TRANSITION–METAL MEDIATED SMALL MOLECULE ACTIVATION AND SYNTHESIS OF ORGANOMETALLIC HOLMIUM BISMUTH COMPLEXES

By

Wilson Wang

A THESIS

Submitted to
Michigan State University
in partial fulfillment of the requirements
for the degree of

Chemistry – Master of Science

2024

ABSTRACT

Nitrous oxide (N_2O) is a potent greenhouse gas with over 310 times the warming power of CO_2 and accounts for 6% of global greenhouse gas emissions. The warming power and extended half-life of N_2O makes it a threat to the atmosphere and environment. To tackle the threat N_2O poses to the atmosphere, the chemistry of N_2O is being explored for applications as a substrate in oxygen atom transfer reactions due to its high thermodynamic oxidizing power (ΔG_f – 104.2 kJ/mol).

Herein, we report the first crystallographic characterization of the pincer iridium hydride (PNP)IrH_2 catalyst, PNP = [N(2-P^iPr_2-4-Me-$C_6H_3)_2$] and the (PNP)Ir(H)Cl complex. Notably, (PNP)IrH_2 can perform selective α C–H activation of linear and cyclic ethers as demonstrated with the reported isolation of the (PNP)Ir=C(C_3H_6O) carbene complex.

The chemistry of dinitrogen is well-studied due to the significance of the nitrogen cycle and its relevance in the industrial Haber-Bosch process. By contrast, the chemistry of the heavier pnictogens is underexplored with the *d*- and *f*-block elements. Unlike lighter pnictogens, bismuth is intriguing due to significant relativistic effects that lead to interesting physical properties, like enhanced spin-orbit coupling and increased magnetic anisotropy.

Herein, we report the isolation of the molecular bismuth-bridged holmium lanthanide complex, ($Cp^*_2Ho)_2$(μ-η^2:η^2-Bi_2), where two holmium(III) centers are linked through a Bi_2^{2-} unit. This marks the first report of a holmium–bismuth bond in a molecular compound.

TABLE OF CONTENTS

LIST OF ABBREVIATIONS

PNP	$H[N(4\text{-}Me\text{-}2\text{-}(P^iPr_2)C_6H_3)_2]$
THF	Tetrahydrofuran
Cp	Cycloopentadienyl
Cp^*	Pentamethylcyclopentadienyl
DCM	Dichoromethane
NBS	*n*-bromosuccinimide
Et_2O	Diethyl ether
*n*BuLi	*n*-butyl lithium
$NaBEt_3H$	Sodium triethyl borohydride
KC_8	Potassium graphite
crypt-222	2.2.2 cryptand
TEMPO	(2,2,6,6-tetramethylpiperidin-1-yl)oxyl)
RE	Rare earth
TM	Transition metal
N_2O	Nitrous oxide
NMR	Nuclear magnetic resonance
SCXRD	Single-crystal X-ray diffraction
IR	Infrared

CHAPTER 1: TRANSITION–METAL MEDIATED SMALL MOLECULE ACTIVATION

1.1 Introduction to Small Molecule Activation

Exploration of the activation and reactivity of small molecules, such as N_2, NH_3, H_2, CO_2, etc. has been prominent over the past few decades due to their abundance and affordability. Small molecule activation is crucial as they are the building blocks used in the construction of larger organic molecules industrially and biologically.[1,2] The Haber-Bosch process is a prevalent example of small-molecule activation that led to the widespread development of industrial fertilizer production in the early 20th century, which is a process that produces ammonia fertilizer by fixating N_2.[3] Fixation is a critical process of the nitrogen cycle that converts dinitrogen to a bioavailable nitrogen source in the form of NH_3, Figure 1.1. This process is so important that it accounts for half of all nitrogen fixed globally, 2% of the global energy consumption, and 4% of global natural gas consumption.[3] Beyond the Haber-Bosch process, small molecule activation is a captivating topic for scientists to explore and develop new renewable energies, modern fuel cells, or new pathways for sustainable organic synthesis.

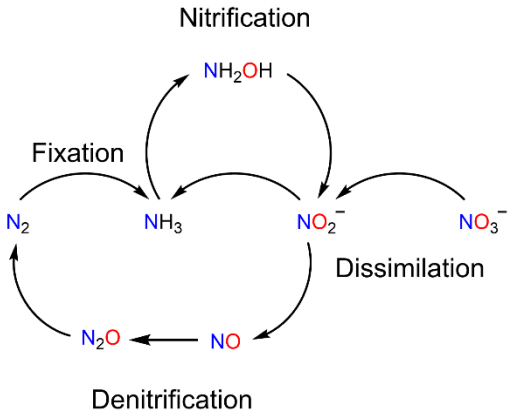

Figure 1.1. Summary of nitrogen cycle

Interest in small molecule activation comes from a diverse range of perspectives, whether it is for investigating clean energy sources, utilizing greenhouse gases as synthons in forging C–N or C–O bonds, among other avenues of research. The difficulties of small molecule activation arises from their thermodynamic and kinetic stability owing to their substantial bond dissociation energies, Table 1.1.[4,5] The nitrogen–oxygen bond in N_2O has a significantly decreased BDE compared to other small molecules because of its resonance structures, Figure 1.2, which leads to elongation of the N=O bond and a lower bond dissociation energy for that bond.

Table 1.1. Bond Dissociation Energies of Common Small Molecules.

Bond Dissociation Energies for Small Molecules	
Compound	**BDE (kcal/mol)**
NN–O	40.0
CH_4	102.7
H_2	104.2
ON–N	114.9
CO_2	127.2
N_2	226.0
CO	257.3

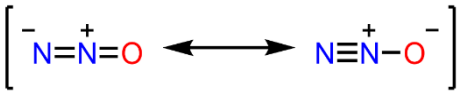

Figure 1.2. Major resonance structures of N_2O.

Functionalization of small molecules often necessitate a transition metal catalyst due to their ability to access different oxidation states and act as an electron source.[1,2] For example, $NiBr_2$(diglyme) can react with aryl halides to cause the metal to undergo oxidative addition followed by a single electron reduction to yield the corresponding phenol, while turning over the nickel catalyst, Figure 1.3A.[6] Although transition metals are most commonly employed as catalysts in small molecule activation, main group elements and lanthanides have been demonstrated to activate small molecules at a much lower cost. An example of a main group element acting as a catalyst is depicted in Figure 3B, where a low-valent gallium (I) complex, GaAr (Ar = 1,6-(2,6-^{i}Pr$_2$C$_6$H$_3$)$_2$-4-(Me$_3$Si)C$_6$H$_2$) activates dihydrogen through cleavage of the H–H bond (104.2 kcal/mol).[7] Figure 1.3C illustrates a sigma-bond metathesis reaction catalyzed by a lanthanide complex where isotopically labeled $^{13}CH_4$ exchanges with the methyl group of a decamethyllutenocene methyl complex.[8]

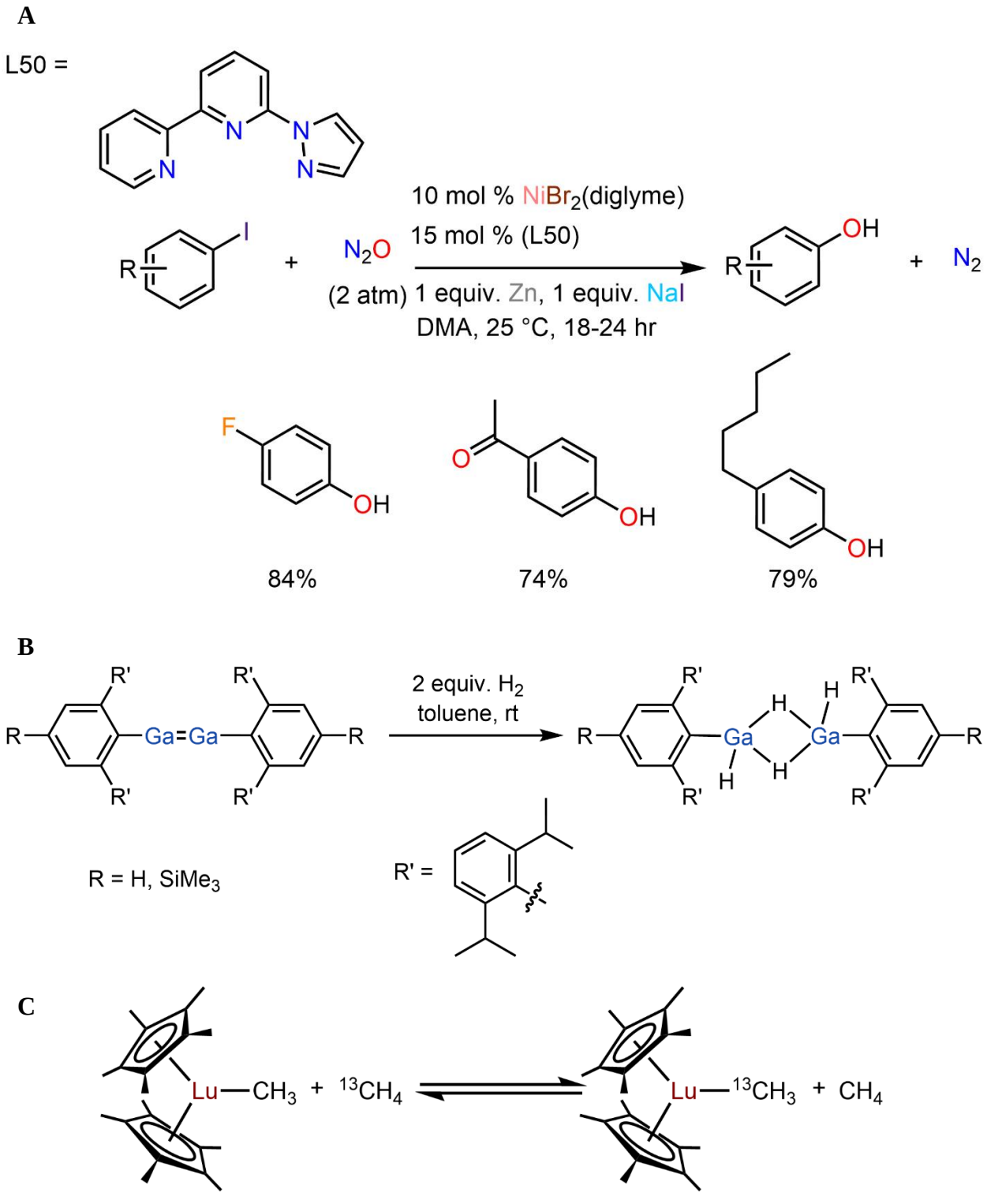

Figure 1.3. Examples of small molecule activation. (A) Catalytic N_2O activation using a nickel catalyst. (B) Activation of H_2 using gallium. (C) Methane activation via a lutetium metallocene complex

1.2 Significance of N_2O

Nitrous oxide (N_2O) is a major greenhouse gas with over 310 times the warming power of CO_2 and an estimated half–life of 120 years.[9] N_2O is also regarded as the most significant contributor to ozone depletion today, despite only accounting for 6% of global greenhouse gas emissions.[9,10,11] The warming power, ozone depleting potential, and long half–life of N_2O makes nitrous oxide a significant threat to the atmosphere and the environment. It poses enough threat that N_2O is one of seven regulated chemical under the Kyoto Protocol that addresses global warming.[10,12] Structurally, N_2O exists in two resonance structures where one nitrogen is positively charged with either the oxygen or the other nitrogen atom being negatively charged depending on the resonance form, Figure 1.2. These resonance forms result in the shortening of the N=N bond distance (1.13 Å) relative to a normal N_2 double bond (1.25 Å). Efforts to tackle N_2O emissions has focused on identifying chemical uses of N_2O and taking advantage of its favorable properties, which include high solubility in polar/nonpolar solvents, stability at most temperatures, high oxidizing power, and minimal toxicity.[9,13]

The main challenges of N_2O activation arise from its kinetic inertness and poor ligand properties making it challenging for insertion of the entire N_2O structural motif into a complex.[13] N_2O has two main coordination modes, Figure 1.4: end–on coordination of the nitrogen or side–on to both nitrogen atoms.[13] Commonly, N_2O is used as an oxygen transfer reagent to deliver oxygen to metal centers and organic substrates liberating dinitrogen in the process. This process occurs due to the much lower BDE of the N–O bond (40 kcal/mol) and the strong thermodynamic driving force of releasing dinitrogen.

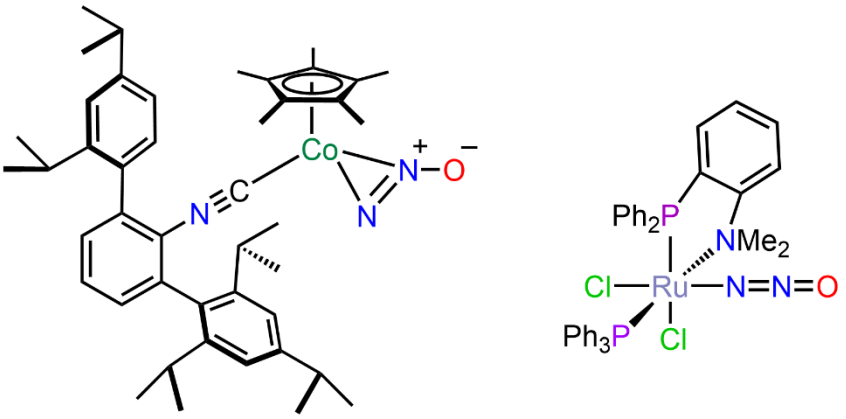

Figure 1.4. End-on (left) or side-on (right) coordination of N_2O

1.3 Transition–Metal Mediated Oxygen Atom Transfer via N_2O

N_2O oxygen atom transfer proves a challenge in ensuring that the target substrate is preferentially oxygenated over the metal center while maintaining regioselectivity. For N_2O catalytic oxygenations, there are two critical factors to consider when activating nitrous oxide while avoiding oxidation of the metal center. First, the selection of the appropriate metal center is crucial as some transition metals have higher affinity for oxygen, while other TMs have higher affinity for dinitrogen. Through literature, reactions of N_2O with early transition metals are commonly shown to result in oxidation of the metal to yield the metal-oxo species.[14-17] This is a result of destabilization of the antibonding p_π-d_π molecular orbitals from strong π-donation of the oxygen lone pairs that are in proximity to the metal, causing it to be more energetically unfavorable to occupy those antibonding orbitals.[15] For example, the addition of N_2O to a niobaziridine–hydride complex leads to generation of the niobium-oxo complex, which is undesirable for further reactivity due to the known stability of metal oxo complexes, Figure 1.5A.[14,18] Therefore, a late transition metal is necessary to avoid oxidation of the metal center, such as the example shown in Figure 1.5B where the oxygen atom is inserted into the Ni–C bond while avoiding formation of the metal oxo derivative.[18] Second, a robust ligand framework is needed that is stable upon complexation, is easily synthesized, occupies large number of coordination sites, and is viable for catalytic transformations.

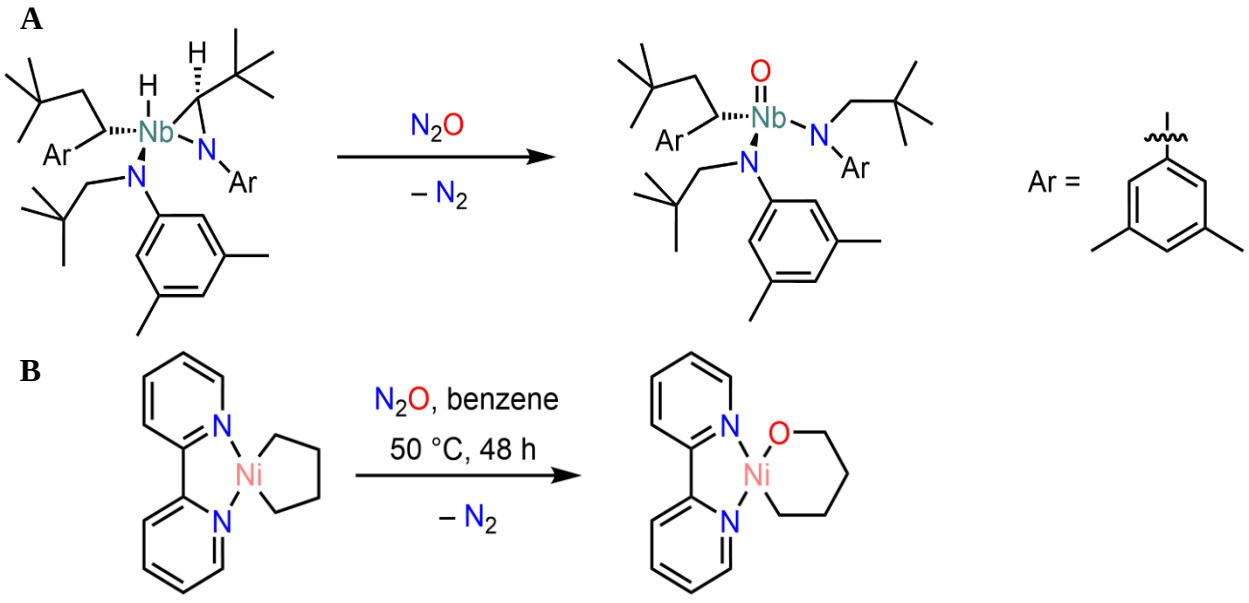

Figure 1.5. **A**. Reaction of niobaziridine–hydride complex with N_2O leading to formation of the Nb oxo compound. **B**. Insertion of oxygen from N_2O into the Ni–C bond of a Ni metallocycle

Considering the two aforementioned factors, the investigation of an ^{Me}PNPIrH$_2$ complex (**1**), ^{Me}PNP = [N(2-P^{i}Pr$_2$-4-Me-C$_6$H$_3$)$_2$]$^-$, for metal-mediated oxygen transfer reactions from N_2O. (^{Me}PNP)IrH$_2$ was selected as it is susceptible to reductive elimination of the dihydride moiety by a hydrogen acceptor. The generated Ir^I species is highly reactive, which can readily undergo oxidative addition to its more stable Ir^{III} oxidation state. Prominent examples of the effectiveness of Ir^I complexes at catalysis are Vaska's complex, (IrCl(CO)(PPh$_3$)$_2$), which readily undergoes reductive elimination or oxidative addition with small molecules, and Crabtree's catalyst, [Ir(cod)(py)(PCy$_3$)][PF$_6$], which is an exceptional hydrogenation catalyst.[19,20] To support the iridium center, a pincer ligand scaffold is used, which is generally defined as any chelating agent that binds tightly to three coplanar meridional positions in a tridentate configuration.[21] Pincer ligand scaffolds enhance the rigidity and thermal stability of the complex and thus, are commonly employed in catalysis. Furthermore, they offer significant such as tunability of the electronics, sterics, and chirality of the catalyst.[21]

It is envisioned that the double C–H activation of the linear ether induced by the reduction of **2** in an excess of norbornene, which acts as the sacrificial hydrogen acceptor, to afford the carbene complex (**II**), Scheme 1.1. Unlike other Fischer carbenes, **I** is nucleophilic at iridium rather than electrophilic at carbon due to the high lying d_z^2 orbital on iridium. Exposure of this carbene with the electrophilic nitrous oxide yields the iridium dinitrogen complex (**II**) while affording the oxygenated organic substrate. The labile N_2 of **II** can be readily displaced from the Ir center by exposure to another molar equivalent of organic substrate allowing for further turnover.[22] The two types of reactions that will be investigated to interrogate the reactivity of **2** with various organic substrates and N_2O are illustrated in Scheme 1.1.

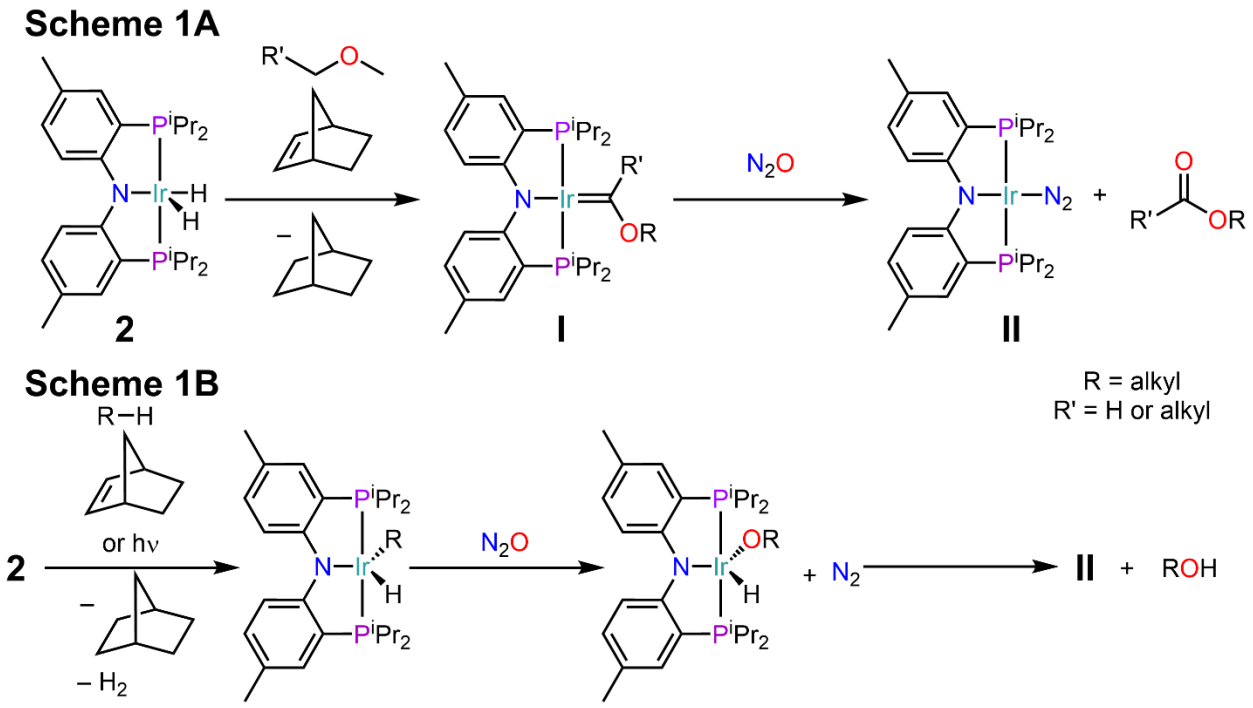

Scheme 1.1. Proposed synthetic pathway of alkyl esters, alkyl formates, and alcohols through oxygenation of Ir-carbene using N_2O.

It has been previously demonstrated that reaction of **2** with linear ethers, such as *sec*-butyl methyl ether, *n*-butyl methyl ether, etc., in the presence of norbornene affords the corresponding carbene, **I**, and following exposure to N_2O affords the organic formate and **II**.[15,16] Hence, this work will investigate the synthesis of the (PNP)IrH_2 catalyst and explore its C–H activation of other alkyl ethers (Scheme 1.1A) and alkanes (Scheme 1.1B). This would then be followed by investigations into viable catalytic opportunities for either reaction scheme.

Alongside linear ethers, C–H activation of cyclic ethers will be investigated to liberate cyclic esters and **3**, as shown in Scheme 1.2 with THF as the cyclic ether. Similar to Scheme 1.1, norbornene is used as a sacrificial hydrogen acceptor to reduce **2** to an Ir(I) intermediate. The Ir(I) species then reacts with the THF solvent to form (^{Me}PNP)Ir=CC_3H_6O (**3**), which is known.[22] However, the following step of reacting the THF carbene complex with N_2O to release γ-butyrolactone and **II** is unknown and will be investigated to see if there is possibility for catalytic turnover.[23,24] This would be an invaluable catalytic process as the cyclic ester moieties are used in medicine, pharmaceuticals, solar cells, among other applications making them highly useful and desirable compounds.[25]

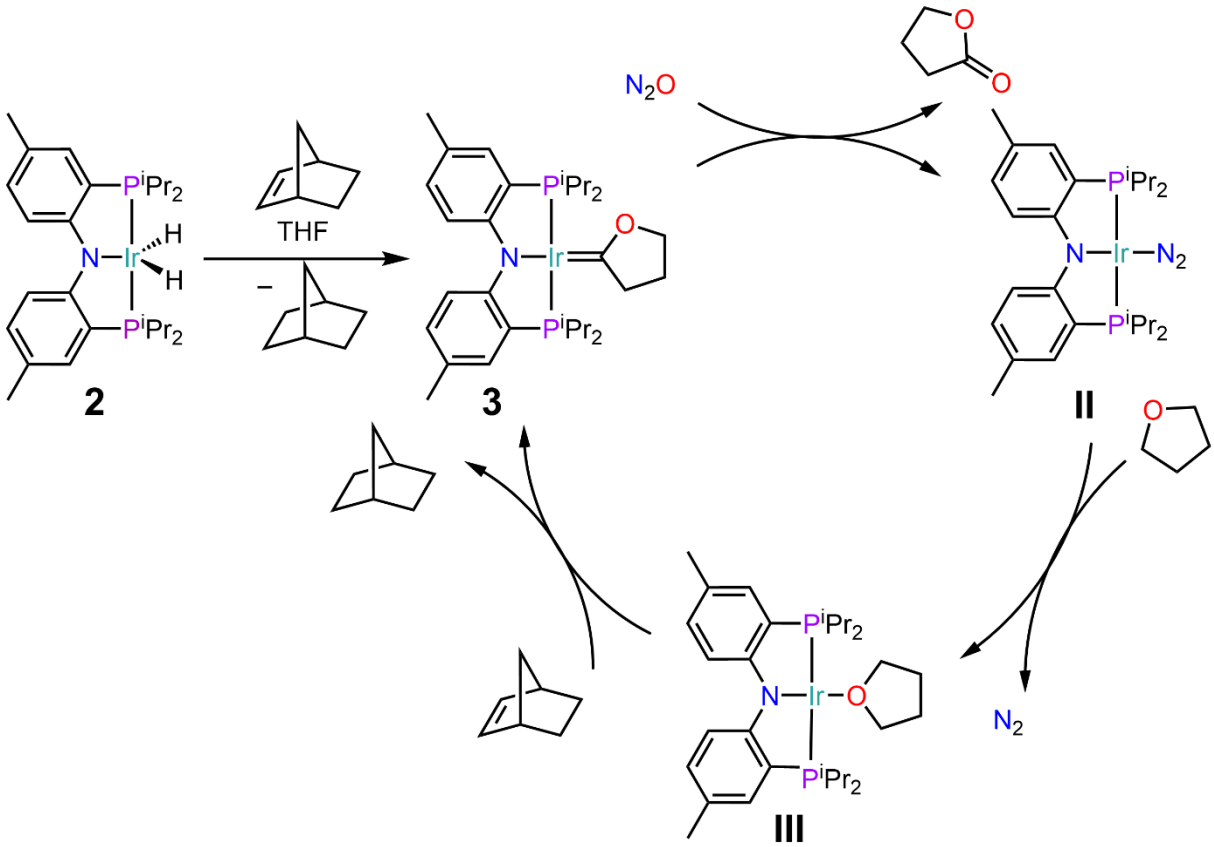

Scheme 1.2. Proposed catalytic cycle for double α-C-H activation of THF and its following oxidation using N_2O.

1.4 Experimental

General Information. All manipulations below were conducted under inert N_2 atmosphere to exclude moisture or oxygen using Schlenk line and glovebox techniques. House nitrogen was purified with a MBraun HP–500–MO–OX gas purifier before use. *n*-hexane, *n*-pentane, dichloromethane, and fluorobenzene were dried by refluxing over calcium hydride and distilled before use. Ethanol, methanol, and DI water were degassed via freeze-pump-thaw cycles prior to use. Tetrahydrofuran, toluene, and diethyl ether were dried by refluxing over potassium and distilled before use. All solvents were tested for the presence of water and oxygen with a drop of sodium benzophenone radical solution in the glovebox. Norbornene was purified via sublimation at 22 °C under 0.03 mbar and was cooled with liquid nitrogen. Benzene–d_6 was purchased from Sigma–Aldrich and dried over 4 Å molecular sieves under inert nitrogen atmosphere. Di-*p*-tolylamine, **A**, 1,5-cyclooctadiene, *n*-bromosuccinimide, diisopropylchlorophosphine, *n*-butyl lithium (2.5 M in hexanes), 1.0 M solution of sodium triethylborohydride ($NaBEt_3H$) in toluene, hexamethyl disiloxane, and $IrCl_3$ x nH_2O were purchased from Aldrich and used as received.

All IR spectra were recorded with a Cary 630 diamond ATR–IR spectrometer in inert nitrogen atmosphere. A PerkinElmer 2400 Series II CHNS/O analyzer was used for CHN elemental analyses. All NMR spectra were taken on Varian or Bruker instruments located in the Max T. Rogers Instrumentation facility at Michigan State University. ^{1}H and ^{13}C NMR spectra were recorded on a Bruker Avance Neo 600 MHz spectrometer with the residual solvent peak being used as the internal reference. ^{31}P NMR were recorded without a reference. Chemical shifts are reported in δ (ppm). A PerkinElmer 2400 Series II CHNS/O analyzer was used for CHN elemental analyses.

X–ray Crystallography Data was collected at a XtaLAB Synergy, Dualflex, HyPix diffractometer equipped with an Oxford Cryosystems low-temperature device, operating at T = 100 K using MoKα radiation. Data for the (PNP)IrH_2 complex was collected at the diffractometer with the Oxford Cryosystems operating at T = 220K. Data were measured using omega and phi scans of 1.0° per frame for 30 s. Cell parameters were retrieved using CrysAlisPro (Rigaku, V1.171.41.90a, 2020) software and refined using CrysAlisPro (Rigaku, V1.171.41.90a, 2020). Data reduction was performed using the CrysAlisPro (Rigaku, V1.171.41.90a, 2020) software.

Synthesis of Bis(2-bromo-4-methylphenyl) amine, ***B***. Compound **B** was synthesized according to the literature procedure.[26] Under dry nitrogen, di-*p*-tolylamine (3.61 g, 20 mmol) was dissolved in

20 mL of dichloromethane (DCM) in a 200 mL Schlenk flask while stirring. Once completely dissolved, *n*-bromosuccinimide (6.52 g, 40 mmol) was slowly added to the reaction mixture causing an immediate color change from pale yellow to dark black. The reaction mixture was stirred for 48 h at ambient temperature to yield a brown-black solution which was dried *in vacuo* to afford a black residue. The black residue was dissolved in pentane and filtered over silica. The clear filtrate was then dried *in vacuo*. White crystals of **B** were obtained from a concentrated hexane solution at –35 °C in 40% crystalline yield (2.58 g, 7.0 mmol). ^{1}H NMR (500 MHz, ppm, $CDCl_3$, 25 °C) δ: 7.40 (d, 2H, *H*–Ph, $^{4}J_{H\text{-}H}$: 2.0 Hz), 7.11 (d, 2H, *H*–Ph, $^{3}J_{H\text{-}H}$: 8.2 Hz), 7.00 (dd, 2H, *H*–Ph, $^{3}J_{H\text{-}H}$ = 8.2 Hz, $^{4}J_{H\text{-}H}$: 1.9 Hz), 6.18 (s, 1H, *H*–N), 2.28 (s, 6H, Ph–*Me*). ^{13}C NMR (126 MHz, ppm, $CDCl_3$, 25 °C) δ: 137.83, (*C*–N) 133.30, (*Ph*), 132.09 (*Ph*), 128.60, (*Ph*), 117.95 (*Ph*), 113.99 (*Ph*), 20.23 (Ph–*Me*)

Synthesis of the PNP(H) ligand (PNP = [HN(4-Me-2-($PiPr_2$)C_6H_3)$_2$]), ***C***. Compound **C** was synthesized according to the literature procedure.[27] Under dry nitrogen, bis(2-bromo-4-methylphenyl) amine (2.01 g, 10 mmol) was dissolved in 30 mL of diethyl ether (Et_2O) in a 200 mL Schlenk flask while stirring and then cooled in a Coldwell with dry ice. Once cooled, *n*-butyl lithium (6.78 mL of a 2.5 M hexane solution) was added dropwise to the stirring reaction mixture. Following the addition, the reaction was removed from the Coldwell and stirred at ambient temperature for 3 h. The reaction mixture was then transferred into the Coldwell, which was cooled with dry ice. Diisopropylchlorophosphine (1.79 mL, 10 mmol) was dispensed dropwise into the stirring reaction mixture causing the solution to turn from pale yellow to bright orange, and this reaction mixture was removed from the Coldwell and stirred at ambient temperature for 24 h. After 24 h of stirring, degassed water (0.31 mL, 20 mmol) was added to the reaction flask and stirred for 45 minutes causing the solution to turn from brown-yellow to an orange-yellow color. This was followed by filtration over silica. The filtrate was dried *in vacuo* and washed with 3 x 20 mL iso-octane. White crystals of **C** were obtained from a concentrated hexamethyldisiloxane solution at –35 °C in 47% crystalline yield (1.14 g, 2.7 mmol) ^{1}H NMR (500 MHz, ppm, benzene-d_6, 25 °C)δ: 8.31 (t, 1H, *H*–N, $^{4}J_{P\text{-}H}$: 8.5 Hz), 7.40 (dd, 2H, *H*–Ph, $^{3}J_{H\text{-}H}$: 8.4 Hz, $^{4}J_{H\text{-}H}$: 4.1 Hz), 7.20 (d, 14 H, *H*–Ph, $^{3}J_{H\text{-}H}$: 2.6 Hz), 6.92 (dd, 2 H, *H*–Ph, $^{3}J_{H\text{-}H}$: 8.4 Hz, $^{4}J_{H\text{-}H}$: 2.1 Hz), 2.19 (s, 6H, Ph–*Me*), 2.02 (m, 4H, *CH*Me_2), 1.13 (dd, 12 H, CH*Me*$_2$, $^{3}J_{H\text{-}H}$: 15.1 Hz, $^{4}J_{H\text{-}H}$: 7.0 Hz), 0.98 (dd, 12 H, CH*Me*$_2$, $^{3}J_{H\text{-}H}$: 11.7 Hz, $^{4}J_{H\text{-}H}$: 6.9 Hz). ^{13}C NMR (126 MHz, ppm, benzene-d_6, 25 °C) δ:147.37 (d, *C*–N, $^{2}J_{C\text{-}P}$: 20.4 Hz), 134.00 (*Ph*), 130.63 (*Ph*), 128.93 (*Ph*), 123.43(d, *Ph*, $^{1}J_{C\text{-}P}$: 16.7), 117.26

(*Ph*), 23.52 (d, *C*HMe$_2$, $^2J_{C\text{-}P}$: 11.4), 20.91 (Ph–*Me*), 20.47 (d, CH*Me*$_2$, $^1J_{C\text{-}P}$: 19.3), 19.27 (d, CH*Me*$_2$, $^2J_{C\text{-}P}$: 9.6). $^{31}P\{^1H\}$ NMR (203 MHz, ppm, benzene-d$_6$, 25 °C) δ: –13.44.

Synthesis of [Ir(COD)Cl]$_2$. [Ir(COD)Cl]$_2$ was synthesized according to the literature procedure.[28] Under dry nitrogen, IrCl$_3$•nH$_2$O (848 mg, 0.003 mol) was added to a 50 mL round bottom flask followed by 11 mL of ethanol and 7 mL of DI water. 3.4 mL of 1,5–cyclooctadiene was transferred to the reaction mixture, which was subsequently heated to 85 °C for 20 h overnight causing the reaction solution to go from dark blue to a light orange color. The solution volume was reduced to 20% volume, and then, the solution was washed with 4 x 5 mL of methanol. Volatiles were removed *in vacuo* and red crystals of [Ir(COD)Cl$_2$] suitable for X–ray diffraction analysis were obtained at –35 °C from a concentrated toluene solution in 61% crystalline yield (0.39 g, 0.58 mmol). ^{1}H NMR (500 MHz, ppm, CDCl$_3$, 25 °C) δ: 4.24 (d, 8H, *CH*, $^3J_{H\text{-}H}$: 4.2 Hz), 2.26 (m, 8H, *CH*$_2$), 1.53 (d, 8H, *CH*$_2$, $^3J_{H\text{-}H}$: 8.1 Hz). ^{13}C NMR (126 MHz, ppm, CDCl$_3$, 25 °C) δ: 62.62 (*C*H), 32.19 (*C*H$_2$).

Synthesis of (PNP)Ir(H)Cl, ***1***. Compound **1** was synthesized according to the literature procedure.[29] Under dry nitrogen, [Ir(COD)Cl]$_2$ (0.21 g, 0.31 mmol) was added to a 20 mL scintillation vial with PNP(H) ligand (0.27 g, 0.62 mmol) and dissolved in 6 mL of fluorobenzene to yield a light orange solution. This solution was stirred overnight for 24 h where a color change to a dark green was observed, and then, the volatiles were removed *in vacuo*. Dark green crystals of **1** suitable for X–ray diffraction analysis was obtained at –35 °C from a concentrated toluene solution in 89% crystalline yield (0.31 g, 0.47 mmol). ^{1}H (500 MHz, ppm, benzene-d$_6$, 25 °C): δ: 7.86 (d, 2H, *H*–Ph, $^3J_{H\text{-}H}$: 8.8 Hz), 6.96 (s, 2H, *H*–Ph), 6.73 (m, 2H, *H*–Ph), 2.94 (m, 2H, *CH*Me$_2$), 2.44 (m, 2H, *CH*Me$_2$), 2.20 (s, 6H, Ph–*Me*), 1.40 (q, 6H, CH*Me*$_2$, $^3J_{H\text{-}H}$: 7.6 Hz), 1.21 (q, 6H, CH*Me*$_2$, $^3J_{H\text{-}H}$: 7.9 Hz), 1.07 (q, 6H, CH*Me*$_2$, $^3J_{H\text{-}H}$: 6.9 Hz), 0.97 (q, 6H, CH*Me*$_2$, $^3J_{H\text{-}H}$: 7.8 Hz), -45.61 (t, 1H, Ir–*H*, $J_{Ir\text{-}H}$: 12.3 Hz). ^{13}C NMR (126 MHz, ppm, benzene-d$_6$, 25 °C) δ: 163.74 (t, *C*–N, $^2J_{C\text{-}P}$: 9.52 Hz), 132.45 (*Ph*), 131.52 (*Ph*), 126.36 (t, *Ph*, $^2J_{C\text{-}P}$: 3.4 Hz), 121.53 (t, *Ph*, $^1J_{C\text{-}P}$: 22.20 Hz), 116.98 (t, *Ph*, $^2J_{C\text{-}P}$: 5.08 Hz), 27.14 (t, *C*HMe$_2$, $^1J_{C\text{-}P}$: 13.22 Hz), 24.59 (t, *C*HMe$_2$, $^1J_{C\text{-}P}$: 16.09 Hz), 20.33 (Ph–*Me)*, 18.64 (CH*Me*$_2$), 18.18 (CH*Me*$_2$). $^{31}P\{^1H\}$ NMR (203 MHz, ppm, benzene-d$_6$, 25 °C) δ: 44.23.

Synthesis of (PNP)IrH$_2$, ***2***. Compound **2** was synthesized according to the literature procedure.[30] Under dry nitrogen, (PNP)Ir(H)Cl was dissolved in 5 mL of THF in a 20 mL scintillation vial. To

this solution, $NaBEt_3H$ (0.15 mL of a 1.0 M hexane solution) was added dropwise. The reaction was stirred for 20 minutes to cause a color change from green to a dark red-orange solution. Volatiles were carefully removed *in vacuo*, and the resulting red residue was dissolved in fluorobenzene and filtered through Celite. The resulting red filtrate was dried *in vacuo*. Bright red crystals of **2** suitable for X–ray diffraction analysis was obtained at –35 °C from a concentrated pentane solution in 38% crystalline yield (0.03g, 0.05 mmol). ^{1}H (500 MHz, ppm, benzene-d_6, 25 °C) : 7.85 (dt, 2H, *H*–Ph, $^3J_{H\text{-}H}$: 8.6 Hz, $^4J_{H\text{-}H}$: *2*.2 Hz), 7.00 (q, 2H, *H*–Ph, $^4J_{H\text{-}H}$: 3.6 Hz), 6.90 (dd, 2H, *H*–Ph, $^3J_{H\text{-}H}$: 8.7 Hz, $^4J_{H\text{-}H}$: *2*.1 Hz), 2.22 (s, 6H, Ph–*Me*), 2.13 (m, 4H, *CH*Me_2) 1.22 (q, 12H, CH*Me*$_2$, $^3J_{H\text{-}H}$: 7.6 Hz), 1.00 (q, 12H, CH*Me*$_2$, $^3J_{H\text{-}H}$: 7.1 Hz), -25.41 (t, 2H, Ir–*H*$_2$, $J_{Ir\text{-}H}$: 10.7 Hz). ^{13}C NMR (126 MHz, ppm, benzene-d_6, 25 °C) δ: 164.59 (t, *C*–N, $^2J_{C\text{-}P}$: 10.76 Hz), 133.27 (*Ph*), 131.64 (*Ph*), 126.58 (t, *Ph*, $^2J_{C\text{-}P}$: 10.76 Hz), 126.22 (t, *Ph*, $^1J_{C\text{-}P}$: 19.7 Hz), 115.03 (*Ph*), 25.19 (*C*HMe_2)), 22.54 (*C*HMe_2), 20.22 (Ph–*Me*), 20.01 (CH*Me*$_2$), 18.47 (CH*Me*$_2$). ^{31}P{^{1}H} NMR (203 MHz, ppm, benzene-d_6, 25 °C): δ: 57.76.

Synthesis of (PNP)Ir=C(C_3H_6O), ***3***. Compound **3** was synthesized according to the literature procedure[24]. Under dry nitrogen, Norbornene (0.04 g, 0.45 mmol) was weighed into a 4 mL scintillation vial with (PNP)IrH_2 (0.04 g, 0.06 mmol), and the mixture was dissolved in 0.3 mL of THF. The red solution was transferred to a J. young tube that was heated 60 °C for 20 h overnight causing no significant changes in color. The red solution was filtered through Celite, and the resulting dark red filtrate was dried *in vacuo*. Bright red crystals of **3** suitable for X–ray diffraction analysis was obtained at –35 °C from slow evaporation of a concentrated pentane solution in 50% crystalline yield (0.02 g, 0.03 mmol). ^{1}H NMR (500 MHz, ppm, benzene-d_6, 25 °C) : 7.90 (d, 2H, *H*–Ph, $^3J_{H\text{-}H}$: 8.6 Hz), 7.26 (d, 2H, *H*–Ph, $^3J_{H\text{-}H}$: 3.1 Hz), 6.87 (dd, 2H, *H*–Ph, $^3J_{H\text{-}H}$: 8.6 Hz, $^4J_{H\text{-}H}$: 2.1 Hz), 3.51 (t, 2H, C_3H_6O, $^3J_{H\text{-}H}$: 7.0 Hz), 2.68 (ddd, 4H, *CH*Me_2, $^3J_{H\text{-}H}$: 7.1 Hz, $^4J_{H\text{-}H}$: 4.4 Hz, $^4J_{H\text{-}H}$: 2.7 Hz), 2.30 (s, 6H, Ph–*Me*), 1.38 (qu, 2H, C_3H_6O, $^3J_{H\text{-}H}$: 7.3 Hz), 1.32 (q, 13H, CH*Me*$_2$, $^3J_{H\text{-}H}$: 7.4 Hz), 1.26 (q, 13 H, CH*Me*$_2$, $^3J_{H\text{-}H}$: 6.9 Hz), 0.39 (t, 2H, C_3H_6O, $^3J_{H\text{-}H}$: 7.6 Hz).

1.5 Results and Discussion

The synthesis of the PNP(H) pincer ligand, (PNP = [N(4-Me-2-(P^iPr_2)C_6H_3)$_2$]), and the (PNP)IrH_2 complex followed procedures published by Ozerov *et al*, as depicted in Scheme 1.3.

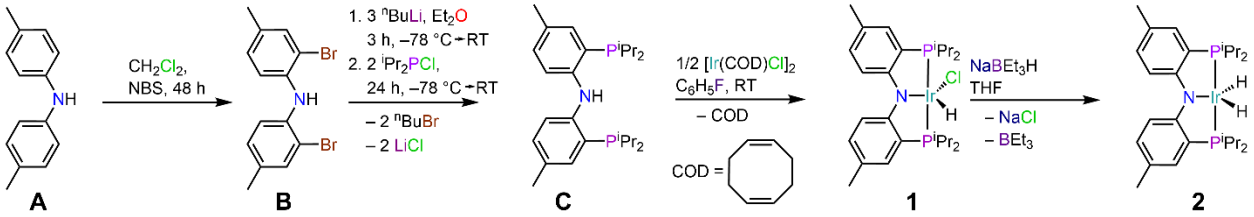

Scheme 1.3. Synthetic Scheme for the (PNP)IrH_2 complex

Bromination of di-*p*-tolylamine (**A**) with *n*-bromosuccinimide is expected to brominate at both ortho positions to the nitrogen because the amine group acts as a stronger ortho director than the methyl group. This is confirmed via ^{1}H NMR by a singlet peak at 7.40 ppm, suggesting an aromatic proton in a highly de-shielded environment that is induced by a neighboring heteroatom, such as bromine. In the ^{1}H NMR of **A**, each chemical shift is shifted 0.02 ppm higher compared to what is reported in literature, and this likely resulted from differences in how the solvent or instrument was referenced. The doublet at 7.4 ppm corresponding to an aromatic proton is reported as a singlet in literature, and this could be a result of 4-bond coupling to the meta proton giving rise to a 2.0 Hz coupling. This is corroborated by an aromatic signal at 7 ppm that also has 1.9 Hz coupling likely back to the proton with the 7.4 chemical shift. 2 Hz couplings are also commonly designated as meta couplings with a methyl substituent between them in aromatic molecules. A higher sample concentration or higher field strength instrument could be responsible for why this peak was observed as a doublet rather than a singlet, as reported in literature.

Following bromination, a phosphine–halide exchange reaction was completed to exchange the bromine with phosphine groups precipitating LiCl. The structure was confirmed via ^{1}H NMR spectrum where the singlet N–H peak becomes significantly de-shielded to 8.5 ppm, resulting from the de-shielding induced by the phosphines at the ortho positions. The doublet at 7.2 ppm corresponding to an aromatic proton is reported as a singlet in literature, and similar to **A**, this could be due to 4-bond coupling to a meta proton. This is further suggested due to the aromatic proton at 6.92 ppm having a 2.0 Hz coupling, which could be meta coupling back to the proton at 7.2 ppm. The peaks at 7.40 and 6.92 ppm are reported to be doublets, but in the obtained spectrum,

they are reported as doublet of doublets, which likely results from the higher resolution enabled by the higher field strength of the instrument used for the experiment (500 MHz) compared to the literature (400 MHz). The ^{31}P NMR spectrum of the ligand indicates presence of phosphorus in the sample with a chemical shift at –13.44 ppm, like what is reported in literature. (–12.9 ppm) [27]

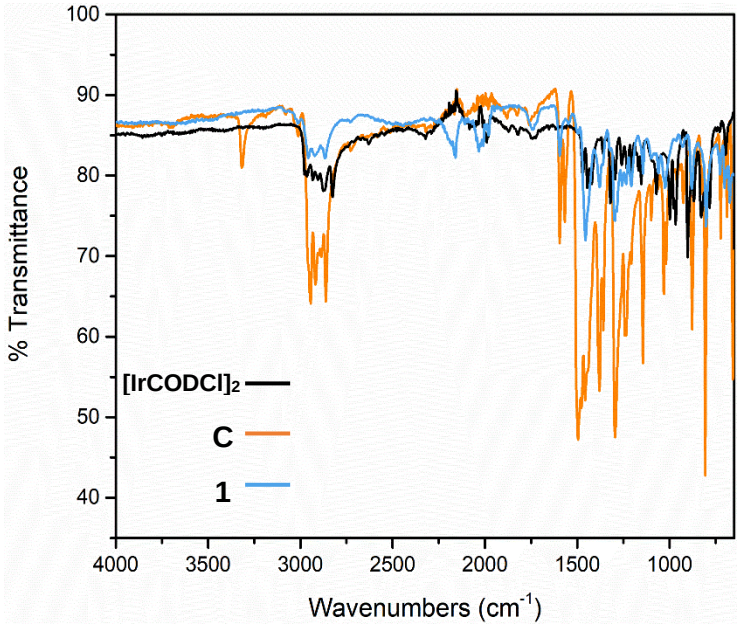

Figure 1.6. IR spectrum of [Ir(COD)Cl_2] (in black), PNP(H) ligand (in orange), and (PNP)Ir(H)Cl (in blue).

[Ir(COD)Cl_2] was synthesized through the reduction of $IrCl_3$•nH_2O with ethanol followed by complexation to 1,5 cyclooctadiene (COD). The (PNP)H is metalated with [Ir(COD)Cl]$_2$ in fluorobenzene to release cyclooctadiene. Dark green crystals of (PNP)Ir(H)Cl, **1**, suitable for single-crystal X-ray diffraction analysis complex were grown from a concentrated toluene solution at –35 °C. The molecular structure of **1** was confirmed via single-crystal X-ray diffraction analysis, Figure 1.7A, and to the best of our knowledge, this is the first report of a crystal structure for **1**, although its synthesis is known. The complex crystallizes in the *P*2/*n* space group with free toluene molecules in the lattice. The Ir–Cl, Ir–P, and Ir–N distances are 2.370(2), 2.295(1), and 2.051(3) Å, respectively, which are well within observed Ir–Cl, Ir–P, and Ir–N distances in other Ir–PNP compounds.[31-34] The P–Ir–P angle is 163.8(1)° which is well within observed P–Ir–P angles reported in other Ir–PNP compounds.[33, 34] The crystal structure shows the flexibility of the pincer ligand backbone since after coordination, the ligand is nonplanar. The chlorine atom is slightly out of plane relative to the iridium center and the ligand backbone, which could suggest the presence of an equatorial hydride that pushes the chlorine atom out of plane. However, hydrides cannot be

confirmed through SCXRD analysis as hydrogen atoms have minimal electron density. Instead, the presence of the hydride was proven via ^{1}H NMR spectroscopy with a triplet occurrence at –46 ppm that integrates to one, and the negative chemical shift is characteristic for a metal hydride. The IR spectrum clearly indicates a reaction of the N–H bond on the pincer ligand because the diagnostic IR stretching mode for the N–H bond is absent in the product, Figure 1.6. The IR spectrum of the product also shows new peaks at around 2000–2200 cm^{-1}, which could signify the Ir–H stretch.

NMR spectroscopy of compound **1** is very similar to what has been reported in literature with some slight differences. In ^{1}H NMR, the peak at 6.73 ppm is a multiplet rather than a singlet, which is what is reported in literature. This could be a result more resolved aromatic coupling of this proton to other aromatic protons due to the higher field strength of the instrument used for the experiment (500 MHz) compared to the literature (400 MHz). In ^{13}C NMR, the peaks at 122.2 and 24.59 ppm have slightly larger coupling (1.2 and 1.09 Hz, respectively) compared to what is reported in literature, and this small difference could arise from differences in how the coupling constants were calculated. Heteronuclear coupling between carbon and phosphorus throughout the experiment could have also led to distortions in the spectrum that can lead to slight changes in the coupling constant.

Sodium triethyl borohydride was reacted with (PNP)Ir(H)Cl, **1**, in a salt metathesis reaction to yield (PNP)IrH_2, **2**, and the byproducts NaCl and triethyl boron. Red-orange crystals of **2** suitable for single-crystal X-ray diffraction analysis were grown from a concentrated pentane solution at –35 °C. The molecular structure of **2** was confirmed via single-crystal X-ray diffraction analysis, Figure 1.7B, and is to the best of our knowledge, the first report of a crystal structure for **2**, although its synthesis is known. The complex crystallizes in the highly symmetric and unusual *I*a$\bar{3}$d space group. The Ir–P and Ir–N distances are 2.2260(2), and 2.047(5) Å, respectively, which are well within observed Ir–P and Ir–N distances in other Ir–PNP compounds.[31-34] The P–Ir–P angle is 167.1(1)° which is well within observed P–Ir–P angles reported in other Ir–PNP compounds.[33, 34] Compared to **1**, Figure 1.7A, the Ir–N and Ir–P distances are slightly shorter in **2**, while the P–Ir–P angle increases slightly by 3.3°.

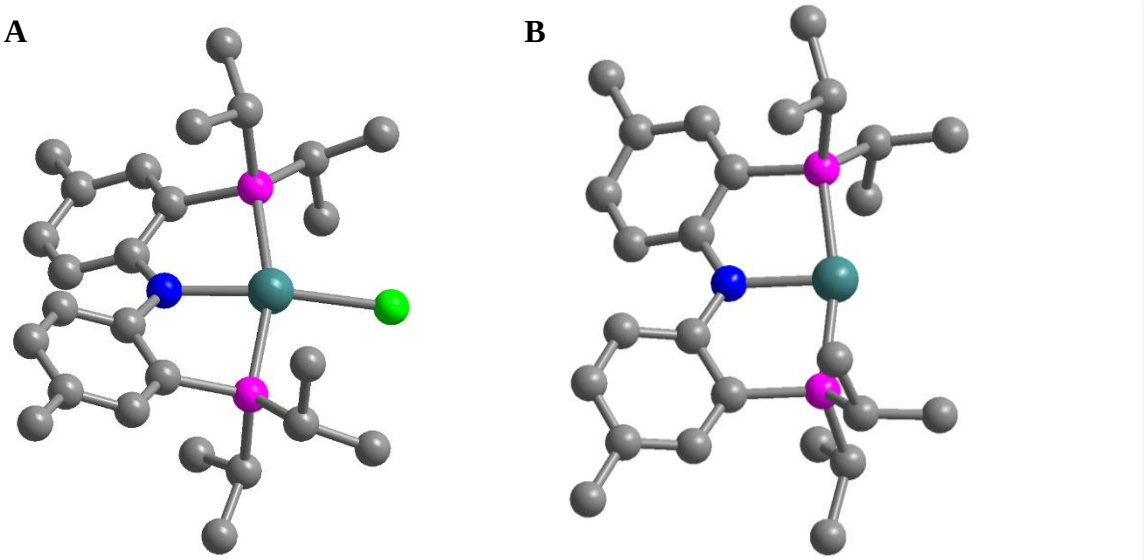

Figure 1.7. Structures of **1** and **2** in crystals of (PNP)Ir(H)Cl (A) and (PNP)IrH_2 (B), respectively. Green, pink, gray, blue, and teal ellipsoids represent chlorine, phosphorus, carbon, nitrogen, and iridium atoms, respectively. H atoms have been omitted for clarity. Selected distances (Å) and angles (deg) for (PNP)Ir(H)Cl and (PNP)IrH_2, respectively: Ir–Cl = 2.370(2); Ir–P = 2.295(1), 2.260(2); Ir–N = 2.051(3), 2.047(5); P–Ir–P = 163.8(1), 167.1(1)

IR data of crystalline **2** resembles the **1** with peaks at similar wavenumbers but with changes in the peak intensity. This further suggests that the stretches at 2000–2200 cm^{-1} may be the Ir–H stretch. The presence of hydrides was confirmed via ^{1}H NMR spectroscopy through the triplet occurrence at –25.41 ppm that integrates to two. The ^{1}H NMR also closely aligns with the reported literature spectrum for **2** with slight differences. The doublet of triplets at 7.85 ppm is reported as a doublet in literature. The peak at 7.00 ppm is a quartet instead of the reported singlet in literature, and the doublet of doublet at 6.9 ppm is reported as a doublet in literature. These multiplicity differences likely arise from the stronger field strength of the instrument used (500 MHz) compared to the field strength of the literature spectrum (400 MHz). This along with differences in sample concentrations could allow for the better resolution of the spectrum to fully elucidate the ortho and meta couplings of these protons and cause changes in multiplicities observed compared to literature. The ^{13}C NMR is similar to what is reported but the peak at 126.78 ppm has a significantly larger coupling of 10.76 Hz compared to the reported 3 Hz coupling for this peak in literature. This large difference is likely a result of distortions caused by heteronuclear carbon – phosphorus coupling that evolves through the experiment which can lead to significant changes in the spectrum or in coupling constants. Despite those differences, the other characterization techniques and the rest of the NMR spectrum support the isolation of **2**.

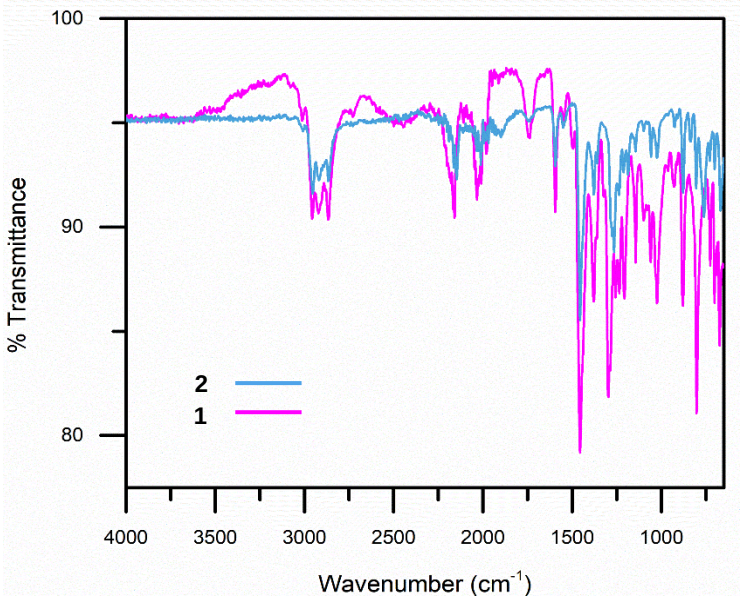

Figure 1.8. IR spectrum of (PNP)Ir(H)Cl (light blue) and (PNP)IrH_2 (pink).

The (PNP)IrH_2, **2**, complex was reacted with norbornene, which acts as a sacrificial hydrogen acceptor, in a solution of THF over 24 h to afford the (PNP)Ir=C(C_3H_6O) carbene complex, **3**. Dark red crystals of **3** suitable for single-crystal X-ray diffraction analysis were grown from a

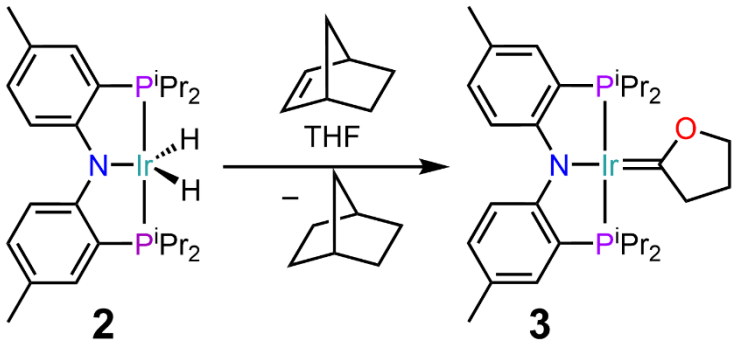

Scheme 1.4. Synthesis of the (PNP)Ir=C(C_3H_6O), **3**, carbene from **2**

concentrated pentane solution at –35 °C. The molecular structure of **3** was proven through single-crystal X-ray diffraction analysis, Figure 1.8. The complex crystallizes in the *Pbcn* space group. The Ir–P, Ir–N, and Ir–C distances are 2.286(1), 2.078(2), and 1.904(3) Å, respectively, which are well within observed Ir–P and Ir–N distances in other Ir–PNP compounds.[31-34,] The P–Ir–P angle is 163.1(1)°, which is well within observed P–Ir–P angles reported in other Ir–PNP compounds.[33, 34] The shortened Ir–C bond distance of 1.904 Å falls in the range expected for iridium carbene complexes.[35] The ^{1}H NMR spectrum of the complex confirms that a hydride abstraction occurred as there are no protons in the negative ppm region, and the THF coordination is supported by the

appearance of three new peaks corresponding to the three methylene groups on THF. The ^{1}H NMR of **3** is similar to what is reported in literature with slight differences in peak multiplicities, similar to **1**. The doublet at 7.26 ppm is reported as a singlet in literature, and the peak at 6.87 ppm is a doublet of doublet instead of the doublet reported in literature. Finally, the doublet of doublet of doublet at 2.68 ppm is reported as a multiplet in literature. These differences likely result from differences in sample concentration or in instrument field strength, but the latter cannot be confirmed as the literature does not specify if the instrument used to measure **3** was 400 or 500 MHz.

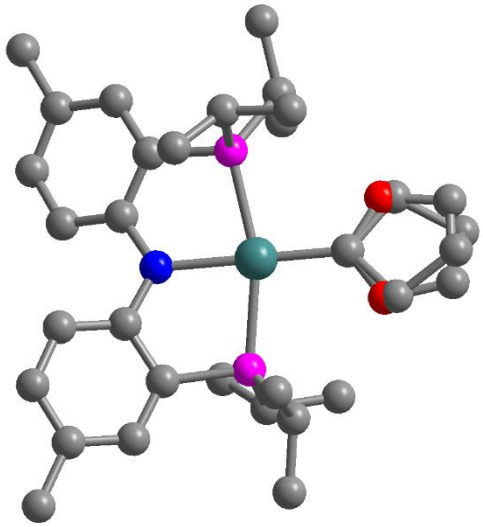

Figure 1.9. Structure of **3** in a crystal of (PNP)Ir=C(C_3H_6O). Red, pink, gray, blue, and teal ellipsoids represent oxygen, phosphorus, carbon, nitrogen, and iridium atoms, respectively. H atoms have been omitted for clarity. Selected distances (Å) and angles (deg) for of (PNP)Ir=C(C_3H_6O): Ir–P = 2.286(1); Ir–N = 2.078(2); Ir–C = 1.904(3); P–Ir–P = 163.1(1).

1.6 Conclusion

Herein, the synthesis of the (PNP)IrH_2 complex was accomplished using a multistep synthetic protocol published in literature. The (PNP)Ir(H)Cl and (PNP)IrH_2 complexes were characterized for the first time through single-crystal X-ray diffraction analysis. The dihydride complex was subjected to double α-C–H activation of tetrahydrofuran to afford the THF-activated (PNP)Ir=C(C_3H_6O) complex. In the future, the goal is the oxidation of the cyclic carbene using N_2O to oxygenate the substrate while coordinating dinitrogen to the iridium complex. Such functionalizations are not yet known and would be a major step in using N_2O as an oxygen atom transfer reaction to oxygenate cyclic ethers. If N_2O can cleanly oxygenate the cyclic carbene, it could lead to possible catalytic opportunities to catalytically generate cyclic esters from cyclic ethers using N_2O with the iridium dihydride complex, and this could be monumental in being able to generate cyclic esters that have a large array of industrial uses. Furthermore, if this is successful, this strategy could also be applied to the oxygenation of alkanes and ethers to generate other value-added products from this greenhouse gas.

REFERENCES

1. Yadav, S.; Saha, S.; Sen, S. S. Compounds with Low-Valent p-Block Elements for Small Molecule Activation and Catalysis. *Chem. Cat. Chem.* **2016**, *8*, 486–501.

2. Milani, B.; Licini, G.; Clot, E.; Albrecht, M. Small Molecule Activation. *Dalton Trans.* **2016**, *45* (37), 14419–14420.

3. Lehnert, N.; Peters, J. C. Preface for Small-Molecule Activation: From Biological Principles to Energy Applications. Part 2: Small Molecules Related to the Global Nitrogen Cycle. *Inorg. Chem.* **2015**, *54*, 9229–9233.

4. Benson, S. W. –II - Bond Energies. *J. Chem. Educ.* **1965**, *42*, 502–518.

5. Darwent, B. deB. Bond Dissociation Energies in Simple Molecules. U.S. National Bureau of Standards, 1970.

6. Le Vaillant, F.; Mateos Calbet, A.; González-Pelayo, S.; Reijerse, E. J.; Ni, S.; Busch, J.; Cornella, J. Catalytic Synthesis of Phenols with Nitrous Oxide. *Nature* **2022**, *604*, 677–683.

7. Zhu, Z.; Wang, X.; Peng, Y.; Lei, H.; Fettinger, J. C.; Rivard, E.; Power, P. P. Addition of Hydrogen or Ammonia to a Low-Valent Group 13 Metal Species at 25 °C and 1 Atmosphere. *Angew. Chem. Int. Ed.* **2009**, *48*, 2031–2034.

8. Watson, P. L.; Parshall, G. W. Organolanthanides in Catalysis. *Acc. Chem. Res.* **1985**, *18*, 51–56.

9. Trogler, W. C. Physical Properties and Mechanisms of Formation of Nitrous Oxide. *Coord. Chem. Rev.* **1999**, *187*, 303–327.

10. US EPA, O. https://www.epa.gov/ghgemissions/global-greenhouse-gas-emissions-data (accessed 2024-03-01).

11. Ravishankara, A. R.; Daniel, J. S.; Portmann, R. W. Nitrous Oxide (N_2O): The Dominant Ozone-Depleting Substance Emitted in th^{e} 21st Century. *Science* **2009**, *326*, 123–125.

12. UNFCCC. https://unfccc.20yotoyoto_protocol (accessed 2024-03-01)

13. Tolman, W. B. Binding and Activation of N_2O at Transition-Metal Centers: Recent Mechanistic Insights. *Angew. Chem. Int. Ed.* **2010**, *49*, 1018–1024.

14. Figueroa, J. S.; Cummins, C. C. The Niobaziridine−Hydride Functional Group: Synthesis and Divergent Reactivity. *J. Am. Chem. Soc.* **2003**, *125*, 4020–4021.

15. Gunay, A.; Theopold, K. H. C−H Bond Activations by Metal Oxo Compounds. *Chem. Rev.* **2010**, *110*, 1060–1081.

16. Bottomley, F.; Lin, I. J. B.; Mukaida, M. Reactions of Dinitrogen Oxide (Nitrous Oxide)

with Dicyclopentadienyltitanium Complexes Including a Reaction in Which Carbon Monoxide Is Oxidized. *J. Am. Chem. Soc.* **1980**, *102*, 5238–5242.

17. Smith, M. R. I.; Matsunaga, P. T.; Andersen, R. A. Preparation of Monomeric $(Me_5C_5)_2VO$ and $(Me_5C_5)_2Ti(O)(L)$ and Their Decomposition to $(Me_5C_5)_4M_4(\mu\text{-}O)_6$. *J. Am. Chem. Soc.* **1993**, *115*, 7049–7050.

18. Matsunaga, P. T.; Hillhouse, G. L.; Rheingold, A. L. Oxygen-Atom Transfer from Nitrous Oxide to a Nickel Metallacycle. Synthesis, Structure, and Reactions of Cyclic (2,2'-Bipyridine)$Ni(OCH_2CH_2CH_2CH_2)$. *J. Am. Chem. Soc.* **1993**, *115*, 2075–2077.

19. Crabtree, R. Iridium Compounds in Catalysis. *Acc. Chem. Res.* **1979**, *12*, 331–337.

20. Kirss, R. U.; Ma, B. FIFTY YEARS OF VASKA'S COMPOUND (1). *Bull. Hist. Chem.* **2013**, *38*, 52-60.

21. Peris, E.; H. Crabtree, R. Key Factors in Pincer Ligand Design. *Chem. Soc. Rev.* **2018**, *47*, 1959–1968.

22. Whited, M. T.; Grubbs, R. H. A Catalytic Cycle for Oxidation of Tert–Butyl Methyl Ether by a Double C–H Activation-Group Transfer Process. *J. Am. Chem. Soc.* **2008**, *130*, 16476–16477.

23. Brookes, N. J.; Whited, M. T.; Ariafard, A.; Stranger, R.; Grubbs, R. H.; Yates, B. F. Factors Dictating Carbene Formation at (PNP)Ir. *Organometallics* **2010**, *29*, 4239–4250.

24. Whited, M. T.; Zhu, Y.; Timpa, S. D.; Chen, C.-H.; Foxman, B. M.; Ozerov, O. V.; Grubbs, R. H. Probing the C−H Activation of Linear and Cyclic Ethers at (PNP)Ir. *Organometallics* **2009**, *28*, 4560–4570.

25. Fateh, S. T.; Salehi-Najafabadi, A. Repurposing of Substances with Lactone Moiety for the Treatment of γ-Hydroxybutyric Acid and γ-Butyrolactone Intoxication through Modulating Paraoxonase and PPARγ. *Front. Pharmacol.* **2022**, *13*, 01–07.

26. Davidson, J. J.; DeMott, J. C.; Douvris, C.; Fafard, C. M.; Bhuvanesh, N.; Chen, C.-H.; Herbert, D. E.; Lee, C.-I.; McCulloch, B. J.; Foxman, B. M.; Ozerov, O. V. Comparison of the Electronic Properties of Diarylamido-Based PNZ Pincer Ligands: Redox Activity at the Ligand and Donor Ability Toward the Metal. *Inorg. Chem.* **2015**, *54*, 2916–2935.

27. Fan, L.; Foxman, B. M.; Ozerov, O. V. N−H Cleavage as a Route to Palladium Complexes of a New PNP Pincer Ligand. *Organometallics* **2004**, *23*, 326–328.

28. Cotton, F. A.; Lahuerta, P.; Sanau, M.; Schwotzer, W. Air Oxidation of $Ir_2(Cl)_2(COD)_2$ Revisited. The Structures of $[Ir(\mu^2\text{-}Cl)(COD)]_2$(Ruby Form) and Its Oxidation Product, $Ir_2Cl_2(COD)_2(\mu^2\text{-}OH)_2(\mu^2\text{-}O)$. *Inorganica Chimica Acta* **1986**, *120*, 153–157.

29. Ozerov, O. V.; Guo, C.; Papkov, V. A.; Foxman, B. M. Facile Oxidative Addition of N−C and N−H Bonds to Monovalent Rhodium and Iridium. *J. Am. Chem. Soc.* **2004**, *126*, 4792–4793.

30. Fan, L.; Parkin, S.; Ozerov, O. V. Halobenzenes and Ir(I): Kinetic C−H Oxidative Addition and Thermodynamic C−Hal Oxidative Addition. *J. Am. Chem. Soc.* **2005**, *127*, 16772–16773.

31. Weng, W.; Guo, C.; Moura, C.; Yang, L.; Foxman, B. M.; Ozerov, O. V. Competitive Activation of N−C and C−H Bonds of the PNP Framework by Monovalent Rhodium and Iridium. *Organometallics* **2005**, *24*, 3487–3499.

32. Ben-Ari, E.; Leitus, G.; Shimon, L. J. W.; Milstein, D. Metal−Ligand Cooperation in C−H and H2 Activation by an Electron-Rich PNP Ir(I) System: Facile Ligand Dearomatization−Aromatization as Key Steps. *J. Am. Chem. Soc.* **2006**, *128*, 15390–15391.

33. Hermann, D.; Gandelman, M.; Rozenberg, H.; Shimon, L. J. W.; Milstein, D. Synthesis, Structure, and Reactivity of New Rhodium and Iridium Complexes, Bearing a Highly Electron-Donating PNP System. Iridium-Mediated Vinylic C−H Bond Activation. *Organometallics* **2002**, *21*, 812–818.

34. S. Lokare, K.; J. Nielsen, R.; Yousufuddin, M.; Iii, W. A. G.; A. Periana, R. Iridium Complexes Bearing a PNP Ligand, Favoring Facile C(Sp 3)–H Bond Cleavage. *Dalton Transactions* **2011**, *40*, 9094–9097.

35. Ramollo, G. K.; Strydom, I.; Fernandes, M. A.; Lemmerer, A.; Ojwach, S. O.; van Wyk, J. L.; Bezuidenhout, D. I. Fischer Carbene Complexes of Iridium(I) for Application in Catalytic Transfer Hydrogenation. *Inorg. Chem.* **2020**, *59*, 4810–4815.

CHAPTER 2: INTRODUCTION OF DIATOMIC BISMUTH UNITS INTO RARE EARTH CHEMISTRY

2.1 Importance and Significance of Bismuth

The chemistry of nitrogen is well studied due to its prevalence in the nitrogen cycle, but the chemistry of the heavier pnictogens is much less explored, especially in the form of metal complexes with the *d*- and *f*- block elements. This is especially noticeable with the *f*- block elements whereas of August 2023, there are almost 30,000 known *f*- block nitrogen complexes which is over 30 times the number of heavier pnictogen *f*- element complexes. This trend remains true with the *d*- block elements although to a lesser extreme with bismuth having the least known number of complexes with the *f*- and *d*- block elements.[1]

Bismuth is slightly radioactive with a half-life of 2.01×10^{19} years, and the heaviest period 6 main group element that is relatively non-toxic unlike its neighbors, thallium, lead, and polonium.[1,2] As bismuth is a heavy element, it experiences significant 6s orbital contraction and radial expansion of the 6p orbitals due to relativistic effects, and this can enable enormous spin–orbit coupling.[2,3] Bismuth is also able to adopt a wide variety of coordination numbers, coordination modes, and formal oxidation states.[2] Commonly, bismuth exists predominantly in its Bi^{III} oxidation state due to the inert-pair effect (relativistic effects) of the $6s^2$ electrons that makes the Bi^{V} oxidation state less stable.[3] However, bismuth has also been shown to exist in lower oxidation states such as Bi^{-I} compounds.[2] Bismuth also exhibits highly variable coordination numbers ranging from 3-coordinate to 9-coordinate complexes.[5]

The unique properties of bismuth have caused researchers to explore its uses in functional and sustainable materials. One such example is the use of bismuth in materials chemistry as a replacement for lead in photovoltaic perovskite materials due to its lower toxicity.[2] Bi^{III} compounds have also seen use in organic synthesis in the oxidation of alcohols, epoxides, sulfides, etc. due to their strong Lewis acidity, low toxicity, and tolerance towards moisture.[6] Furthermore, bismuth has seen extensive use in radical chemistry and photoredox catalysis via accessing the Bi^{II} radical by performing single electron reduction of common Bi^{III} compounds, and these radicals can undergo radical–radical coupling with reagents like TEMPO (2,2,6,6-tetramethylpiperidin-1-yl)oxyl).[7,8] The most well-known application of bismuth compounds is in the medicinal field as stomach remedies in the forms of bismuth subsalicylate (Pepto-Bismol) and colloidal bismuth subcitrate (De-Nol).[9]

2.2 Rare Earth Metal-Mediated Activation

Although bismuth chemistry is underexplored with both transition metals and rare earth metals, the rare earth elements have intrinsic properties that allow for the isolation of molecules that would normally be unattainable in molecular systems with transition metals. The reactivity of the rare earth elements is fundamentally different from the transition metals in that they are commonly trivalent and rarely seen in the +I or +IV oxidation state in metal complexes. The lanthanides also have their coordination geometries almost entirely dictated by steric attributes rather than the ligand field. Another crucial difference between the lanthanides and the transition metals is the presence of the 4f orbitals which are deeply buried and contracted causing them to not participate in bonding. The result is that chemical bonds with the lanthanides and the other rare earth elements are predominantly ionic.[10] The strong ionic interactions of the lanthanides with other elements allow for the isolation of molecular compounds containing unique chemical motifs, such as the first ever isolation of the $N_2^{3\bullet-}$ and the $(NO)^{2\bullet-}$ radical anions in 2009 and 2010, respectively, Figure 2.1[11,12] Prior to these publications, these ions had never been observed in any reported isolated complex. Rare-earth elements facilitated the isolation of these radical complexes due their ionic nature that can trap the radical and prevent it from communicating with the external environment.[13]

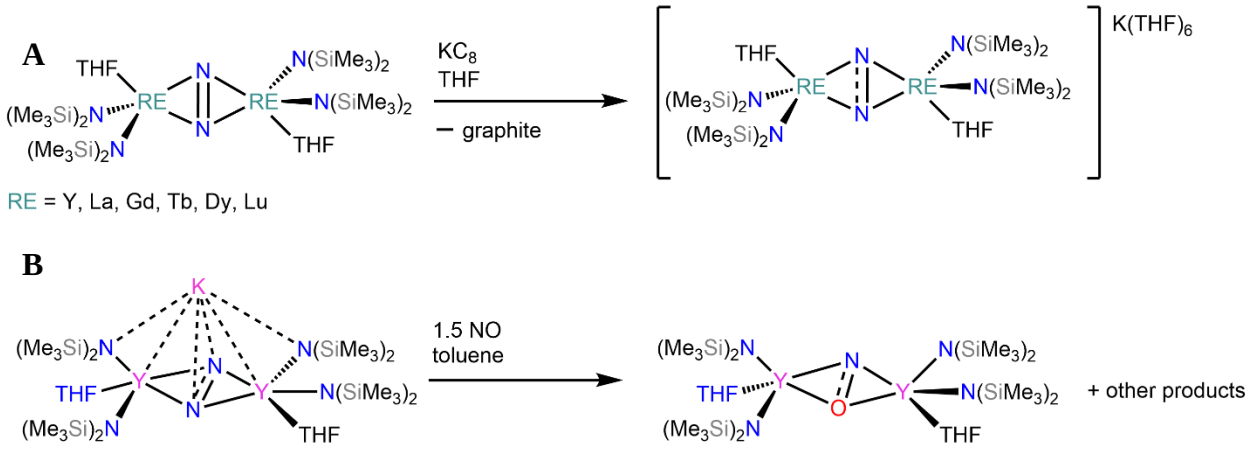

Figure 2.1. Isolation of (A) N_2^{3-} and (B) NO^{2-} anions in rare earth metal complexes.

Rare earth elements have been shown to be able to activate small molecules and generate chemical motifs unprecedented with transition metal-based complexes, but to accomplish such, the nature of the ligand is crucial for the desired reactivity. One of the most important ligands in rare earth chemistry is the cyclopentadienyl (Cp) ligand and its derivatives. The latter are prevalent in rare earth chemistry due to several reasons: (a) impart higher solubility in aprotic non-polar solvents and prevent oligomerization, (b) can access high coordination numbers, (c) high tunability through

addition of sterically demanding organic groups onto the carbon ring atoms, (d) anionic charge of the Cp ring leads to strong electrostatic interaction with the rare earth metal cation. Rare earth metal cyclopentadienyl complexes have been utilized in the activation of small molecules, as shown in Figure 2.2. Figure 2.2A demonstrates the RE-mediated reduction of dinitrogen via addition of KC_8 to the $((Cp^{Me4H})_2RE(BPh_4)$ complex to yield the $(Cp^{Me4H}{}_2RE(THF))_2(\mu\text{-}N_2)$ complex, RE = Tb, Dy. These dinitrogen complexes can then be further reduced with another molar equivalent of KC_8 in the presence of 2.2.2 cryptand (crypt-222) to yield [K(crypt-222)(THF)][$(Cp^{Me4H}{}_2RE(THF))_2(\mu{-}N_2^{\bullet})$]. The latter were treated with 2-Me-THF and crystallized from concentrated solutions to yield the[K(crypt-222)][$(Cp^{Me4H}{}_2RE)_2(\mu{-}N_2^{\bullet})$] , (where RE = Tb, Dy).[14] Rare earth elements were also used to isolate the first ever example of a Bi_2^{3-} radical unit in a metal complex for any *d*- or *f*- block element using the procedure shown in Figure 2.2B. This was achieved via reaction of 8 molar equiv. of $(Cp^*)_2RE(BPh_4)$, where $Cp^* = CpMe_5$, with 2 molar equiv. KC_8 under Ar to yield a bismuth bridging dilanthanide complex containing the Bi_2^{2-} bridging moiety. These complexes can then be further reduced with another molar equivalent of KC_8 in THF in the presence of 2.2.2 cryptand to yield the corresponding [K(crypt-222)][$(Cp^*{}_2RE)_2(\mu\text{-}\eta^2\text{:}\eta^2\text{-}Bi_2^{\bullet})$]·2 THF complexes.[3] These few examples demonstrate the potential for reactivity and activation of small molecules using rare earth metal complexes that are supported by cyclopentadienyl ligand scaffolds.

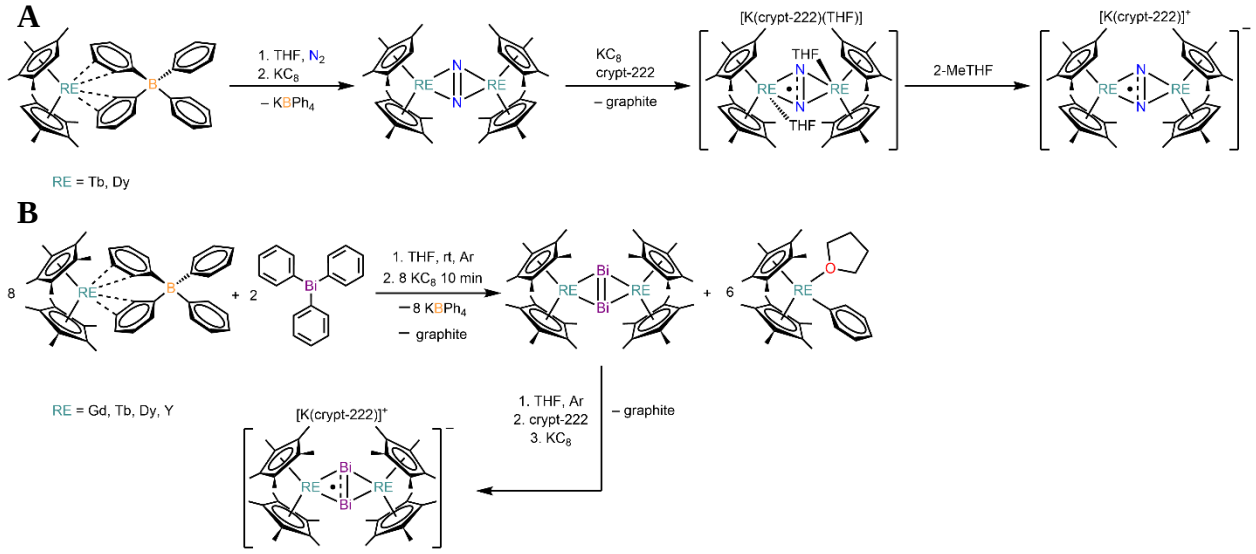

Figure 2.2. (A) Synthesis of the N_2^{3-} radical bridged complex from the $(Cp^{Me4H})_2RE(BPh_4)$ complex. (B) Synthetic route towards the first isolation of an activated Bi_2^{3-} radical bridged complex.

2.3 Bismuth Activation in Rare Earth Metal Complexes

Activation of elemental bismuth and reactivity studies on small bismuth species using the *d*- and *f*- block elements have been a growing field of research due to aforementioned electronic properties of bismuth. The second chapter will focus on the isolation and investigation of the bismuth analogues of dinitrogen in organometallic complexes in multiple oxidation states as shown in Figure 2.3. Diatomic bismuth moieties have been isolated in various metal or main group element complexes in oxidation states similar to what has been reported for analogous dinitrogen complexes. However, the $Bi_2^{1-\bullet}$ radical anion remains yet to be isolated in any molecular compound and is a therefore sought-after goal in the research of diatomic bismuth.

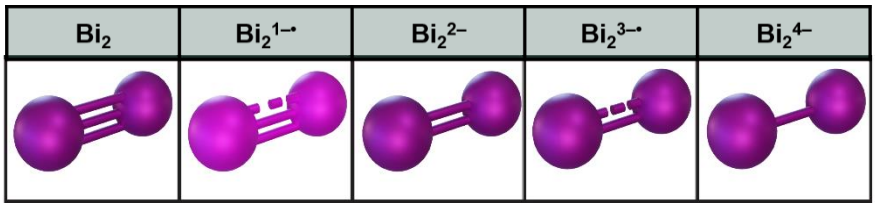

Figure 2.3. Diatomic bismuth moieties in oxidation states of 1– to 4– analogous to d N_2. The light shade of purple indicates units not previously isolated in a main group element complex. Dark purple indicates its isolation in a main group element complex.

The challenge with isolation of these diatomic bismuth species is that, unlike dinitrogen, diatomic bismuth does not exist in ambient conditions. However, diatomic bismuth can be obtained at extremely high temperatures and has previously been isolated through vaporization of elemental bismuth in an evacuated quartz tube at 1200 °C.[15] Stabilization of the fleeting diatomic bismuth unit can be achieved in the presence of metal atoms in organometallic molecular compounds. The rare earth elements serve as excellent candidates to stabilize these anionic bismuth units due to their high electropositivity and tendency to form complexes of high coordination number.[10] Examples of rare earth metal complexes being able to stabilize anionic bismuth bridges are shown in Figure 2.B and in Figure 2.4. Figure 2.4A shows the seminal work by Evans et al. where the first side-on coordinated Bi_2 moiety between two metals was isolated using the decamethyl samarocene complex.[16] Figure 2.4B demonstrates the successful use of rare earth metal complexes to isolate the first lanthanide complex where the lanthanide centers are bridged by a anionic Bi_6^{6-} core.[17] It is known in literature that the unique bonding properties of the rare earth elements allow for the isolation of seldom seen chemical motifs in molecular complexes, as shown by their use in

the first isolations of the N_2^{3-}, $(NO)^{2-}$, and Bi_2^{3-} radical anions for any *d*- or *f*- block element.

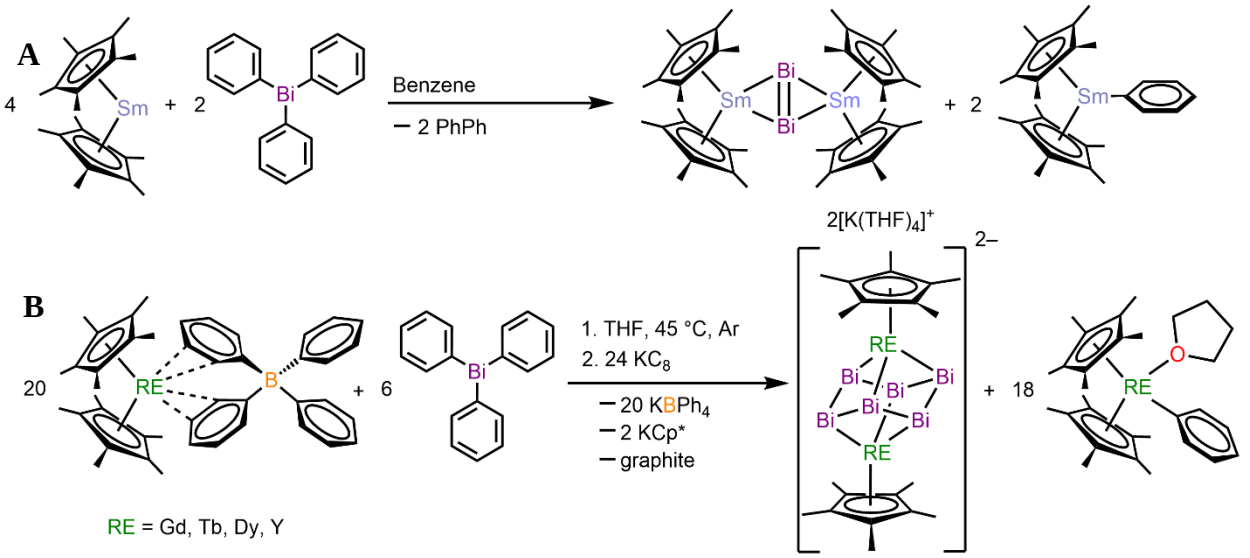

Figure 2.4. Examples of bismuth bridging rare earth metal complexes. (A) First published example of a dibismuth complex in which the diatomic bismuth unit is coordinated side-on in a planar bonding mode to two metals (B) Isolation of the first dilanthanide complex where the two lanthanide centers are bridged by a Bi_6^{6-} core.

Fifteen lanthanides alongside scandium and yttrium comprise the rare earth elements, and as such, selection of the appropriate rare earth element is an important choice when deciding which element should be used to isolate the diatomic bismuth units in metal complexes. Shown in Figure 2.2B are the rare elements used in the synthesis of the $[K(crypt\text{-}222)][(Cp^*_2RE)_2(\mu\text{-}\eta^2\text{:}\eta^2\text{-}Bi_2^{\bullet})]\cdot 2THF$ complex, which were gadolinium, terbium, dysprosium, and yttrium in order of decreasing ionic radii. Hence, the next lanthanide in this series would be holmium, with an ionic radii of 1.155 Å, to determine if the Bi_2 moiety is accessible with each rare earth element and if it is, what oxidation states of that bridge are accessible with each rare earth element.[18] If that proves successful, the chemical oxidation and reduction of the Bi_2^{2-} unit would be attempted with the goal of isolating Bi_2 motifs with charges spanning –1 to –4. Monooxidation of Bi_2^{2-} in the systems would afford a currently unknown Bi_2^{1-} complex, a result which will be of great interest to both the main-group and organometallic community. In all cases, investigation of the influence of the charge of the Bi_2^{n-} (n = 1, 2, 3, 4) unit will be of fundamental interest. Thus, the synthesis of the Ho analog of Bi_2^{2-} complexes and its selective mono-oxidation and -reduction to give Bi_2^{1-} and Bi_2^{3-} complexes, as illustrated in Figure 2.5, is an exciting aim.

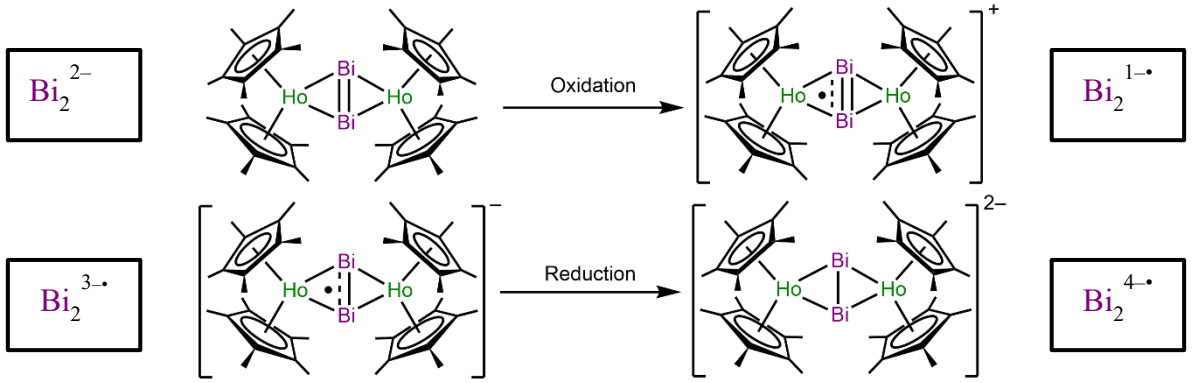

Figure 2.5. Diatomic bismuth compounds where the Bi_2 moiety exists in oxidation states from -1 to -4, which are obtained through oxidation and reduction reactions.

In addition to using the next smallest, rare earth element in the series following yttrium and dysprosium, holmium itself has interesting physical properties that make it an interesting choice for this synthetic strategy. The Ho^{III} ion shows interesting spectroscopic applications as it can have up-conversion of its luminescence in the presence of 4f metal ions owing to its weak f-f transition. Holmium also exhibits an efficient luminescent re-absorption effect due to its many absorption peaks in the visible range. These absorption peaks can strongly be influenced by temperature leading to hot bands that are thermally dependent. This allows for opportunities to probe the holmium bismuth complexes using luminescence or the temperature dependence of its absorptions.[19] Aside from these spectroscopic properties, holmium also has historically been one of the most important rare earth magnetic elements used industrially in the form of holmium intermetallic compounds.[20] Interestingly, there are also no molecular compounds known containing a holmium–bismuth bond, so the isolation of such would be monumental.

2.4 Experimental

General Information All manipulations mentioned herein were conducted under inert argon atmosphere to exclude moisture or oxygen using Schlenk line and glovebox techniques. House nitrogen was purified through a MBraun HP–500–MO–OX gas purifier prior to use. *n*-hexane was dried by refluxing over calcium hydride and distilled before use. Tetrahydrofuran and toluene were dried by refluxing over elemental potassium. All solvents were tested for the presence of water and oxygen with a drop of sodium benzophenone radical solution in the glovebox. Potassium bis(trimethylsilyl)amide ($KN(SiMe_3)_2$) was purchased from Sigma-Aldrich, dissolved in toluene, centrifuged, filtered, and recrystallized at –35 °C. Pentamethylcyclopentadienyl ($CpMe_5H$) was purchased from Sigma-Aldrich and dried over 4 Å molecular sieves. Triphenylbismuth and 2.2.2-cryptand (crypt-222) were purchased from Sigma-Aldrich and recrystallized from hexane. Allyl magnesium chloride (2.0 M in THF) and anhydrous $HoCl_3$ were purchased from Sigma-Aldrich and used as received. Potassium graphite was prepared according to literature procedures.[21] IR spectra were recorded with an Cary 630 diamond ATR–IR spectrometer in a nitrogen atmosphere. A PerkinElmer 2400 Series II CHNS/O analyzer was used for CHN elemental analyses.

X–ray Crystallography Data was collected at a XtaLAB Synergy, Dualflex, HyPix diffractometer equipped with an Oxford Cryosystems low-temperature device, operating at T = 100 K using MoKα radiation. Data were measured using omega and phi scans of 1.0° per frame for 30 s. Cell parameters were retrieved using CrysAlisPro (Rigaku, V1.171.41.90a, 2020) software and refined using CrysAlisPro (Rigaku, V1.171.41.90a, 2020). Data reduction was performed using the CrysAlisPro (Rigaku, V1.171.41.90a, 2020) software.

Synthesis of $KCpMe_5$. $KCpMe_5$ was synthesized according to the literature procedure.[21] Under dry argon atmosphere, $CpMe_5H$ (2.91 g, 0.02 mol) was dissolved in 20 mL toluene in a 200 mL Schlenk flask. While stirring, a solution of $KN(SiMe_3)_2$ (4.993 g, 0.03 mol) in 20 mL toluene was added to the reaction flask, and this was stirred for 2 h. The solution was then filtered through a glass frit, and the solid washed with 20 mL hexane. The solid was then dried *in vacuo* to afford a white solid in 76% yield (2.89 g).

Synthesis of $Cp^*_2Ho(\mu\text{-}Cl_2)K$, ***A***. Compound **A** was synthesized according to the literature procedure.[21, 22] Under dry argon atmosphere, $HoCl_3$ (1.96 g, 0.01 mol) and KCp^* (2.45 g, .0.01 mol) was dissolved in 80 mL of THF in a 100 mL round bottom flask. The reaction mixture was

stirred for 12 h resulting in a color change from reddish pink to orange. The solution was filtered through a glass frit to remove the white insoluble solids. The filtrate was then dried *in vacuo*. This solid was then washed with 4 x 40 mL of toluene to remove any toluene-soluble impurities. After toluene washes, the solid was then dried *in vacuo* for 1 hour at ambient temperature followed by during under vacuum at 70°C for 2 h to remove any coordinating THF. This affords $Cp^*_2Ho(\mu\text{-}Cl_2)K$ as a pale red solid in 85% yield (3.32 g)

Synthesis of $Cp^*2Ho(\eta^3\text{-}C_3H_5)$, ***B***. Compound **B** was synthesized according to the literature procedure.[21,22] Under dry argon atmosphere, $Cp^*_2Ho(\mu\text{-}Cl_2)K$ (3.26 g, 0.01 mol) was added to a 250 mL round bottom flask with 20 mL toluene to form a slurry. To this mixture, allylmagnesium chloride (2.84 mL of a 2.0 M solution in THF) was added dropwise over the course of 10 minutes while stirring, which turned the solution from pale red to an orange-brown color. Solution was stirred for 2 h before volatiles were removed *in vacuo*. Once dried, the solid was triturated with 3 x 20 mL of 1,4 dioxane in hexane mixture (1:10). The solids were filtered through celite into another 250 mL round bottom flask where the volatiles were removed *in vacuo*. Bright orange crystals of B suitable for X–ray analysis were obtained at –35 °C from a concentrated toluene solution in 76% crystalline yield (2.84 g).

Synthesis of $[Cp^*_2Ho][(\mu\text{-}Ph_2)BPh_2]$, ***C***. Compound **C** was synthesized according to the literature procedure.[21, 22] Under dry argon atmosphere, $Cp^*_2Ho(\eta^3\text{-}C_3H_5)$ (2.93 g, 0.01 mol) was dissolved in 40 mL toluene in a 250 mL Schlenk flask. Once fully dissolved, $[HNEt_3][BPh_4]$ (2.20 g, 0.01 mol) was transferred to the reaction flask. The reaction was stirred for 1 hour with the glass stopper off to allow for release of propene gas and then stirred for another hour with the glass stopper on. After stirring, the colorless solid was removed via filtration to yield a yellow filtrate. The solid was dried *in vacuo* to produce $[Cp^*_2Ho][(\mu\text{-}Ph_2)BPh_2]$ as a yellow powder in 67% yield (4.10 g).

Synthesis of $(Cp^*_2Ho)_2(\mu\text{-}\eta^2\text{:}\eta^2\text{-}Bi_2)$, ***1***. Under dry argon atmosphere, $[Cp^*_2Ho][(\mu\text{-}Ph_2)BPh_2]$ (0.17 g, 0.22 mmol) was dissolved in 4 mL THF followed by the addition of a solution of triphenylbismuth (0.02 g, 0.06 mmol) dissolved in 2 mL THF. A suspension of potassium graphite (0.03 g, 0.22 mmol) in 1 mL THF was transferred to the reaction mixture causing an immediate color change of the solution from light yellow to maroon. The reaction was stirred at ambient temperature for 15 minutes to yield a dark, maroon-colored solution. The reaction vial was then cooled in a Coldwell with dry ice. Once the reaction cooled for 20 minutes, the red solution was

filtered to remove the insoluble graphite and $KBPh_4$ precipitates. The filtrate was then dried *in vacuo* in the Coldwell over 3 h. The resulting solid was then washed with 3 x 2 mL hexane to remove the hexane soluble $Cp^*_2Ho(Ph)(THF)$ byproduct to yield a reddish–brown residue in 54% yield (0.053 g). Dark red crystals of **1** suitable for X–ray analysis were grown at –35 °C from layering hexane over a concentrated toluene solution in 8% crystalline yield (0.003 g) based on elemental bismuth analysis. Anal. Calcd for $C_{40}H_{60}Ho_2Bi_2$: C 37.27, H 4.69, N 0. Found: C 37.14, H 4.13, N 0.19.

2.5 Results and Discussion

The $Cp^*_2Ho(BPh_4)$ complex, where Cp^* = pentamethylcyclopentadienyl, was synthesized via literature procedures, as is shown in Scheme 2.1. The first step involves the complexation of KCp^* to $HoCl_3$ in THF through a salt metathesis reaction to yield the "salt-like" compound, $Cp^*_2Ho(\mu\text{-}Cl_2)K$ (**A**). **A** was then reacted with allyl magnesium chloride to obtain the $Cp^*2Ho(\eta^3\text{-}C_3H_5)$ (**B**) alkyl complex through another salt metathesis reaction. Lastly, displacement of the allyl is completed through reaction with $[HNEt_3][BPh_4]$ to yield the $Cp^*_2Ho(BPh_4)$ compound (**C**). The utility of using $Cp^*_2Ho(BPh_4)$ complex comes from the weakly coordinating tetraphenylborate ligand that is bound to the lanthanide center through agostic interactions. This allows it to be easily displaced by any incoming ligands, while also being a sterically bulky ligand that occupies a large amount of equatorial space in the coordination sphere of the lanthanide.

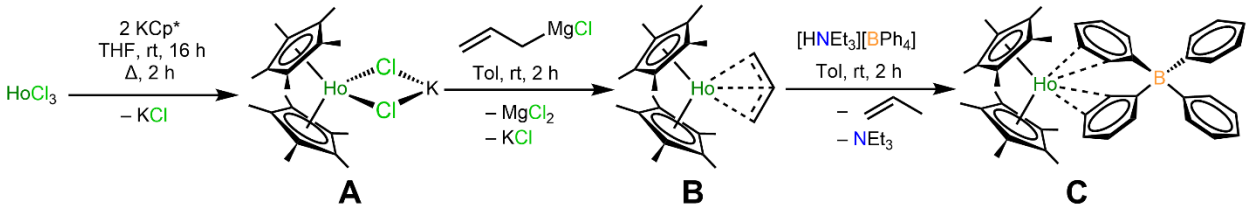

Scheme 2.1. Synthesis for the $[Cp^*_2Ho][(\mu\text{-}Ph_2)BPh_2]$ complex from $HoCl_3$

As shown in scheme 2.2, eight molar equivalents of $Cp^*_2Ho(BPh_4)$ is then allowed to react with two molar equivalents triphenyl bismuth at –78 °C in THF solution, followed by addition of eight molar equivalents of potassium graphite (KC_8) as a reductant to reduce Bi^{III} to Bi^{-I} to yield the hexane soluble $Cp^*_2Ho(Ph)(THF)$, **2**, and toluene soluble $(Cp^*_2Ho)_2(\mu\text{-}\eta^2\text{:}\eta^2\text{-}Bi_2)$,**1**, complexes in addition to graphite and potassium tetraphenylborate precipitate. Solubility differences are utilized to separate the two complexes from each other through fractional recrystallization. Dark red crystals of **1** were grown from a concentrated toluene solution at –35 °C. The molecular structure of the synthesized compound was confirmed via single-crystal X-ray diffraction analysis, as shown in Figure 2.6. To my knowledge, this is the first molecular holmium–bismuth compound characterized.

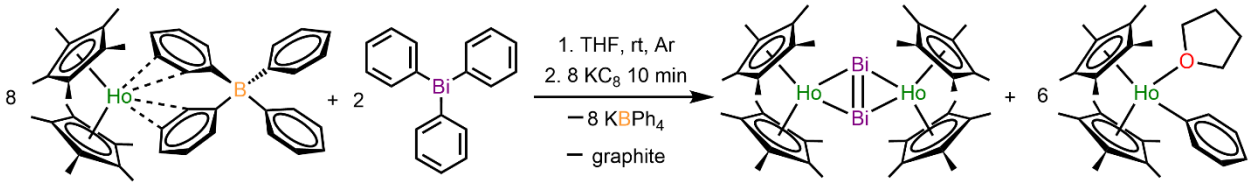

Scheme 2.2. Synthesis of $(Cp^*_2Ho)_2(\mu\text{-}\eta^2\text{:}\eta^2\text{-}Bi_2)$ from $Cp^*_2Ho(BPh_4)$.

The $(Cp^*_2Ho)_2(\mu\text{-}\eta^2\text{:}\eta^2\text{-}Bi_2)$ crystallizes in the $P2_1$ space group and is isostructural to similarly reported $(Cp^*_2RE)_2(\mu\text{-}\eta^2\text{:}\eta^2\text{-}Bi_2)$ complexes.[3] As shown in Figure 2.6, each lanthanide ion is eightfold coordinated to the two η^5-Cp^* and each bismuth atom of the Bi_2^{2-} bridge. There is a nearly coplanar arrangement of the Bi_2^{2-} bridge with the two lanthanide centers. The Bi–Bi distance is 2.842(1) Å, which is in accordance with a Bi=Bi double bond observed in other compounds.[16, 23] The mean Ho–Bi distance is 3.191(1) Å, which is shorter than the analogous yttrium complex, due to lanthanide contraction.[3] The mean $Cp^*_{centroid}$–Ho–$Cp^*_{centroid}$ angle is 135.9° similar to other complexes with the Cp^*_2RE moieties.[3]

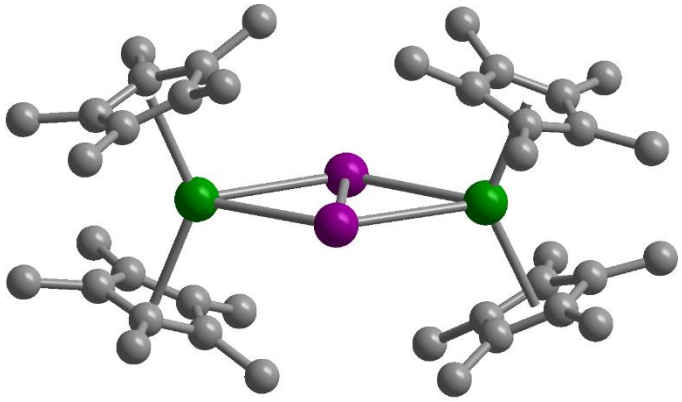

Figure 2.6. Structure of **1** in a crystal of $(Cp^*_2Ho)_2(\mu\text{-}\eta^2\text{:}\eta^2\text{-}Bi_2)$. Green, purple, and gray ellipsoids represent holmium, bismuth, and carbon atoms, respectively. H atoms have been omitted for clarity. Selected distances (Å) and angles (deg) are as follows: Bi–Bi = 2.842(1), mean Ho–Bi = 3.191(1), Ho–Ho = 5.772(2), mean Cp^*_{cent}–Ho–Cp^*_{cent} = 135.9(1).

The main features of the IR spectrum of **1** are stretching modes around 2800 – 3000 cm^{-1} for the CH_2 groups of the cyclopentadienyl ring and around 1370 cm^{-1} corresponding to the methyl groups on Cp^*, Figure 2.7. Compared to other $(Cp^*_2RE)_2(\mu\text{-}\eta^2\text{:}\eta^2\text{-}Bi_2)$ species there are minimal differences in spectrum as the RE used is changed.

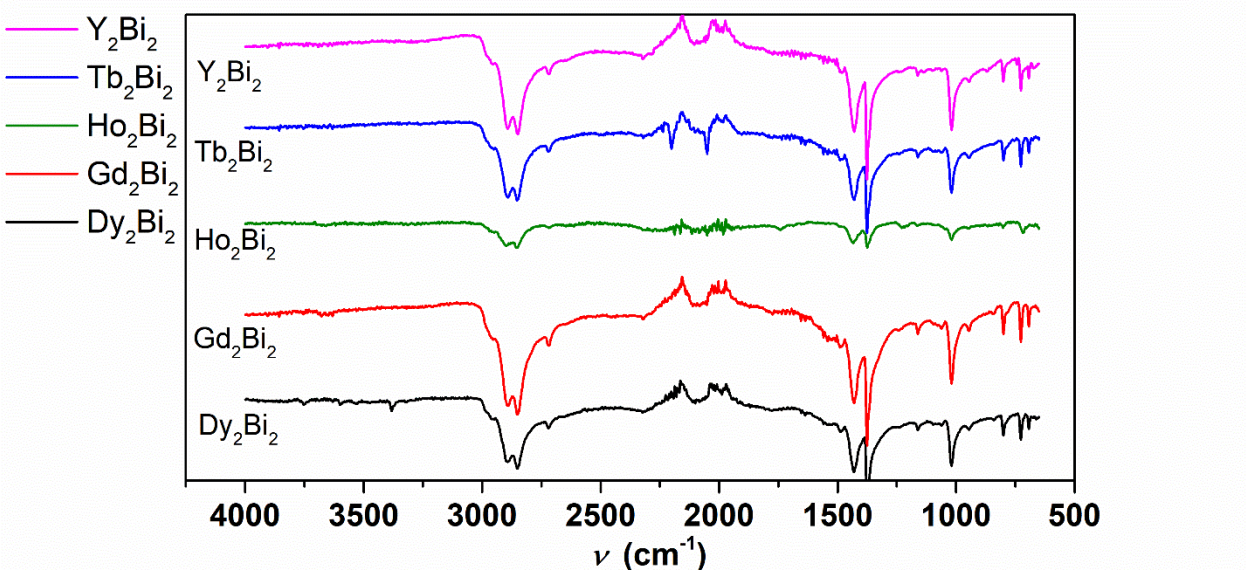

Figure 2.7. IR spectrum of $(Cp^*_2RE)_2(\mu\text{-}\eta^2\text{:}\eta^2\text{-}Bi_2)$ (RE = Y, pink), (RE = Tb, blue), (RE = Ho (**1**), green), (RE = Gd, orange), (RE = Dy, black)

Crystals of the hexane soluble $Cp^*_2Ho(Ph)(THF)$ complex were grown from a concentrated hexane solution at –35 °C. The molecular structure of the synthesized compound was confirmed via single crystal X-ray diffraction analysis and is shown in Figure 2.8, which is to the best of our knowledge, the first report of a crystal structure for **2**. $Cp^*_2Ho(Ph)THF$ crystallizes in the $P2_1/c$ space group and is isostructural to similarly reported $Cp^*_2RE(Ph)(THF)$ complexes.[3] As shown in Figure 2.8, each lanthanide is eightfold coordinated to the two η^5-Cp^*, the oxygen atom in THF, and η^1-Ph.

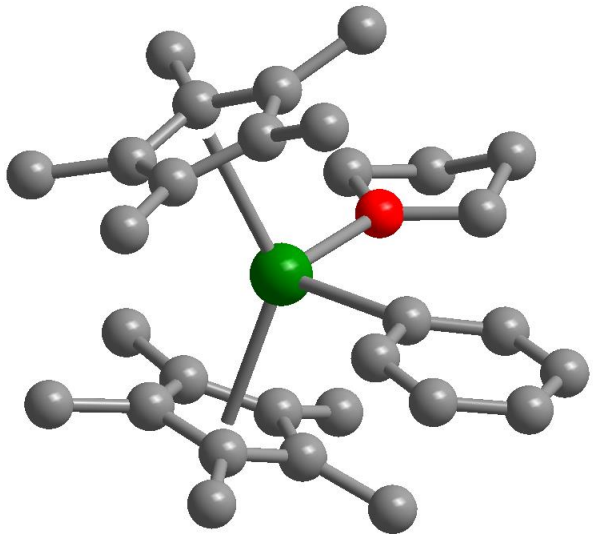

Figure 2.8. Structure of **2** in a crystal of $Cp^*_2Ho(Ph)THF$). Green, red, and gray ellipsoids represent holmium, oxygen, and carbon atoms, respectively. H atoms have been omitted for clarity. Selected distances (Å) and angles (deg) are as follows: Ho–O = 2.387(2), Ho–Ph = 2.444(3), Ho–centroid = 2.390(1), Cp^*_{cent}–Ho–Cp^*_{cent} = 135.8(1).

The Ho–O, Ho–Ph, and mean Ho centroid distance (Å) is 2.387, 2.444, and 2.390, respectively. The Cp^*_{cent}–Ho–Cp^*_{cent} (cent = centroid) angle is 135.8(1) ° similar to other complexes with the Cp^*_2RE moieties.

Synthesis of **1** is challenging due to the strong oxophilicity of the lanthanides that cause lanthanide complexes to be highly susceptible ro reactions with trace moisture and air. This was evidenced by the decomposition of $(Cp^*_2Ho)_2(\mu\text{-}\eta^2\text{:}\eta^2\text{-}Bi_2)$ to the $(Cp^*_2Ho)_2(\mu\text{-}\eta^1\text{-}O)$, **3**, complex when left at ambient temperature, where $(Cp^*_2Ho)_2(\mu\text{-}\eta^2\text{:}\eta^2\text{-}Bi_2)$ reacts with trace moisture or oxygen in the glovebox. This complex was crystallographically characterized via single-crystal X-ray diffraction analysis and shown in Figure 2.9, which is to the best of our knowledge, the first report of a crystal structure for **3**. It crystallizes in the $I\bar{4}2m$ space group and each lanthanide is sevenfold coordinated to the two η^5-Cp^* and the bridging oxygen atom, Figure 2.9. The Ho–O–Ho, Ho–O and mean Ho–centroid distance (Å) are 4.107(1), 2.054(1), and 2.390(3), respectively. The much shorter Ho–O–Ho distance forces one of the metallocene moieties to rotate out of plane due to the much closer proximity of the metallocenes that is induced from the much smaller bridging oxygen atom. The Cp^*_{cent}–Ho–Cp^*_{cent} angle (cent = centroid) is 135.8(1) ° similar to other complexes with the Cp^*_2RE moieties.

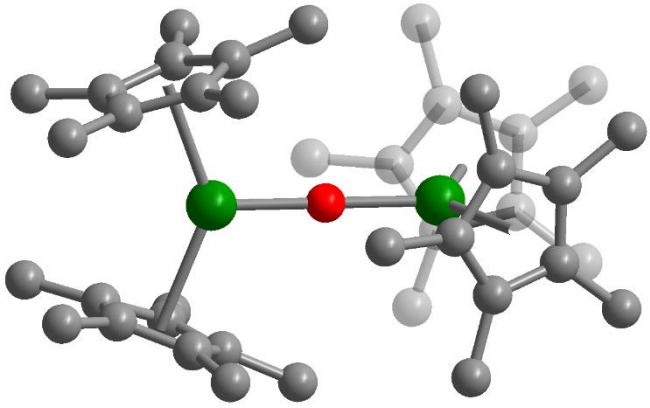

Figure 2.9. Structure of **3** in a crystal of $(Cp^*_2Ho)_2(\mu\text{-}\eta^1\text{-}O)$. Green, red, and gray ellipsoids represent holmium, oxygen, and carbon atoms, respectively. H atoms have been omitted for clarity. Selected distances (Å) and angles (deg) are as follows: Ho–O –Ho = 4.107(1) mean Ho–O = 2.054(1), mean Ho–centroid = 2.390(1), mean Cp^*_{cent}–Ho–Cp^*_{cent} = 135.8(1).

2.6 Conclusion

The multistep synthesis of the $Cp^*_2Ho(BPh_4)$ complex was completed and was then followed by a reaction with triphenyl bismuth and KC_8 to generate the novel $(Cp^*_2Ho)_2(\mu\text{-}\eta^2\text{:}\eta^2\text{-}Bi_2)$ complex. This compound was then crystallographically characterized with single-crystal X-ray diffraction analysis and represents the first Ho–Bi bond characterized in a molecular compound. Following this synthesis, the next step going forward is the reduction of oxidation of this complex to generate a series of complexes with identical topologies where only the oxidation state of the bismuth bridge changes. Oxidation of the $(Cp^*_2Ho)_2(\mu\text{-}\eta^2\text{:}\eta^2\text{-}Bi_2)$ complex is expected to yield a similar complex but with a radical Bi_2^{1-} bridge, which would be the first time such an oxidation state would be isolated for a diatomic bismuth bridge, and this result would be of great interest to both main group and organometallic chemists. Similarly, reduction of the $(Cp^*_2Ho)_2(\mu\text{-}\eta^2\text{:}\eta^2\text{-}Bi_2)$ should yield the radical Bi_2^{3-} bridged complex, which could bear interesting magnetic properties such as single molecule magnetism exhibited by other rare earth analogue of such a complex. This could then be followed by another electron reduction to yield a complex with a Bi_2^{4-} bridge, and this would be the first time such a complex would have been isolated for any lanthanide or transition metal making the result very exciting for organometallic chemists. Finally, another avenue that could be explored is how the properties of these $(Cp^*_2RE)_2(\mu\text{-}\eta^2\text{:}\eta^2\text{-}Bi_2)$ changes from one rare earth to another and how their physical properties change when the oxidation state of the bismuth bridge is altered. This would allow for greater understanding of the interaction between bismuth with the rare earth elements and could be an important step in making novel organometallic bismuth complexes that bear intriguing physical properties owing to the unique properties of bismuth itself and its interaction with the rare earth elements.

REFERENCES

1. Du, J.; Cobb, P. J.; Ding, J.; Mills, D. P.; Liddle, S. T. F-Element Heavy Pnictogen Chemistry. *Chem. Sci.* 2023.

2. Kanatzidis, M.; Sun, H.; Dehnen, S. Bismuth—The Magic Element. *Inorg. Chem.* 2020, 59 (6), 3341–3343.

3. Zhang, P.; Nabi, R.; Staab, J. K.; Chilton, N. F.; Demir, S. Taming Super-Reduced Bi_2^{3-} Radicals with Rare Earth Cations. *J. Am. Chem. Soc.* 2023, 145 (16), 9152–9163.

4. Whitmire, K. H. Bismuth: Inorganic Chemistry. In Encyclopedia of Inorganic and Bioinorganic Chemistry; *John Wiley & Sons, Ltd*, 2014; pp 1–32.

5. Arsenic, Antimony and Bismuth; Smith, J. D., Ed.; Pergamon Texts in Inorganic Chemistry; *Pergamon*, 1973; p 547.

6. Leonard, N. M.; Wieland, L. C.; Mohan, R. S. Applications of Bismuth(III) Compounds in Organic Synthesis. *Tetrahedron* 2002, 58 (42), 8373–8397.

7. Mato, M.; Cornella, J. Bismuth in Radical Chemistry and Catalysis. *Angew. Chem. Int. Ed.*, e202315046.

8. Mato, M.; Bruzzese, P. C.; Takahashi, F.; Leutzsch, M.; Reijerse, E. J.; Schnegg, A.; Cornella, J. Oxidative Addition of Aryl Electrophiles into a Red-Light-Active Bismuthinidene. *J. Am. Chem. Soc.* **2023**, *145*, 18742–18747.

9. Briand, G. G.; Burford, N. Bismuth Compounds and Preparations with Biological or Medicinal Relevance. *Chem. Rev.* 1999, 99 (9), 2601–2658.

10. Benner, F.; Delano, F.; R Pugliese, E.; Demir, S. 4.04 - Cyclopentadienyls and Phospholyls of the Group 3 Metals and Lanthanides. In Comprehensive Organometallic Chemistry IV; Parkin, G., Meyer, K., O'hare, D., Eds.; *Elsevier: Oxford*, 2022; pp 98–184.

11. Evans, W. J.; Fang, M.; Zucchi, G.; Furche, F.; Ziller, J. W.; Hoekstra, R. M.; Zink, J. I. Isolation of Dysprosium and Yttrium Complexes of a Three-Electron Reduction Product in the Activation of Dinitrogen, the $(N_2)^{3-}$ Radical. *J. Am. Chem. Soc.* **2009**, *131* (31), 11195–11202.

12. Evans, W. J.; Fang, M.; Bates, J. E.; Furche, F.; Ziller, J. W.; Kiesz, M. D.; Zink, J. I. Isolation of a Radical Dianion of Nitrogen Oxide $(NO)^{2-}$. *Nature Chem* **2010**, *2* (8), 644–647.

13. Wedal, J. C.; Evans, W. J. A Rare-Earth Metal Retrospective to Stimulate All Fields. *J. Am. Chem. Soc.* **2021**, *143* (44), 18354–18367.

14. Demir, S.; Gonzalez, M. I.; Darago, L. E.; Evans, W. J.; Long, J. R. Giant Coercivity and High Magnetic Blocking Temperatures for N2 3− Radical-Bridged Dilanthanide Complexes upon Ligand Dissociation. *Nat Commun* **2017**, *8* (1), 2144.

15. Almy, G. M.; Sparks, F. M. The Absorption Spectrum of Diatomic Bismuth. *Phys. Rev.* **1933**, *44* (5), 365–375.

16. Evans, W. J.; Gonzales, S. L.; Ziller, J. W. Organosamarium-Mediated Synthesis of Bismuth-Bismuth Bonds: X-Ray Crystal Structure of the First Dibismuth Complex Containing a Planar $M_2(\mu\text{-}\eta^2\text{:}\eta^2\text{-}Bi_2)$ Unit. *J. Am. Chem. Soc.* **1991**, *113* (26), 9880–9882.

17. Zhang, P.; Benner, F.; Chilton, N. F.; Demir, S. Organometallic Lanthanide Bismuth Cluster Single-Molecule Magnets. *Chem* **2022**, *8* (3), 717–730.

18. Shannon, R. D. Revised Effective Ionic Radii and Systematic Studies of Interatomic Distances in Halides and Chalcogenides. *Acta Crystallographica Section A* **1976**, *32* (5), 751–767.

19. Wang, J.; J. Zakrzewski, J.; Zychowicz, M.; Vieru, V.; F. Chibotaru, L.; Nakabayashi, K.; Chorazy, S.; Ohkoshi, S. Holmium(Iii) Molecular Nanomagnets for Optical Thermometry Exploring the Luminescence Re-Absorption Effect. *Chem. Sci.* **2021**, *12* (2), 730–741.

20. Liu, K.; Liu, Y.-L.; Yuan, L.-Y.; Wang, L.; Wang, L.; Li, Z.-J.; Chai, Z.-F.; Shi, W.-Q. Thermodynamic and Electrochemical Properties of Holmium and HoxAly Intermetallic Compounds in the LiCl-KCl Eutectic. *Electrochimica Acta* **2015**, *174*, 15–25.

21. Evans, W. J.; Kozimor, S. A.; Ziller, J. W.; Kaltsoyannis, N. Structure, Reactivity, and Density Functional Theory Analysis of the Six-Electron Reductant, $[(C_5Me_5)_2U]_2(\mu\text{-}H_6\text{:}H_6\text{-}C_6H_6)$, Synthesized via a New Mode of $(C_5Me_5)_3M$ Reactivity. *J. Am. Chem. Soc.* **2004**, *126* , 14533–14547.

22. Demir, S.; Meihaus, K. R.; Long, J. R. Slow Magnetic Relaxation in a Neodymium Metallocene Tetraphenylborate Complex. *Journal of Organometallic Chemistry* **2018**, *857*, 164–169.

23. Evans, W. J.; Seibel, C. A.; Ziller, J. W. Unsolvated Lanthanide Metallocene Cations $[(C_5Me_5)_2Ln][BPh_4]$: Multiple Syntheses, Structural Characterization, and Reactivity Including the Formation of $(C_5Me_5)_3Nd$[1]. *J. Am. Chem. Soc.* **1998**, *120* , 6745–6752. Prabusankar, G.; Gemel, C.; Parameswaran, P.; Flener, C.; Frenking, G.; Fischer, R. A. A Short Bi=Bi Bond Supported by a Metalloid Group 13 Ligand. *Angew. Chem. Int. Ed.* **2009**, *48*, 5526–5529.

24. Demir, S.; Zadrozny, J. M.; Nippe, M.; Long, J. R. Exchange Coupling and Magnetic Blocking in Bipyrimidyl Radical-Bridged Dilanthanide Complexes. *J. Am. Chem. Soc.* **2012**, *134* (45), 18546–18549.

APPENDIX

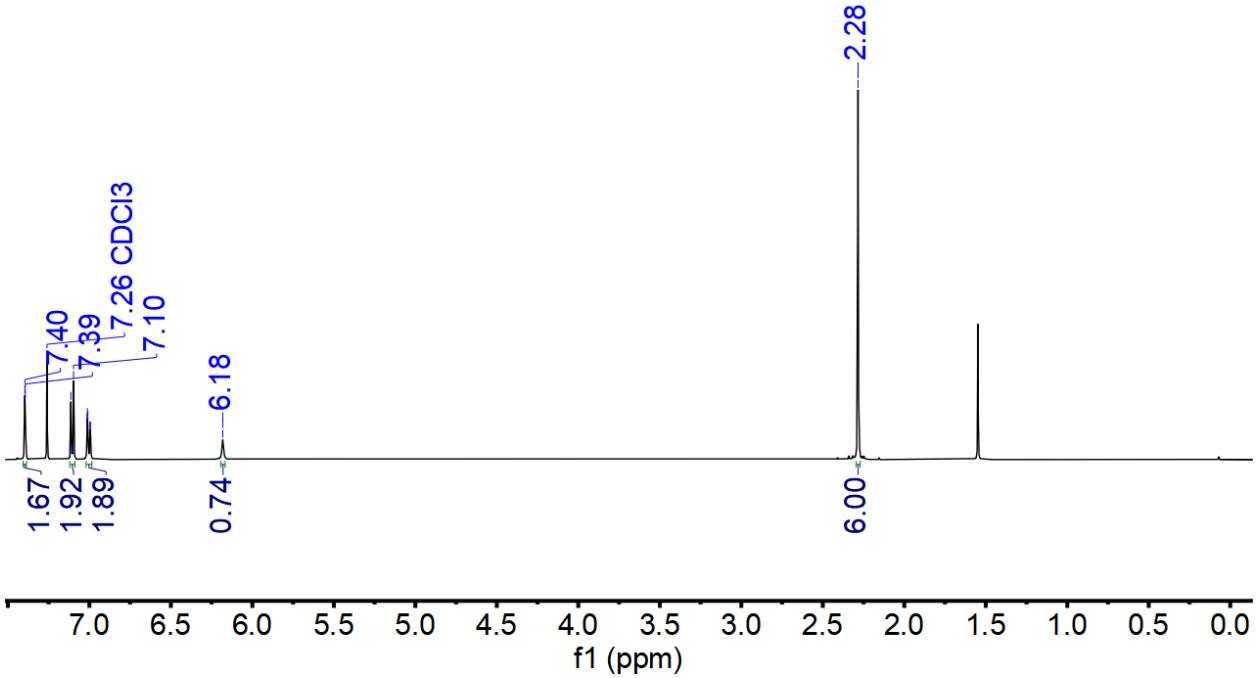

Figure S1. ^{1}H NMR of Bis(2-bromo-4-methylphenyl) amine (500 MHz, ppm, $CDCl_3$, 25 °C) δ: 7.40 (d, 2H, *H*–Ph, $^{4}J_{H\text{-}H}$: 2.0 Hz), 7.11 (d, 2H, *H*–Ph, $^{3}J_{H\text{-}H}$: 8.2 Hz), 7.00 (dd, 2H, *H*–Ph, $^{3}J_{H\text{-}H}$ = 8.2 Hz, $^{4}J_{H\text{-}H}$: 1.9 Hz), 6.18 (s, 1H, *H*–N), 2.28 (s, 6H, Ph–*Me*).

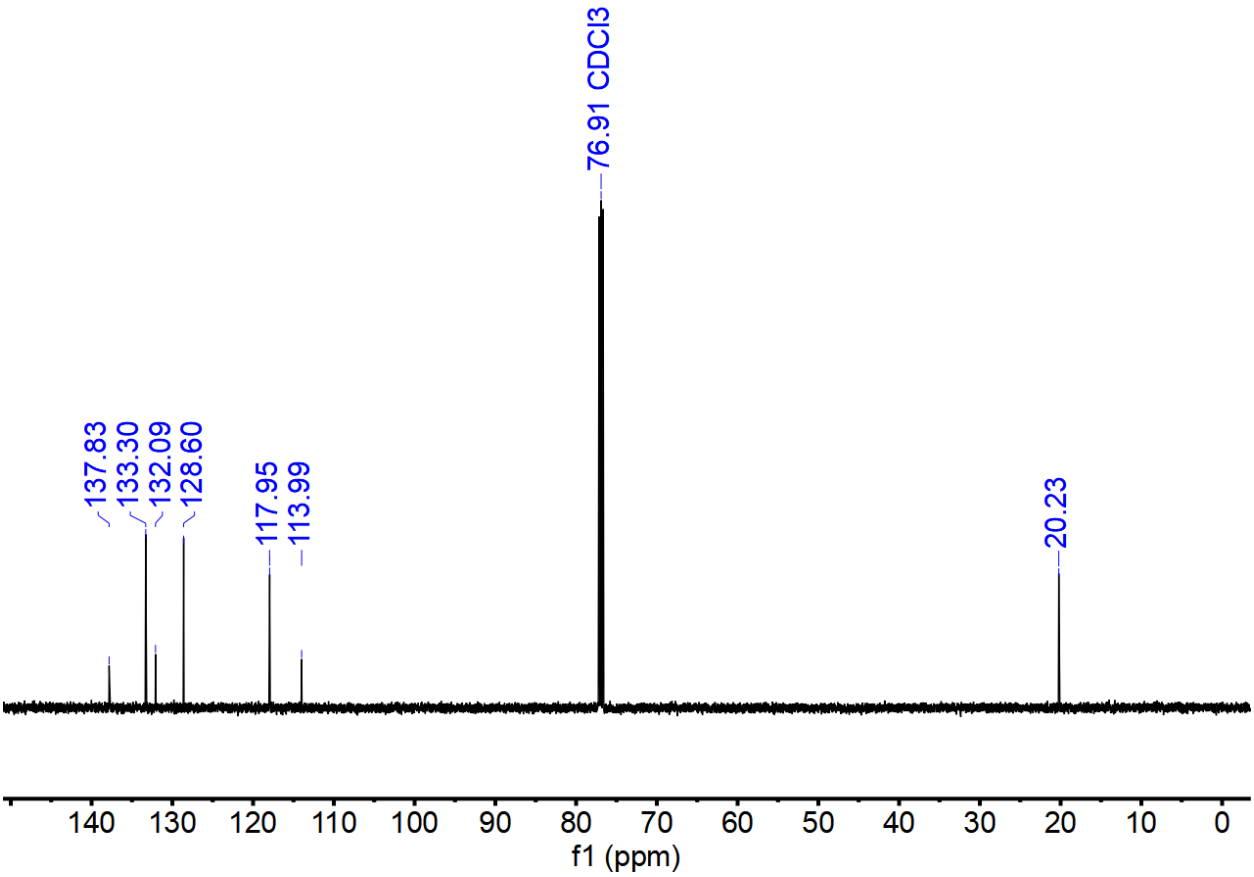

Figure S2. ^{13}C NMR of Bis(2-bromo-4-methylphenyl) amine (126 MHz, ppm, $CDCl_3$, 25 °C) δ: 137.83, (*C*–N) 133.30, (*Ph*), 132.09 (*Ph*), 128.60, (*Ph*), 117.95 (*Ph*), 113.99 (*Ph*), 20.23 (Ph–*Me*)

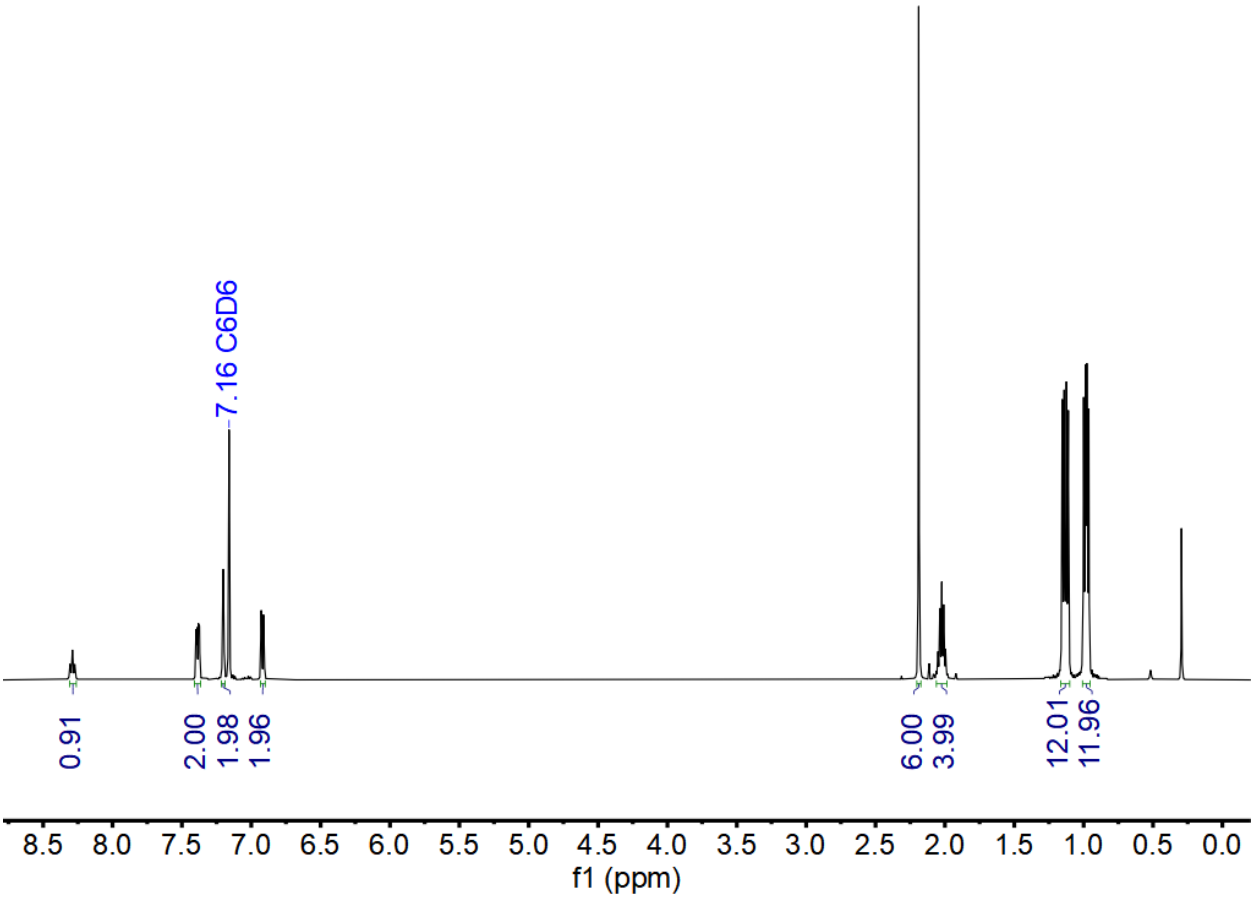

Figure S3. ^{1}H NMR of PNP(H) (500 MHz, ppm, benzene-d$_6$, 25 °C)δ: 8.31 (t, 1H, *H*–N, $^{4}J_{P\text{-}H}$: 8.5 Hz), 7.40 (dd, 2H, *H*–Ph, $^{3}J_{H\text{-}H}$: 8.4 Hz, $^{4}J_{H\text{-}H}$: 4.1 Hz), 7.20 (d, 14 H, *H*–Ph, $^{3}J_{H\text{-}H}$: 2.6 Hz), 6.92 (dd, 2 H, *H*–Ph, $^{3}J_{H\text{-}H}$: 8.4 Hz, $^{4}J_{H\text{-}H}$: 2.1 Hz), 2.19 (s, 6H, Ph–*Me*), 2.02 (m, 4H, *CH*Me$_2$), 1.13 (dd, 12 H, CH*Me*$_2$, $^{3}J_{H\text{-}H}$: 15.1 Hz, $^{4}J_{H\text{-}H}$: 7.0 Hz), 0.98 (dd, 12 H, CH*Me*$_2$, $^{3}J_{H\text{-}H}$: 11.7 Hz, $^{4}J_{H\text{-}H}$: 6.9 Hz).

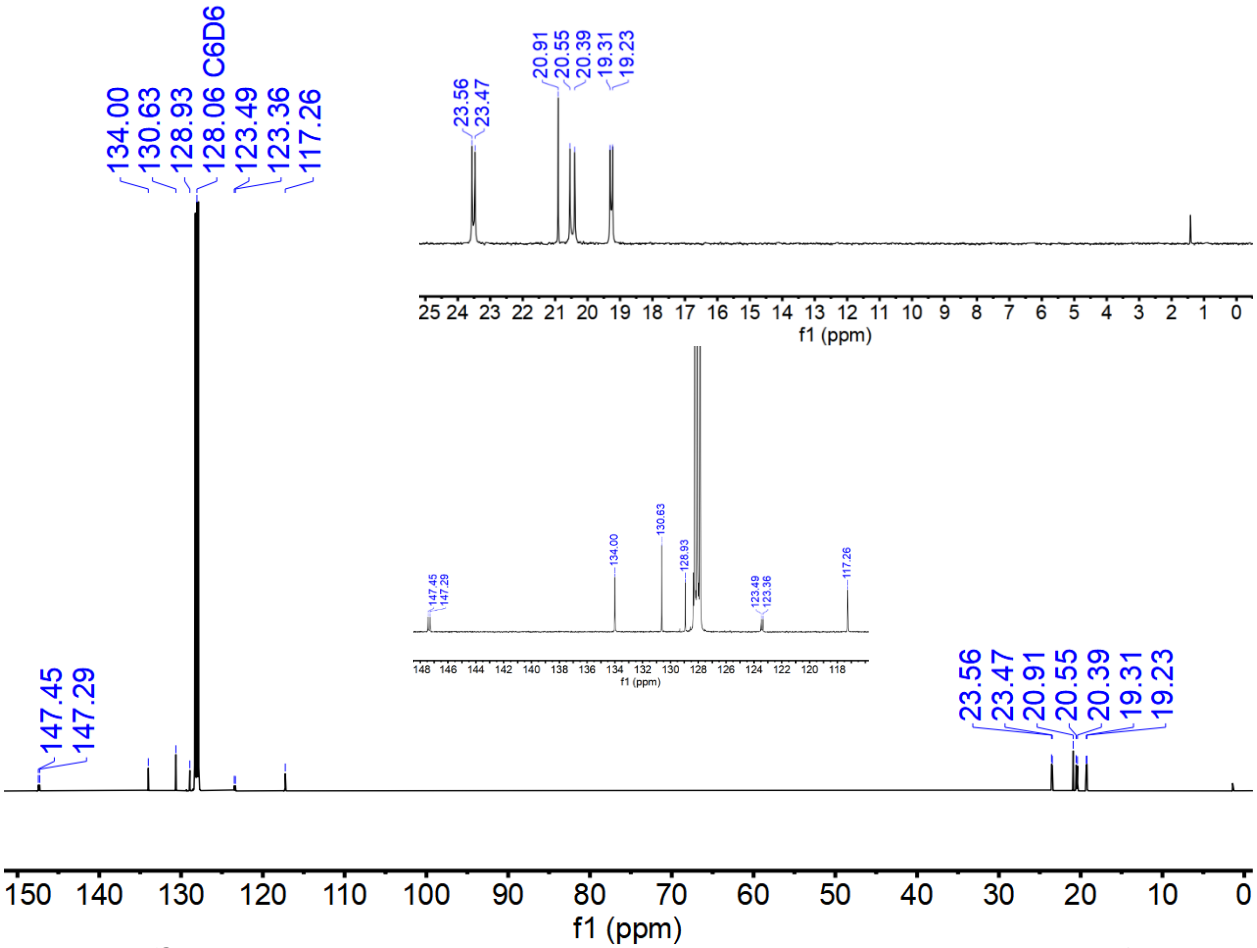

Figure S4. ^{13}C NMR of PNP(H) (126 MHz, ppm, benzene-d$_6$, 25 °C) δ:147.37 (d, <u>*C*</u>–N, $^{2}J_{C\text{-}P}$: 20.4 Hz), 134.00 (<u>*Ph*</u>), 130.63 (<u>*Ph*</u>), 128.93 (<u>*Ph*</u>), 123.43(d, <u>*Ph*</u>, $^{1}J_{C\text{-}P}$: 16.7), 117.26 (<u>*Ph*</u>), 23.52 (d, <u>*C*</u>HMe$_2$, $^{2}J_{C\text{-}P}$: 11.4), 20.91 (Ph–<u>*Me*</u>), 20.47 (d, CH<u>*Me*</u>$_2$, $^{1}J_{C\text{-}P}$: 19.3), 19.27 (d, CH<u>*Me*</u>$_2$, $^{2}J_{C\text{-}P}$: 9.6).

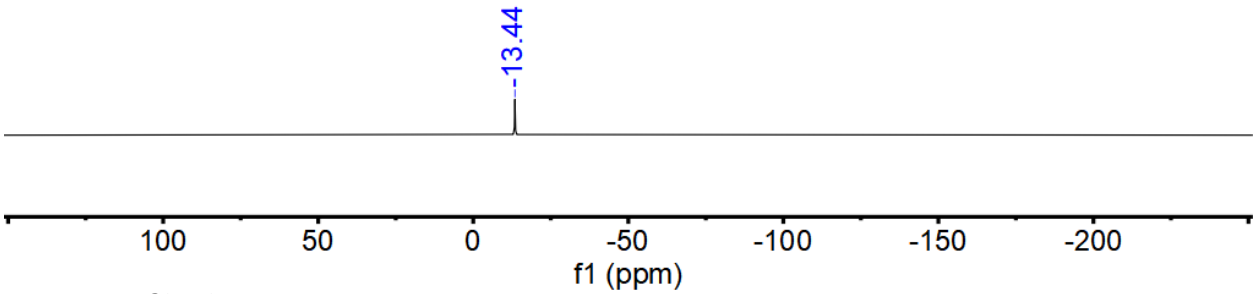

Figure S5. $^{31}P\{^{1}H\}$ NMR of PNP(H) (203 MHz, ppm, benzene-d_6, 25 °C) δ: -13.44.

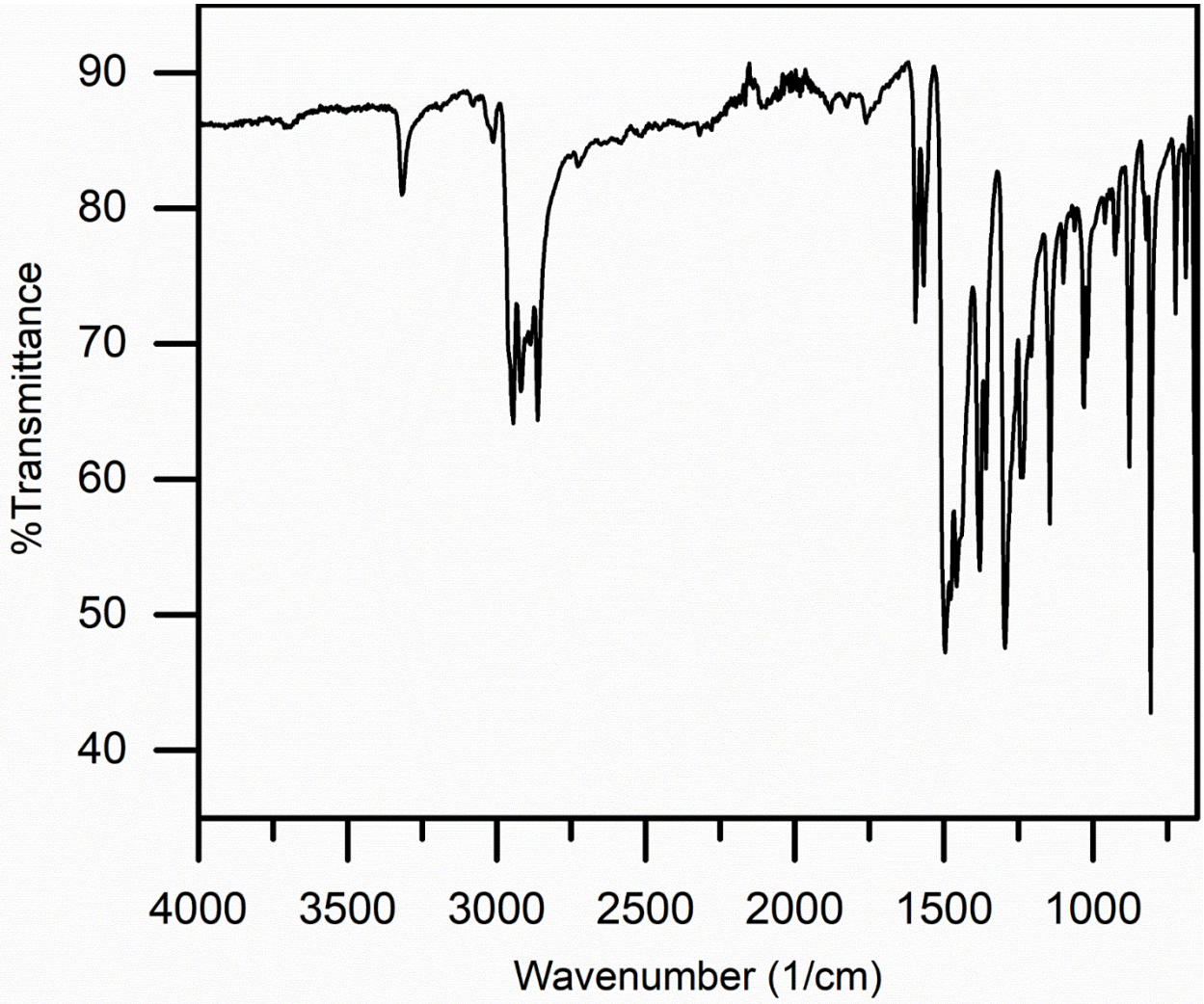

Figure S6. PNP(H) FTIR spectrum**, C**.

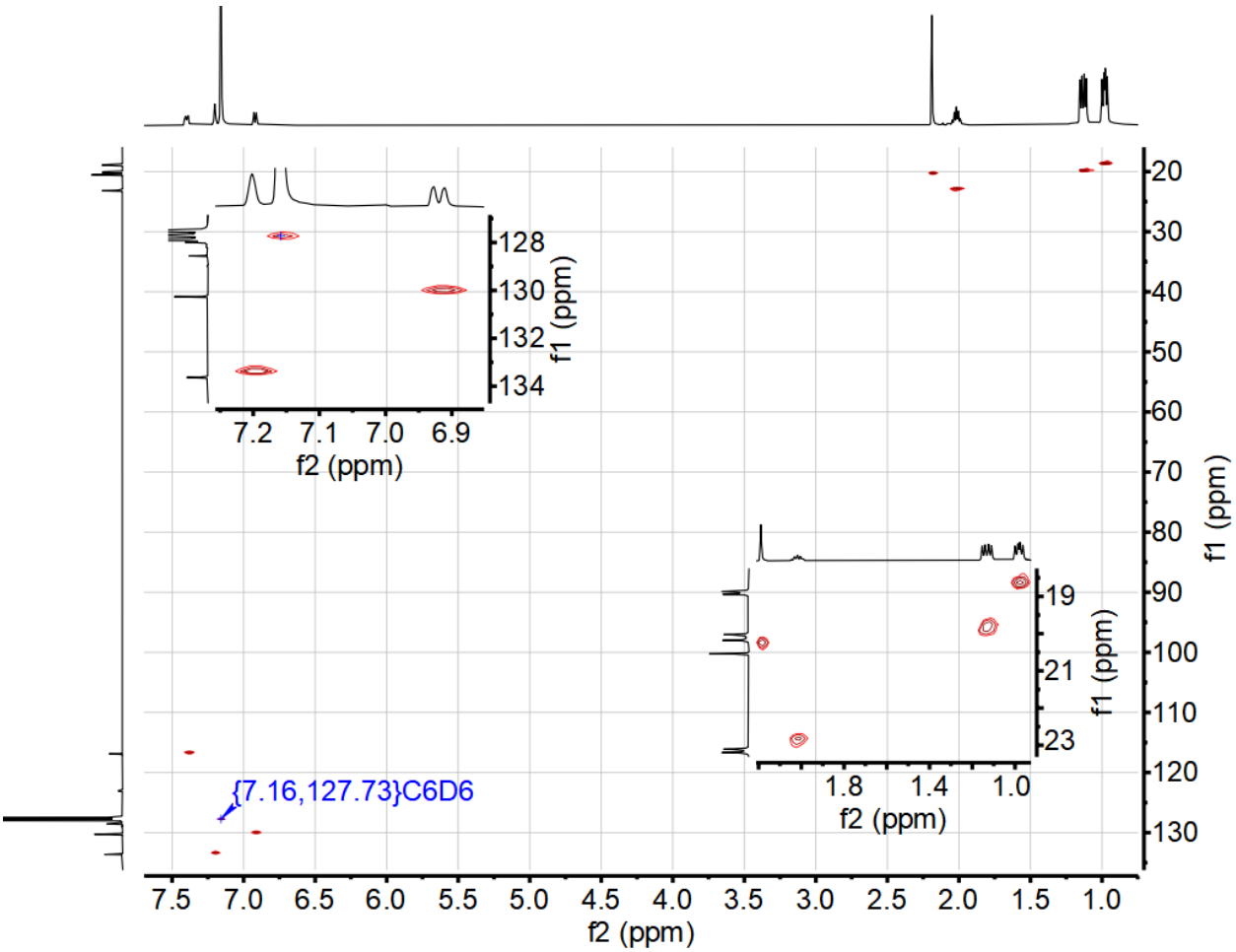

Figure S7. $^{1}H–^{13}C$ gHSQC of PNP(H) (500 MHz, ppm, benzene-d_6, 25 °C)

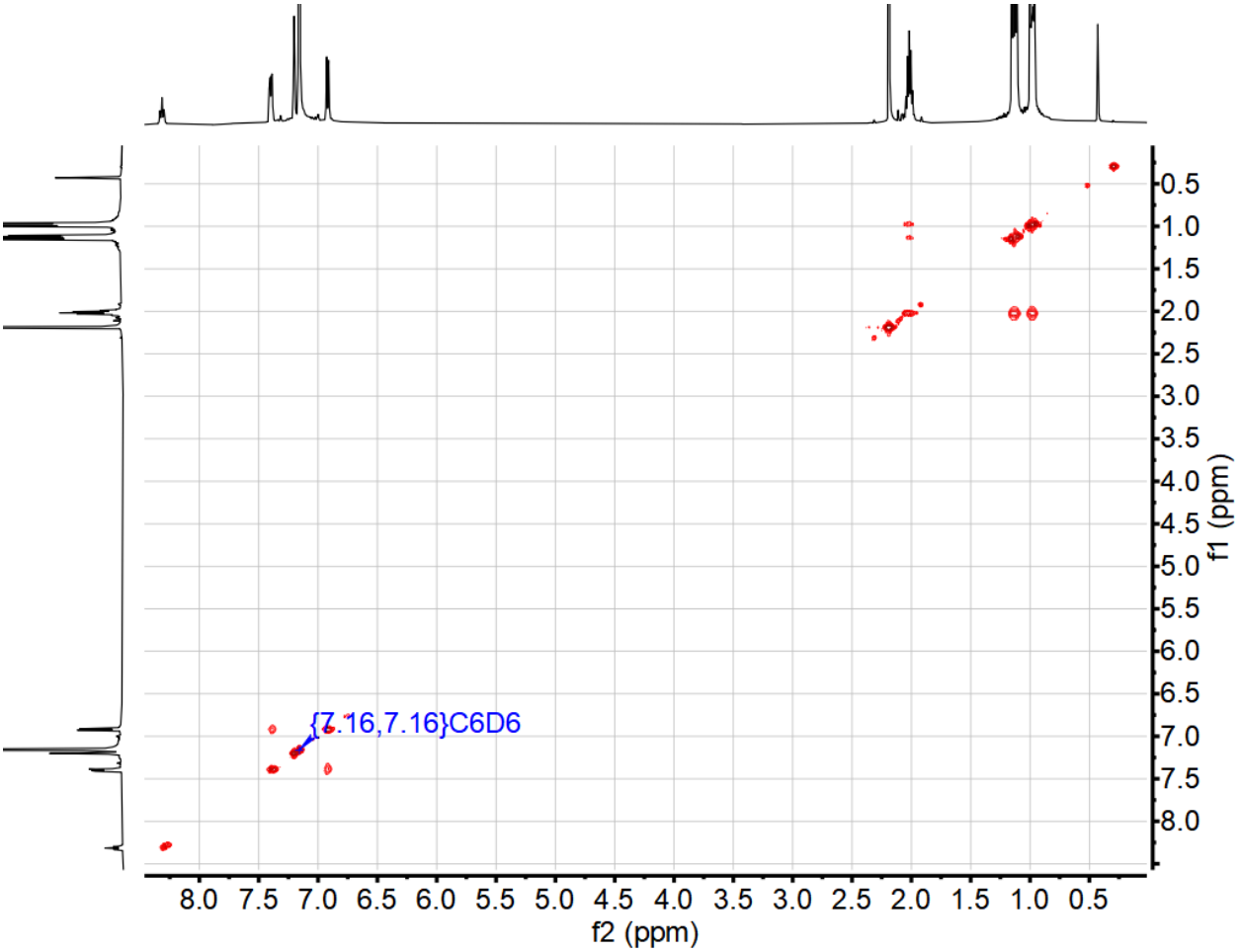

Figure S8. $^{1}H–^{1}H$ gCOSY of PNP(H) in C_6D_6 (500 MHz, ppm, benzene-d_6, 25 °C)

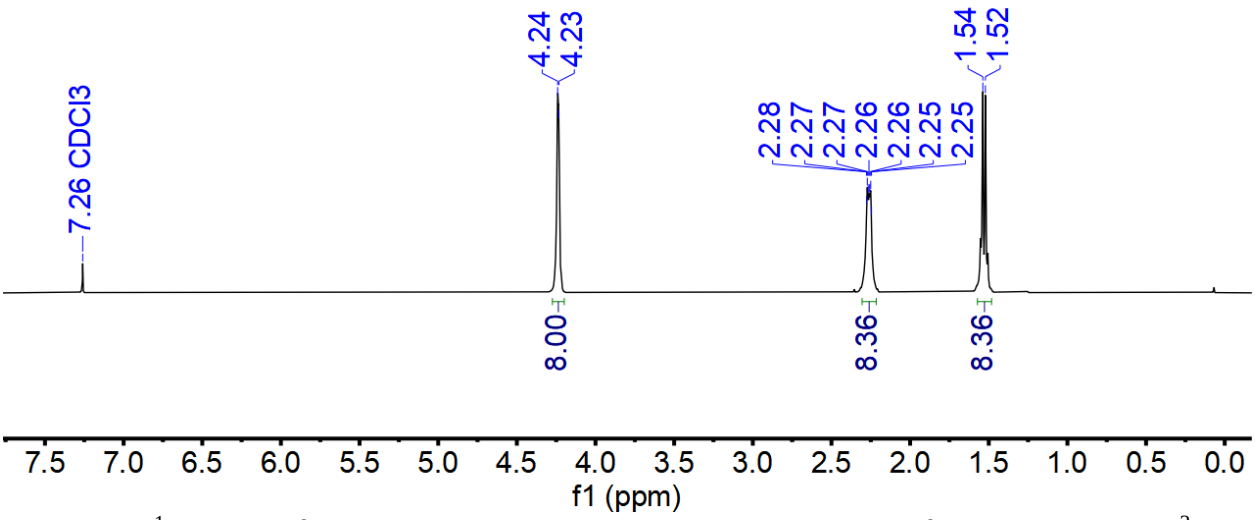

Figure S9. ^{1}H NMR of [Ir(COD)Cl]$_2$ (500 MHz, ppm, $CDCl_3$, 25 °C) δ: 4.24 (d, 8H, *CH*, $^{3}J_{H\text{-}H}$: 4.2 Hz), 2.26 (m, 8H, *CH*$_2$), 1.53 (d, 8H, *CH*$_2$, $^{3}J_{H\text{-}H}$: 8.1 Hz).

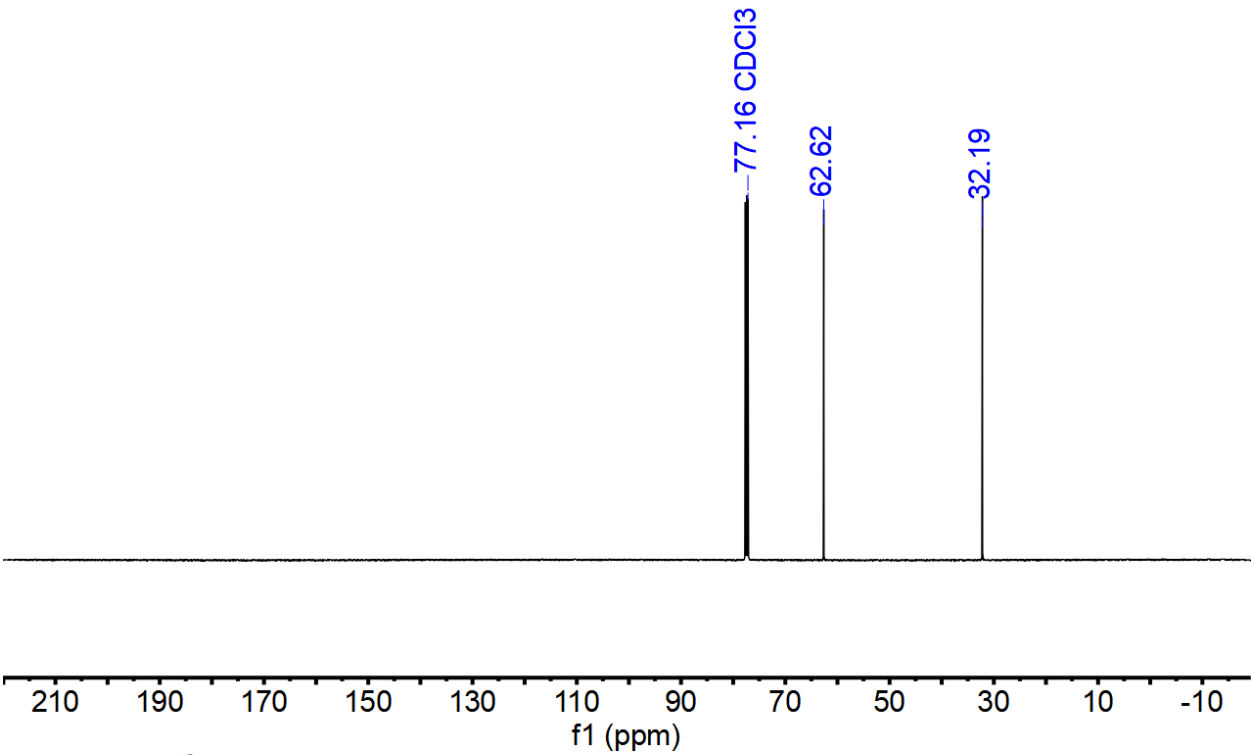

Figure S10. ^{13}C NMR of [Ir(COD)Cl]$_2$ (126 MHz, ppm, $CDCl_3$, 25 °C) δ: 62.62 (<u>*C*</u>H), 32.19 (<u>*C*</u>H$_2$).

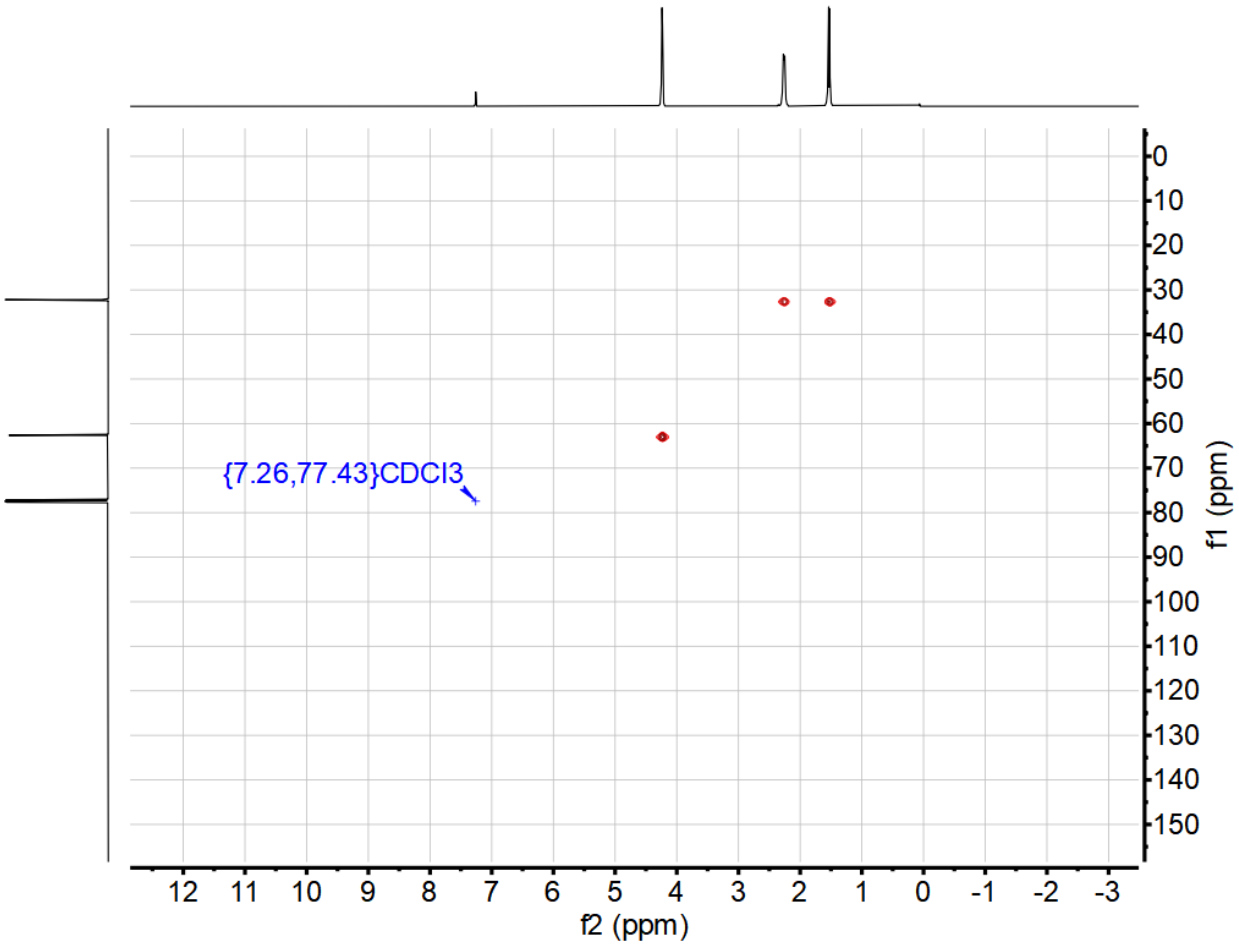

Figure S11. $^{1}H–^{13}C$ HSQC of $[Ir(COD)Cl]_2$ (500 MHz, ppm, $CDCl_3$, 25 °C)

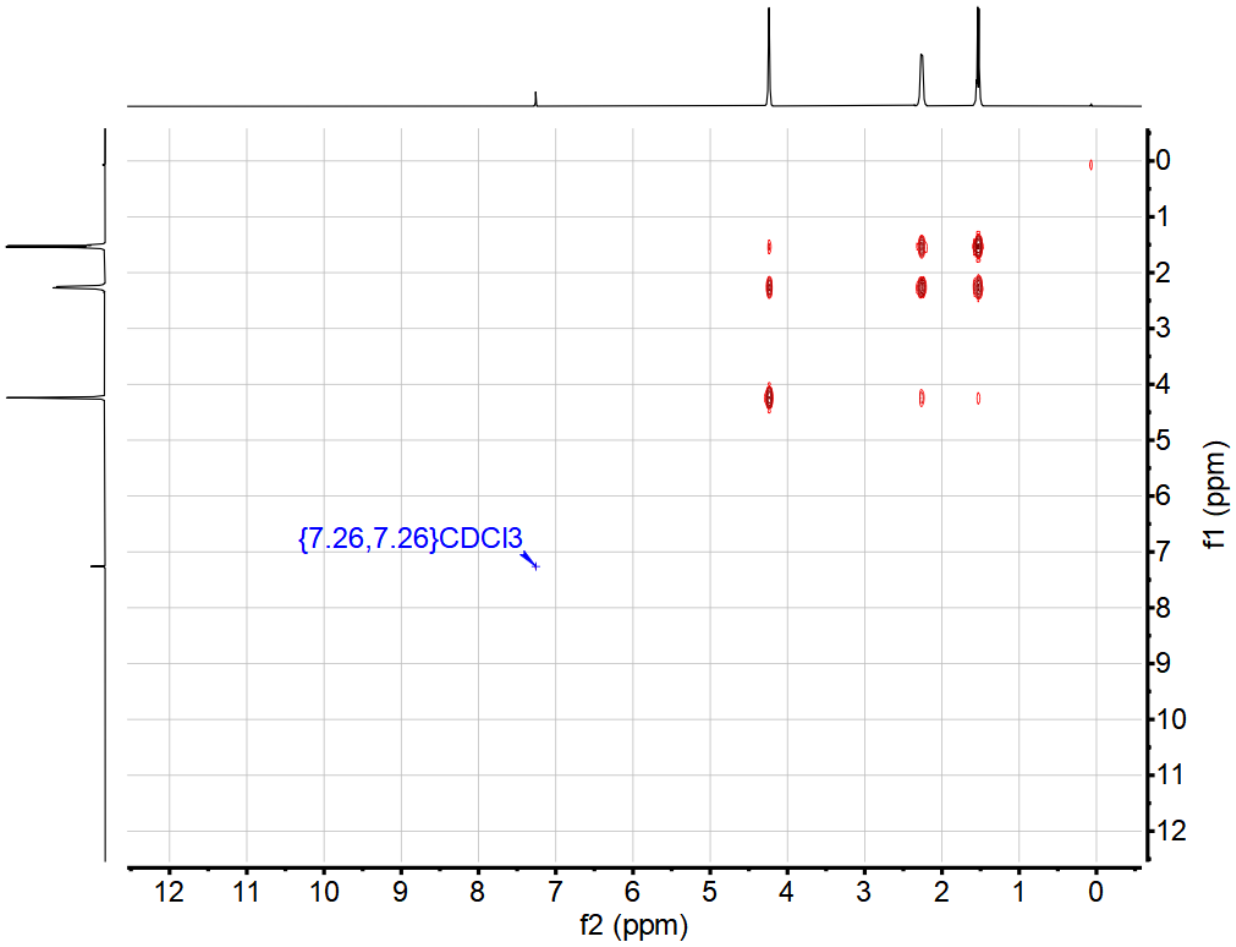

Figure S12. $^{1}H–^{1}H$ gCOSY of $[Ir(COD)Cl]_2$ (500 MHz, ppm, $CDCl_3$, 25 °C)

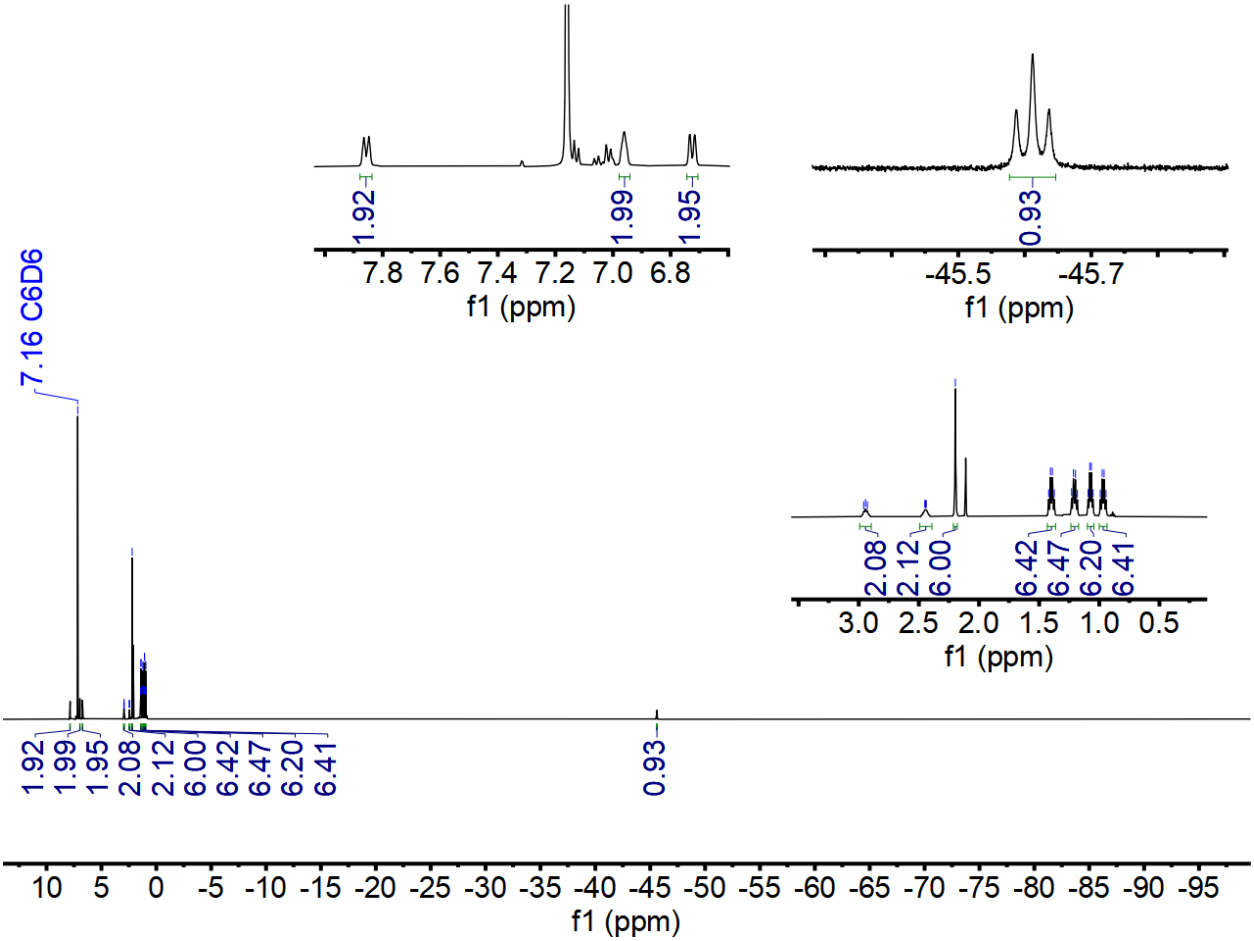

Figure S13. ^{1}H NMR of (PNP)Ir(H)Cl (500 MHz, ppm, benzene-d$_6$, 25 °C): δ: 7.86 (d, 2H, *H*–Ph, $^{3}J_{H\text{-}H}$: 8.8 Hz), 6.96 (s, 2H, *H*–Ph), 6.73 (m, 2H, *H*–Ph), 2.94 (m, 2H, *CH*Me$_2$), 2.44 (m, 2H, *CH*Me$_2$), 2.20 (s, 6H, Ph–*Me*), 1.40 (q, 6H, CH*Me*$_2$, $^{3}J_{H\text{-}H}$: 7.6 Hz), 1.21 (q, 6H, CH*Me*$_2$, $^{3}J_{H\text{-}H}$: 7.9 Hz), 1.07 (q, 6H, CH*Me*$_2$, $^{3}J_{H\text{-}H}$: 6.9 Hz), 0.97 (q, 6H, CH*Me*$_2$, $^{3}J_{H\text{-}H}$: 7.8 Hz), -45.61 (t, 1H, Ir–*H*, $J_{Ir\text{-}H}$: 12.3 Hz).

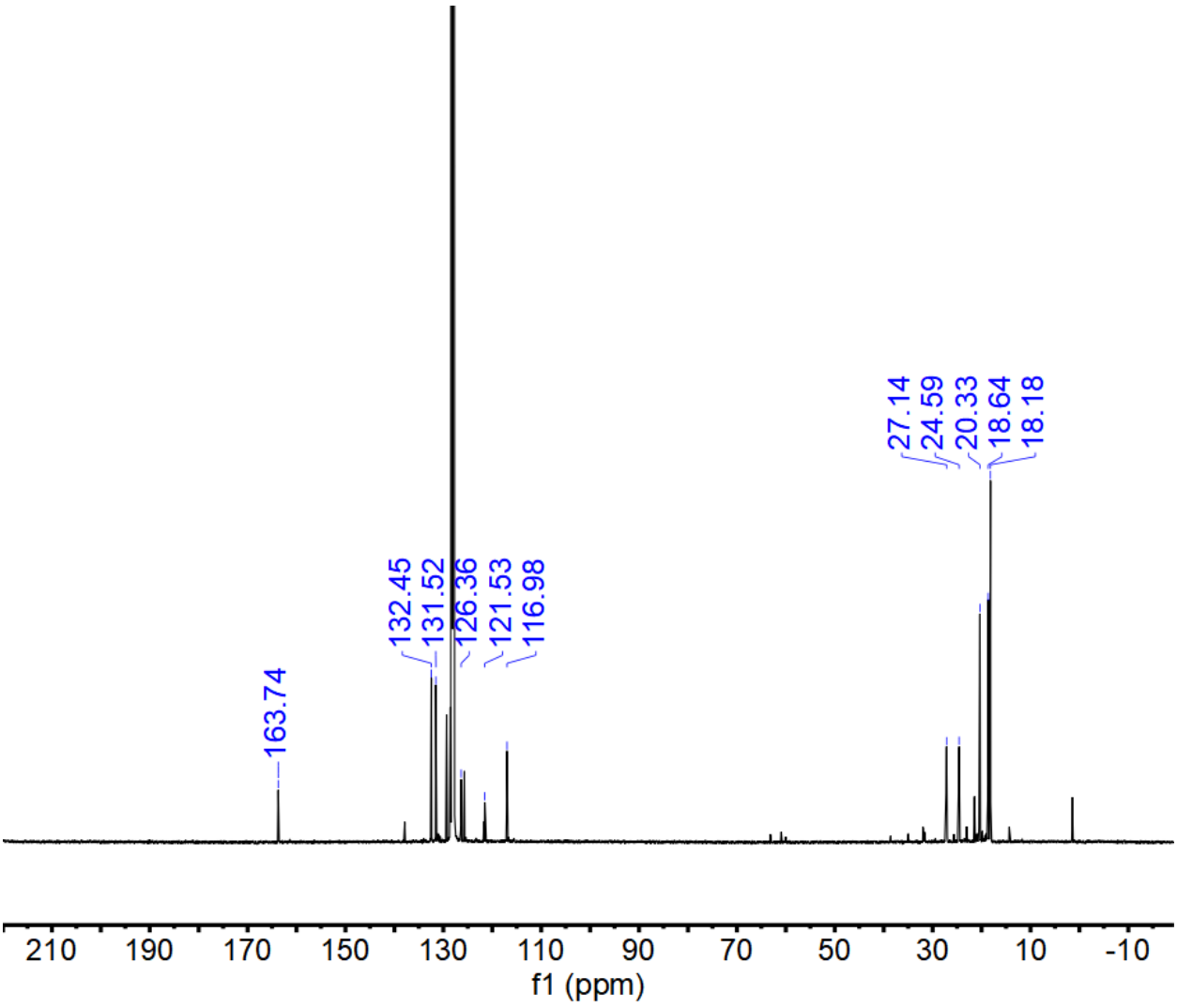

Figure S14. ^{13}C NMR of (PNP)Ir(H)Cl (126 MHz, ppm, benzene-d$_6$, 25 °C) δ: 163.74 (t, <u>*C*</u>–N, $^{2}J_{C\text{-}P}$: 9.52 Hz), 132.45 (<u>*Ph*</u>), 131.52 (<u>*Ph*</u>), 126.36 (t, <u>*Ph*</u>, $^{2}J_{C\text{-}P}$: 3.4 Hz), 121.53 (t, <u>*Ph*</u>, $^{1}J_{C\text{-}P}$: 22.20 Hz), 116.98 (t, <u>*Ph*</u>, $^{2}J_{C\text{-}P}$: 5.08 Hz), 27.14 (t, <u>*C*</u>HMe$_2$, $^{1}J_{C\text{-}P}$: 13.22 Hz), 24.59 (t, <u>*C*</u>HMe$_2$, $^{1}J_{C\text{-}P}$: 16.09 Hz), 20.33 (Ph–<u>*Me)*</u>, 18.64 (CH<u>*Me*</u>$_2$), 18.18 (CH<u>*Me*</u>$_2$).

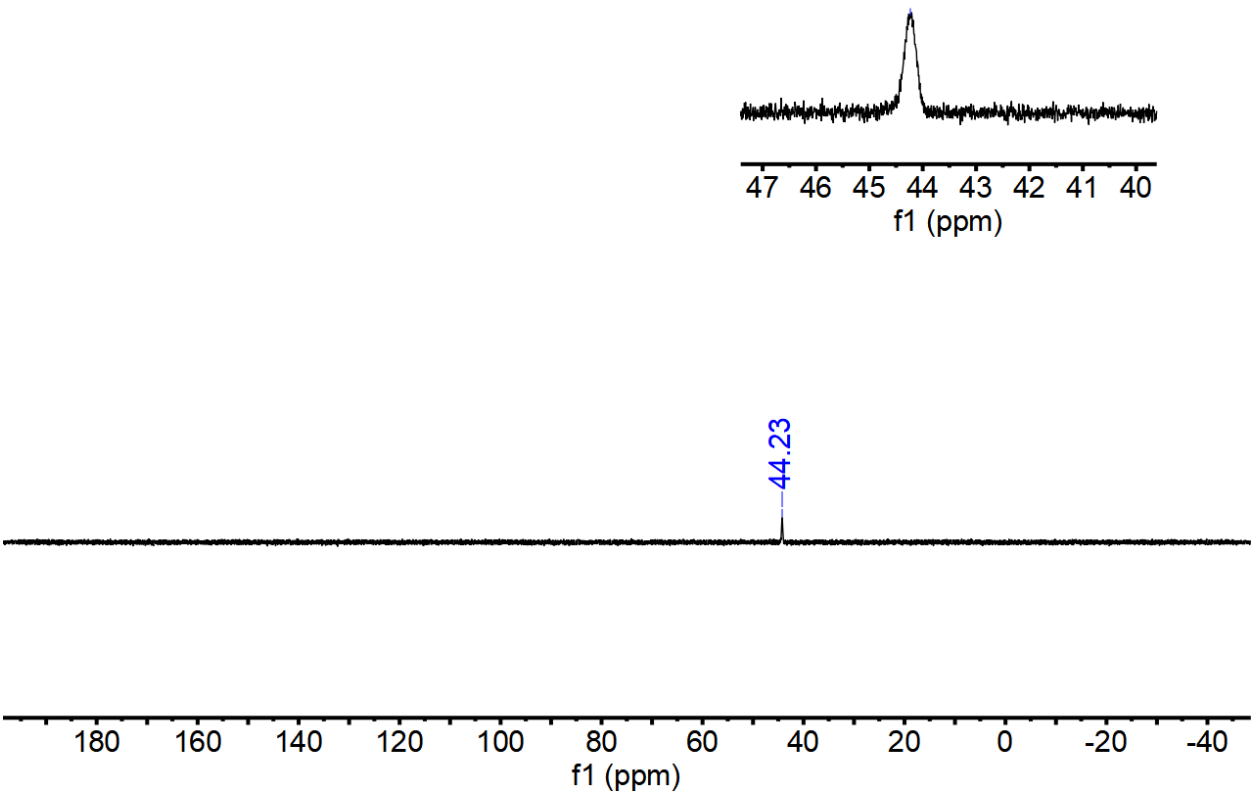

Figure S15. $^{31}P\{^{1}H\}$ NMR of (PNP)Ir(H)Cl (203 MHz, ppm, benzene-d_6, 25 °C) δ: 44.23.

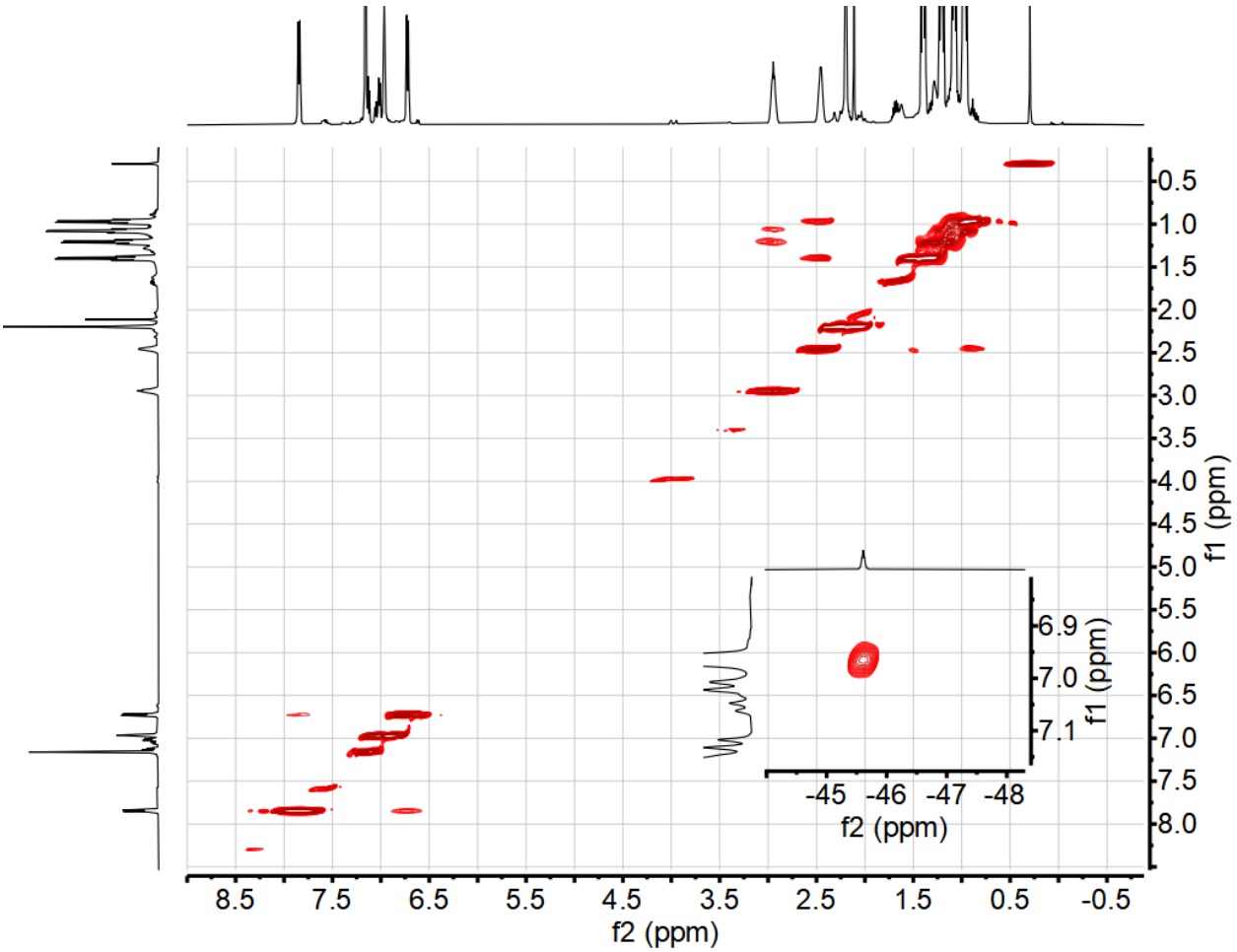

Figure S16. $^{1}H–^{1}H$ gCOSY of (PNP)Ir(H)Cl (500 MHz, ppm, benzene-d_6, 25 °C)

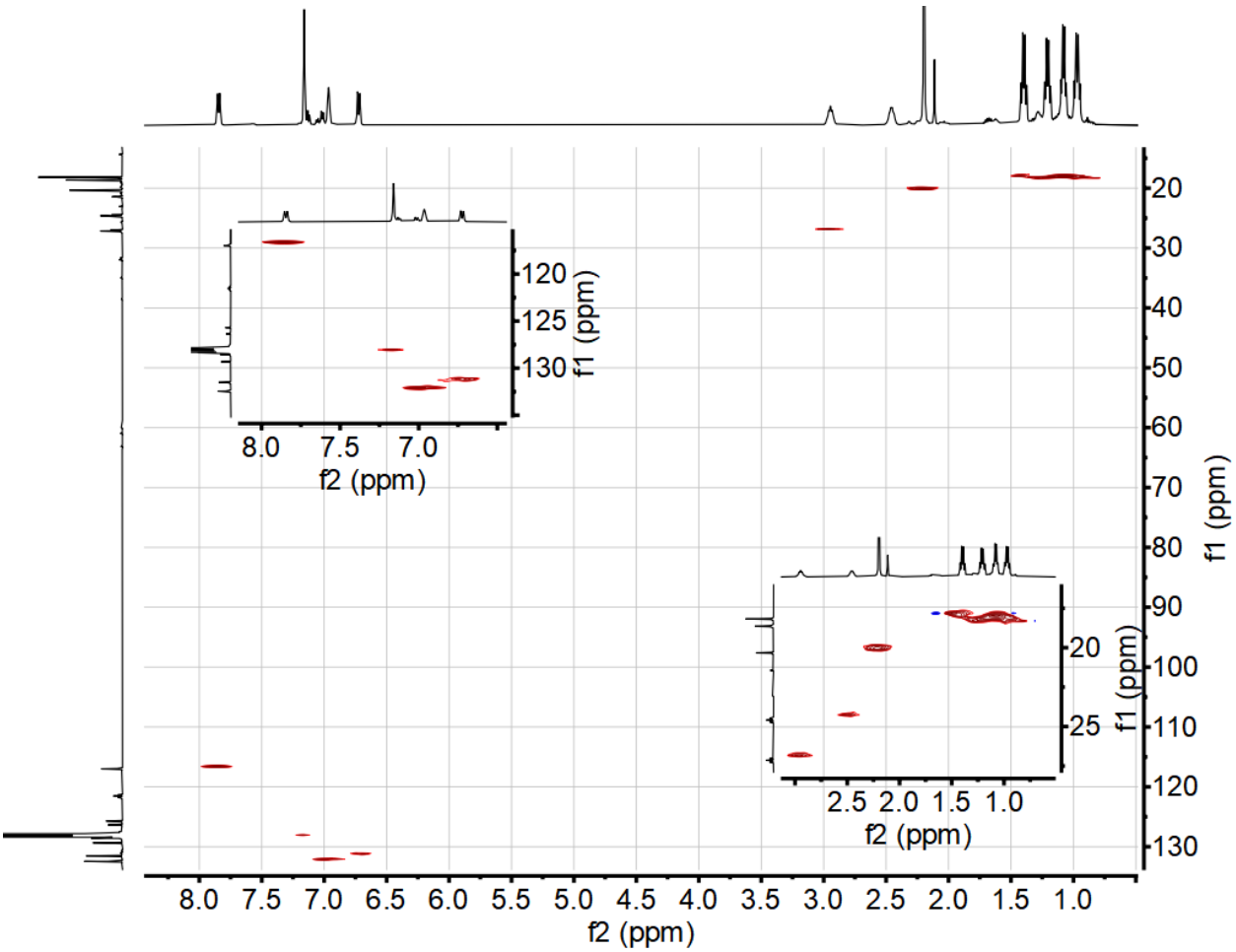

Figure S17. $^{1}H–^{13}C$ gHSQC of (PNP)Ir(H)Cl (500 MHz, ppm, benzene-d_6 , 25 °C)

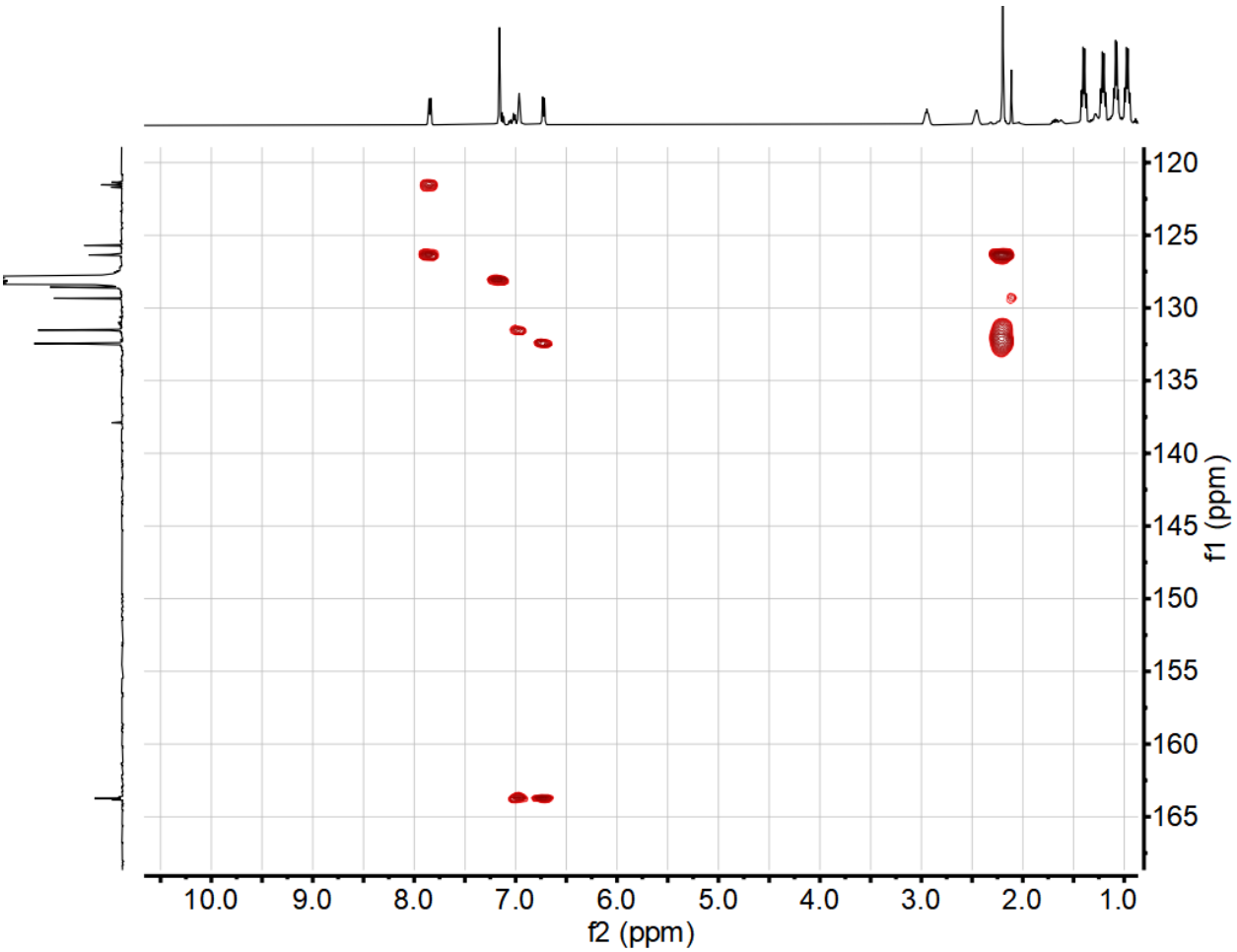

Figure S18. $^{1}H–^{13}C$ gHMBC of (PNP)Ir(H)Cl (500 MHz, ppm, benzene-d_6, 25 °C)

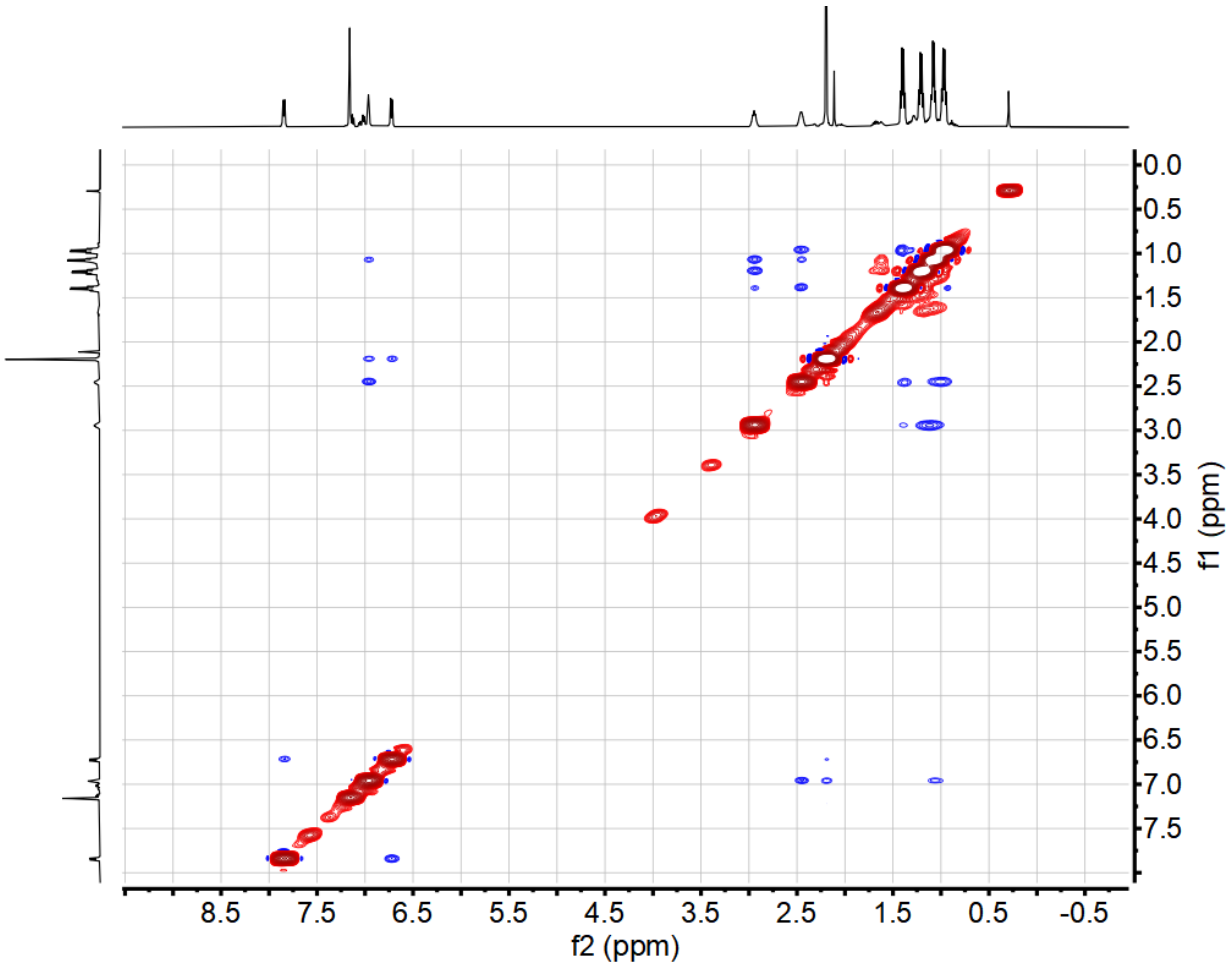

Figure S19. $^{1}H–^{1}H$ NOESY of (PNP)Ir(H)Cl (500 MHz, ppm, benzene-d_6 , 25 °C)

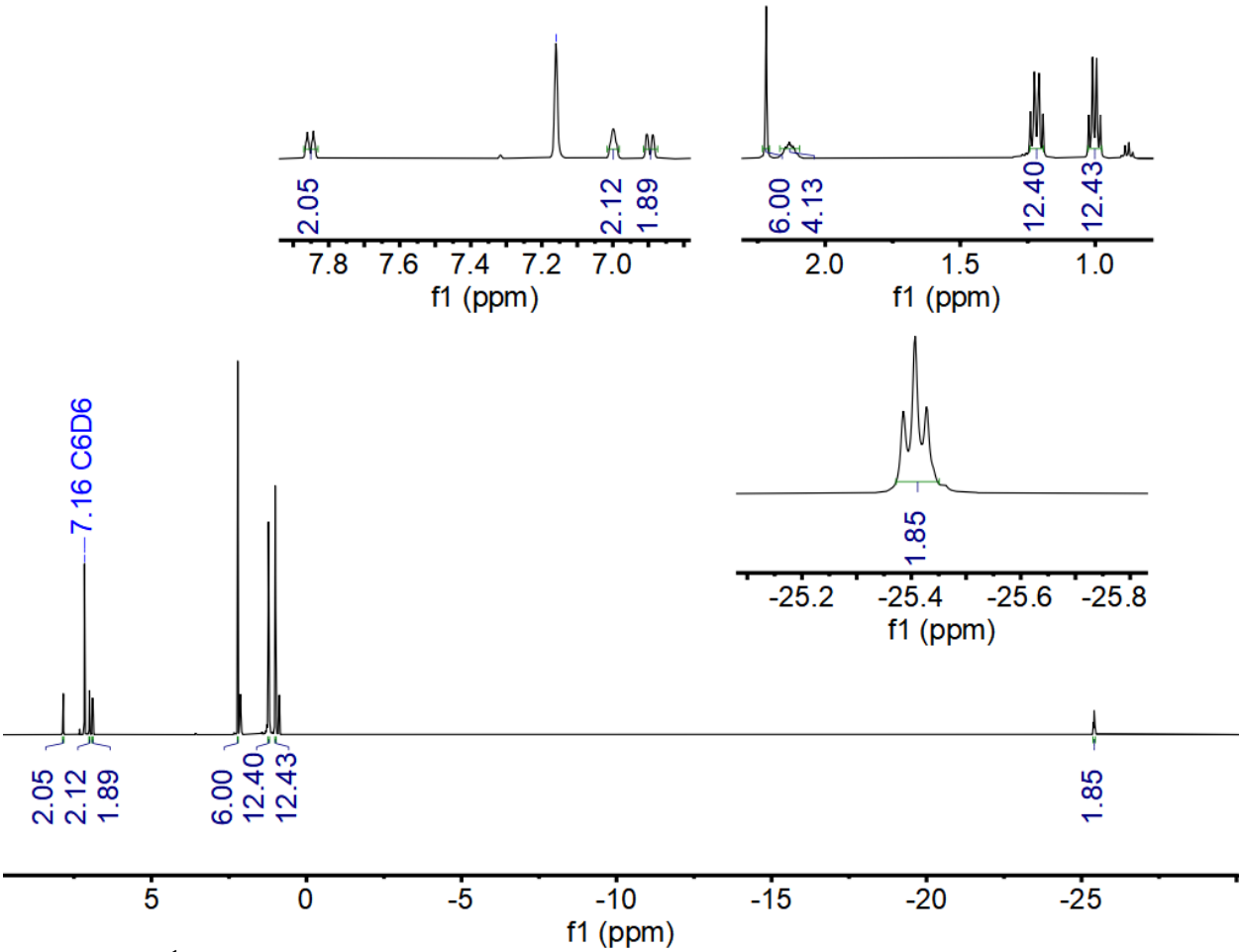

Figure S20. ^{1}H NMR of (PNP)IrH_2 (500 MHz, ppm, benzene-d_6, 25 °C) : 7.85 (dt, 2H, *H*–Ph, $^{3}J_{H\text{-}H}$: 8.6 Hz, $^{4}J_{H\text{-}H}$: *2*.2 Hz), 7.00 (q, 2H, *H*–Ph, $^{4}J_{H\text{-}H}$: 3.6 Hz), 6.90 (dd, 2H, *H*–Ph, $^{3}J_{H\text{-}H}$: 8.7 Hz, $^{4}J_{H\text{-}H}$: *2*.1 Hz), 2.22 (s, 6H, Ph–*Me*), 2.13 (m, 4H, *CH*Me$_2$) 1.22 (q, 12H, CH*Me*$_2$, $^{3}J_{H\text{-}H}$: 7.6 Hz), 1.00 (q, 12H, CH*Me*$_2$, $^{3}J_{H\text{-}H}$: 7.1 Hz), -25.41 (t, 2H, Ir–*H*$_2$, $J_{Ir\text{-}H}$: 10.7 Hz).

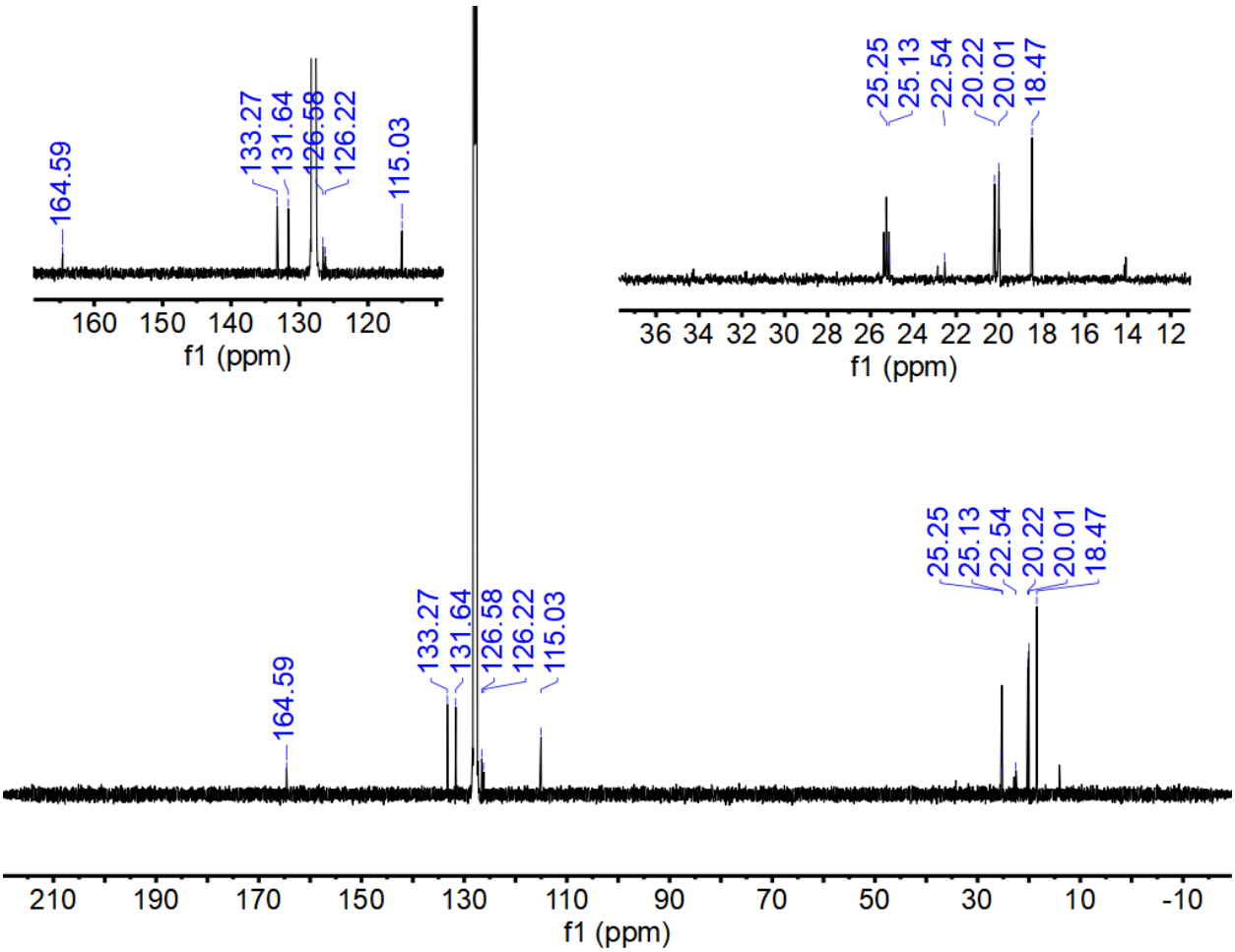

Figure S21. ^{13}C NMR of (PNP)IrH_2 (126 MHz, ppm, benzene-d_6, 25 °C) δ: 164.59 (*C*–N, $^{2}J_{C\text{-}P}$: 10.76 Hz), 133.27 (*Ph*), 131.64 (*Ph*), 126.58 (*Ph*, $^{2}J_{C\text{-}P}$: 10.76 Hz), 126.22 (*Ph*, $^{1}J_{C\text{-}P}$: 19.7 Hz), 115.03 (*Ph*), 25.19 (*C*HMe$_2$)), 22.54 (*C*HMe$_2$), 20.22 (Ph–*Me*), 20.01 (CH*Me*$_2$), 18.47 (CH*Me*$_2$).

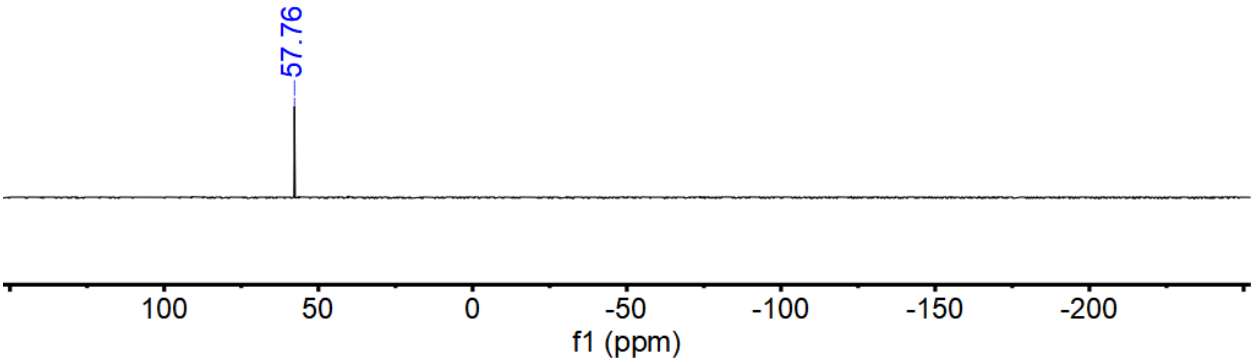

Figure S22. $^{31}P\{^{1}H\}$ NMR of (PNP)IrH_2 (203 MHz, ppm, benzene-d_6, 25 °C): δ: 57.76.

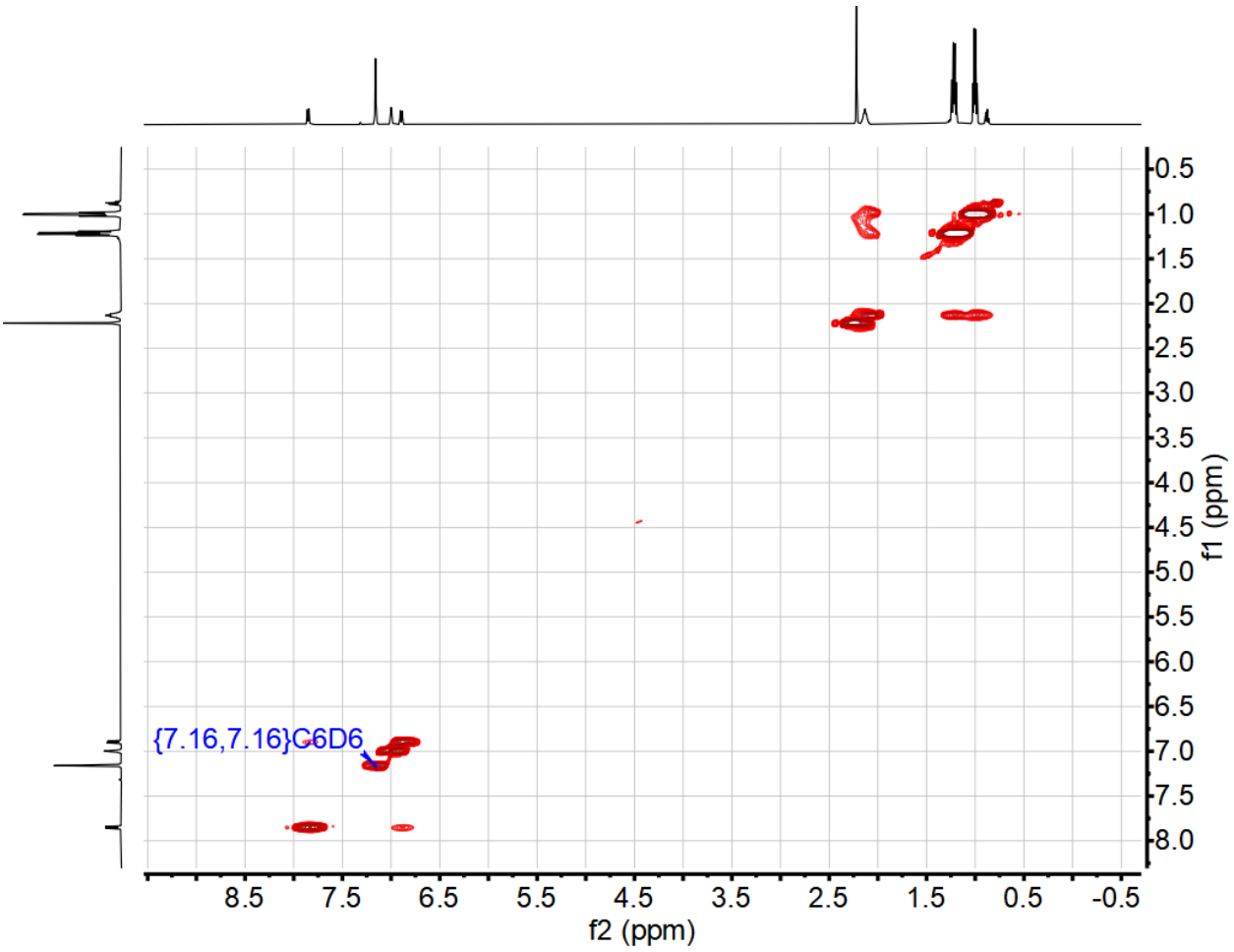

Figure S23. $^{1}H–^{1}H$ gCOSY of (PNP)IrH_2 (500 MHz ppm, benzene-d_6 , 25 °C)

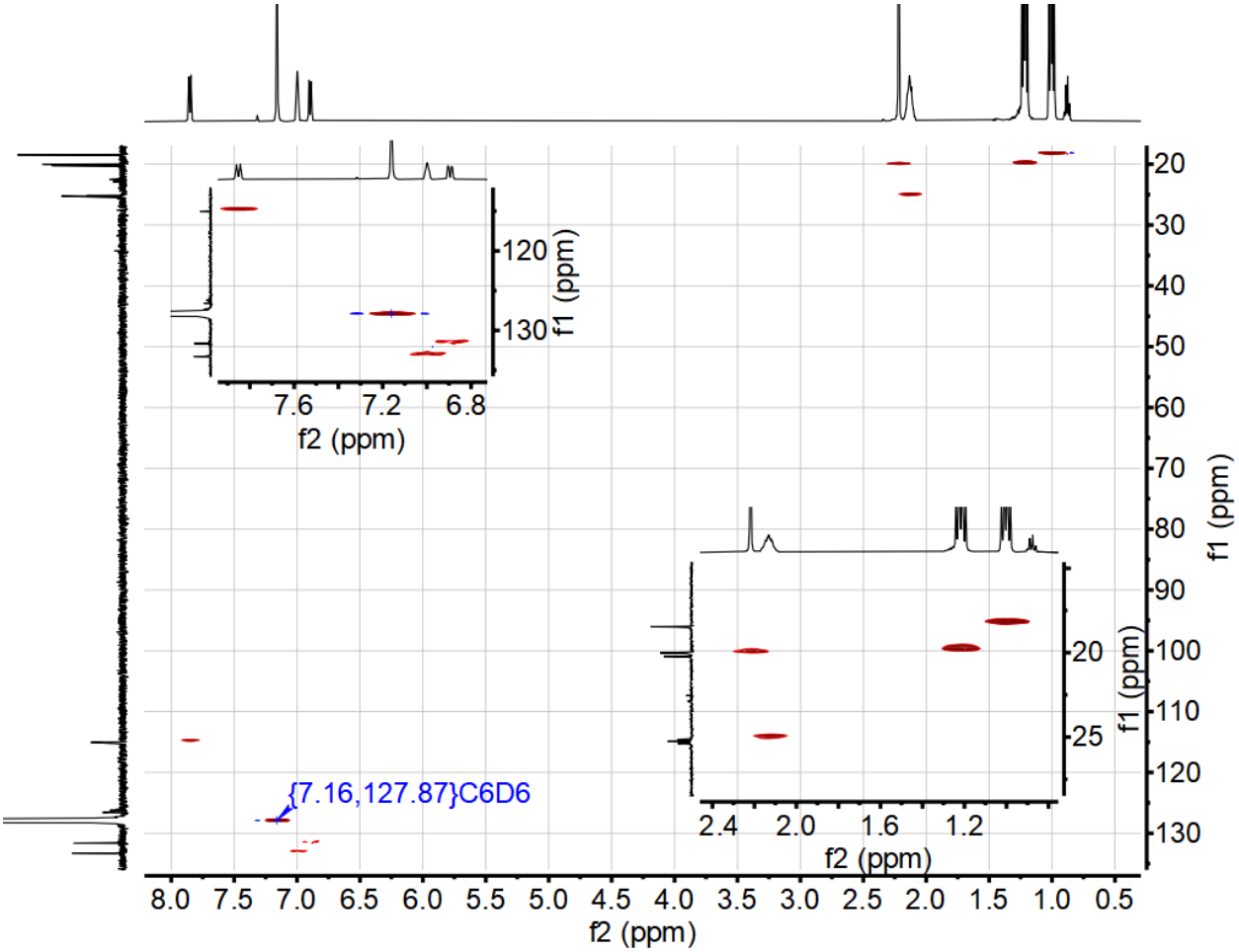

Figure S24. $^{1}H–^{13}C$ gHSQC of (PNP)IrH_2 (500 MHz, ppm, benzene-d_6 , 25 °C)

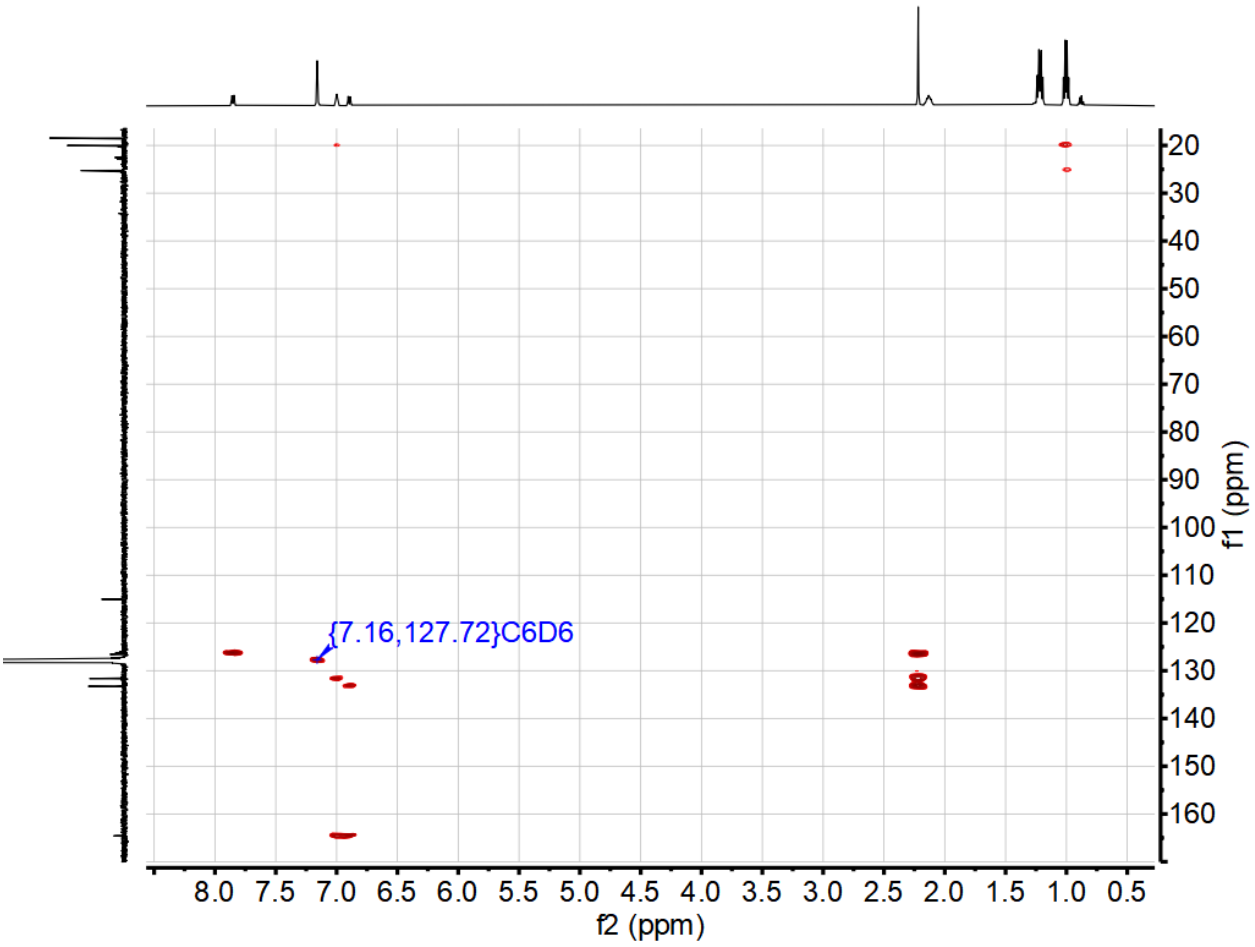

Figure S25. $^{1}H–^{13}C$ gHMBC of (PNP)IrH_2 (500 MHz, ppm, benzene-d_6 , 25 °C)

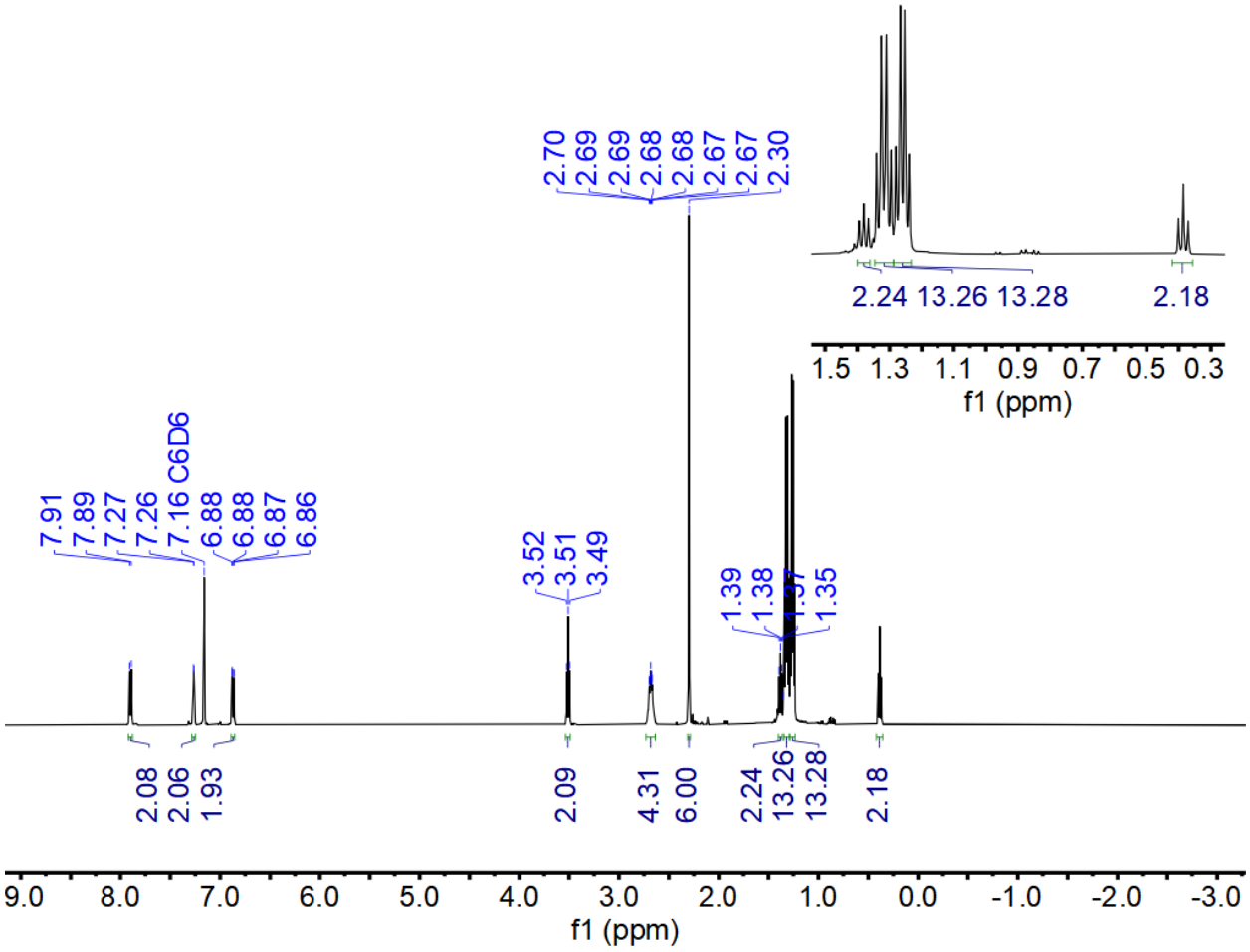

Figure S26: ^{1}H NMR of (PNP)Ir=C(C_3H_6O) (500 MHz, ppm, benzene-d_6, 25 °C) : 7.90 (d, 2H, *H*–Ph, $^{3}J_{H\text{-}H}$: 8.6 Hz), 7.26 (d, 2H, *H*–Ph, $^{3}J_{H\text{-}H}$: 3.1 Hz), 6.87 (dd, 2H, *H*–Ph, $^{3}J_{H\text{-}H}$: 8.6 Hz, $^{4}J_{H\text{-}H}$: 2.1 Hz), 3.51 (t, 2H, C_3H_6O, $^{3}J_{H\text{-}H}$: 7.0 Hz), 2.68 (ddd, 4H, *CH*Me_2, $^{3}J_{H\text{-}H}$: 7.1 Hz, $^{4}J_{H\text{-}H}$: 4.4 Hz, $^{4}J_{H\text{-}H}$: 2.7 Hz), 2.30 (s, 6H, Ph–*Me*), 1.38 (qu, 2H, C_3H_6O, $^{3}J_{H\text{-}H}$: 7.3 Hz), 1.32 (q, 13H, CH*Me*$_2$, $^{3}J_{H\text{-}H}$: 7.4 Hz), 1.26 (q, 13 H, CH*Me*$_2$, $^{3}J_{H\text{-}H}$: 6.9 Hz), 0.39 (t, 2H, C_3H_6O, $^{3}J_{H\text{-}H}$: 7.6 Hz).

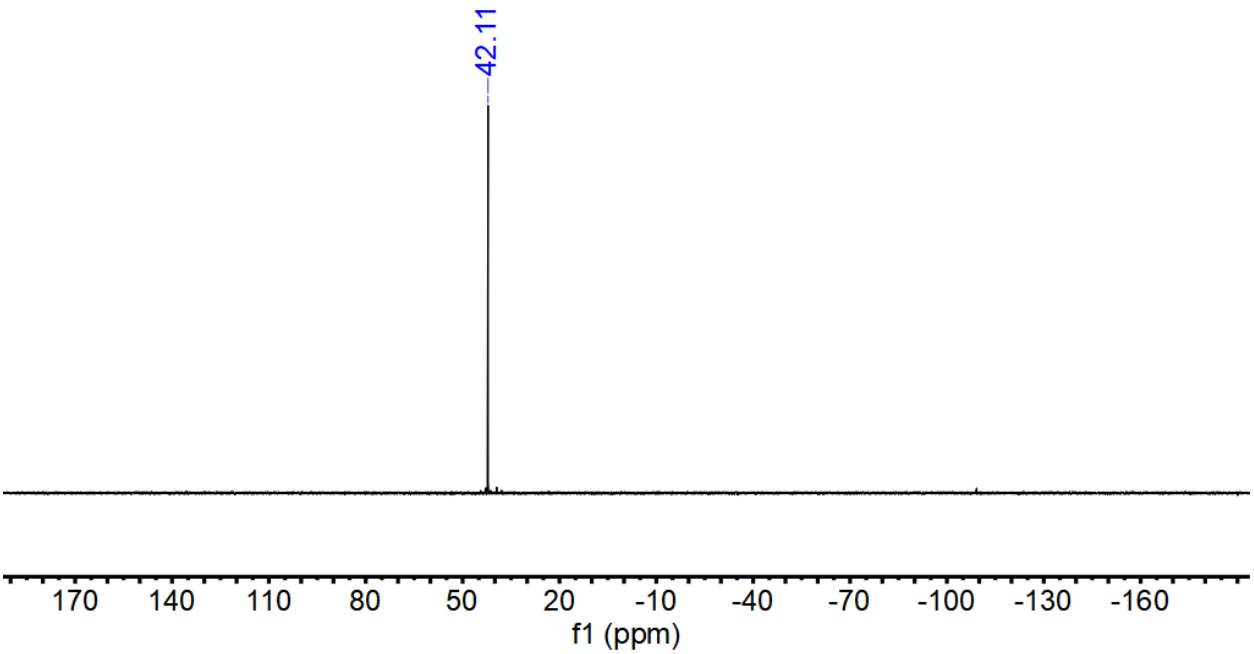

Figure S27. $^{31}P\{^{1}H\}$ NMR of (PNP)Ir=C(C_3H_6O) (203 MHz, ppm, benzene-d_6, 25 °C) δ: 42.11.